FREQUENCY-DOMAIN MODELS FOR NONLINEAR FINITE DEPTH WATER WAVE PROPAGATION

by
JAMES M. KAIHATU

RESEARCH REPORT NO. CACR-94-17
September, 1994

CENTER FOR APPLIED COASTAL RESEARCH
OCEAN ENGINEERING LABORATORY
UNIVERSITY OF DELAWARE
NEWARK, DE 19716

TABLE OF CONTENTS

LIST OF FIGURES xi
LIST OF TABLES xix
ABSTRACT xx

Chapter

1 INTRODUCTION 1

  1.1 General Definition of Domain of Problem 2
  1.2 Boussinesq Equations of Peregrine (1967) and Associated Models 3
  1.3 Implications of the Shallow Water Assumption 6

2 NONLINEAR MILD-SLOPE EQUATION 8

  2.1 Introduction 8
  2.2 Boundary Value Problem 10
  2.3 Resonant Triad Interaction 13
  2.4 Time-Harmonic Wave Propagation in Two Dimensions 15
  2.5 Parabolic Approximation 16
  2.6 Comparison with Agnon et al. (1993) 20
  2.7 Implications of Resonant Triad Interaction Theory 22
  2.8 Summary 25

3 FULLY NONLINEAR EXTENDED BOUSSINESQ EQUATION 27

  3.1 Introduction 27
  3.2 Derivation of a Fully-Nonlinear, Extended Boussinesq Equation . 29
  3.3 Linear Dispersion 30
  3.4 Frequency Domain Transformation 32

3.5 Parabolic Approximation 36
3.6 Linear Shoaling 40

3.6.1 Shoaling Models Derived from the $(\eta, \mathbf{u}_\alpha)$ Form of the Fully Nonlinear Extended Boussinesq Equations 41
3.6.2 Comparison of Linear Shoaling Models 48

3.7 Summary 51

4 COMPARISONS TO DATA - ONE-DIMENSIONAL AND PARABOLIC MODELS 53

4.1 Comparison of Parabolic Models to Whalin (1971) 53
4.2 Comparison to Mase and Kirby (1992) 64

4.2.1 Introduction 64
4.2.2 Energy Dissipation 65
4.2.3 Linear Shoaling as Applicable to Mase and Kirby (1992) . 68
4.2.4 Model to Data Comparison 77
4.2.5 Root-Mean-Square Waveheight, Skewness and Asymmetry 83

4.3 Summary 101

5 ANGULAR SPECTRUM MODELING OF EXTENDED BOUSSINESQ EQUATIONS 107

5.1 Introduction 107
5.2 Simplified Extended Boussinesq Angular Spectrum Model 108
5.3 Angular Spectrum Model of the Fully Nonlinear Extended Boussinesq Equation 111

5.3.1 Longshore Periodic Waves 111
5.3.2 Shoaling Waves 115

5.4 Permanent Form Solutions 118
5.5 Summary 122

6 COMPARISONS TO DATA - ANGULAR SPECTRUM MODELS 125

6.1 Introduction 125

6.2 Comparison of Parabolic and Angular Spectrum Models to Hammack et al. (1990) 125

6.2.1 Introduction 125
6.2.2 Comparison of Models to Mach Stem Experimental Data . 128
6.2.3 Results 132

6.3 Summary 155

7 CONCLUSIONS AND SUGGESTIONS FOR FUTURE WORK 158
REFERENCES 165

LIST OF FIGURES

1.1 Comparison of Three Dispersion Relations. Linear Dispersion Relation (–); Dispersion Relation of the Boussinesq Equations (- -); Dispersion Relation of the KdV Equation (..). 5

2.1 Relative Magnitude of Phase Mismatch $k_2 - 2k_1$ 24

3.1 Comparison of Wave Celerities and Group Velocities to Those of Linear Theory for Several Values of α: $\alpha = -0.3855$ (—); $\alpha = -0.390$ (- - -); $\alpha = -1/3$ (. . .); $\alpha = -2/5$ (- . -). (Top) Normalized Wave Celerity; (Bottom) Normalized Group Velocity. 33

3.2 Comparison of Shoaling Model to Linear Shoaling for Several Values of β: Linear Theory (—); $\beta = -0.354$ (- - -); $\beta = -1/3$ (. . .); $\beta = 0$ (- . -) 46

3.3 Comparison of Shoaling Models (Deep Water): Linear Theory (–); Linearized (η, ϕ_α) Equations (- -); β-Dependent Shoaling Model with $\beta = -0.354$ (. .); Energy Flux Conservation Model Using Approximate Group Velocity Expression (- .); Green's Law (∘∘) 49

3.4 Comparison of Shoaling Models (Intermediate Water): Linear Theory (—); Linearized (η, ϕ_α) Equations (- -); β-Dependent Shoaling Model with $\beta = -0.354$ (. .); Energy Flux Conservation Model Using Approximate Group Velocity Expression (- .); Green's Law (∘∘) 50

4.1 Wavetank Layout of Experiment of Whalin (1971): (Top) Bottom Contours; (Bottom) Centerline Depth. 55

4.2 Comparisons Between Models and Whalin's Experiment, $T = 3$s, $a_o = 0.68$cm. Fully Nonlinear Extended Boussinesq Model (–), Extended Boussinesq Model of Chen and Liu (1993) (- -), Nonlinear Mild-Slope Model (-.-), KP Model of Liu et al. (1985) (..), Data of Whalin (1971) (oo). (Top) First Harmonic; (Middle) Second Harmonic; (Bottom) Third Harmonic. 58

4.3 Comparisons Between Models and Whalin's Experiment, $T = 3$s, $a_o = 0.98$cm. Fully Nonlinear Extended Boussinesq Model (–), Extended Boussinesq Model of Chen and Liu (1993) (- -), Nonlinear Mild-Slope Model (-.-), KP Model of Liu et al. (1985) (..), Data of Whalin (1971) (oo). (Top) First Harmonic; (Middle) Second Harmonic; (Bottom) Third Harmonic. 59

4.4 Comparisons Between Models and Whalin's Experiment, $T = 3$s, $a_o = 1.46$cm. Fully Nonlinear Extended Boussinesq Model (–), Extended Boussinesq Model of Chen and Liu (1993) (- -), Nonlinear Mild-Slope Model (-.-), KP Model of Liu et al. (1985) (..), Data of Whalin (1971) (oo). (Top) First Harmonic; (Middle) Second Harmonic; (Bottom) Third Harmonic. 60

4.5 Comparisons Between Models and Whalin's Experiment, $T = 2$s, $a_o = 0.75$cm. Fully Nonlinear Extended Boussinesq Model (–), Extended Boussinesq Model of Chen and Liu (1993) (- -), Nonlinear Mild-Slope Model (-.-), KP Model of Liu et al. (1985) (..) Data of Whalin (1971) (oo). (Top) First Harmonic; (Middle) Second Harmonic; (Bottom) Third Harmonic. 61

4.6 Comparisons Between Models and Whalin's Experiment, $T = 2$s, $a_o = 1.06$cm. Fully Nonlinear Extended Boussinesq Model (–), Extended Boussinesq Model of Chen and Liu (1993) (- -), Nonlinear Mild-Slope Model (-.-), KP Model of Liu et al. (1985) (..), Data of Whalin (1971) (oo). (Top) First Harmonic; (Middle) Second Harmonic; (Bottom) Third Harmonic. 62

4.7 Comparisons Between Models and Whalin's Experiment, $T = 2$s, $a_o = 1.49$cm. Fully Nonlinear Extended Boussinesq Model (–), Extended Boussinesq Model of Chen and Liu (1993) (- -), Nonlinear Mild-Slope Model (-.-), KP Model of Liu et al. (1985) (..), Data of Whalin (1971) (oo). (Top) First Harmonic; (Middle) Second Harmonic; (Bottom) Third Harmonic. 63

4.8 Experimental Setup of Mase and Kirby (1992) (from Wei and Kirby 1994) 64

4.9 Shoaling Coefficients K_s from Linear Theory for Same Frequency Range and Bathymetry as Used in Model Comparisons to Mase and Kirby (1992) 69

4.10 Shoaling Coefficients K_s from Green's Law, for Same Frequency Range and Bathymetry as Used in Model Comparisons to Mase and Kirby (1992) 70

4.11 Shoaling Coefficients K_s from Fully Nonlinear Extended Boussinesq Model, for Same Frequency Range and Bathymetry as Used in Model Comparisons to Mase and Kirby (1992) 71

4.12 Percent Error Between Green's Law and Shoaling from Linear Theory 72

4.13 Percent Error Between Linear Shoaling from Fully Nonlinear Extended Boussinesq Equation and Shoaling from Linear Theory 73

4.14 Comparison of Linear Shoaling Errors from Green's Law (–) and Fully Nonlinear Extended Boussinesq Model (- -). (Top) $f = 0.3Hz$; (Middle) $f = 0.9Hz$; (Bottom) $f = 1.2Hz$ 75

4.15 Comparison of Linear Shoaling Errors from Green's Law (–) and Fully Nonlinear Extended Boussinesq Model (- -). (Top) $f = 1.5Hz$; (Middle) $f = 2.4Hz$; (Bottom) $f = 3.0Hz$ 76

4.16 Comparison of Shoaling Models to Case 2 of Mase and Kirby (1992). Experimental Data (–), Fully Dispersive Shoaling Model (- -), Consistent Model of Freilich and Guza (1984) (. .), Fully Nonlinear Extended Boussinesq Frequency Domain Model (- .). (Top) Input Spectra at $d = 47\ cm$; (Bottom) $d = 35\ cm$. 79

4.17 Comparison of Shoaling Models to Case 2 of Mase and Kirby (1992). Experimental Data (–), Fully Dispersive Shoaling Model (- -), Consistent Model of Freilich and Guza (1984) (. .), Fully Nonlinear Extended Boussinesq Frequency Domain Model (- .). (Top) $d = 30\ cm$; (Middle) $d = 25\ cm$; (Bottom) $d = 20\ cm$. . . 80

4.18 Comparison of Shoaling Models to Case 2 of Mase and Kirby (1992). Experimental Data (–), Fully Dispersive Shoaling Model (- -), Consistent Model of Freilich and Guza (1984) (. .), Fully Nonlinear Extended Boussinesq Frequency Domain Model (- .). (Top) $d = 17.5\ cm$; (Middle) $d = 15\ cm$; (Bottom) $d = 12.5\ cm$. 81

4.19 Comparison of Shoaling Models to Case 2 of Mase and Kirby (1992). Experimental Data (–), Fully Dispersive Shoaling Model (- -), Consistent Model of Freilich and Guza (1984) (. .), Fully Nonlinear Extended Boussinesq Frequency Domain Model (- .). (Top) $d = 10.0\ cm$; (Middle) $d = 7.5cm$; (Bottom) $d = 5\ cm$ . . 82

4.20 Variation of H_{rms} of Experimental Data of Mase and Kirby (1992) with Depth. H_{rms} Averaged Over Seven Realizations (–), Average H_{rms} with One Standard Deviation Added or Subtracted (- -). (Top) Data Truncated At 300 Components; (Bottom) Full Spectrum. 85

4.21 Variation of H_{rms} of Model Result with Depth. H_{rms} Averaged Over Seven Realizations (–), Average H_{rms} with One Standard Deviation Added or Subtracted (- -). (Top) Fully Dispersive Nonlinear Shoaling Model; (Middle) Consistent Shoaling Model of Freilich and Guza (1984); (Bottom) Fully Nonlinear Extended Boussinesq Model 86

4.22 Comparison of Average H_{rms}. Experimental Data of Mase and Kirby (1992) Truncated at 300 Components (-); Fully Dispersive Nonlinear Shoaling Model (- -); Consistent Shoaling Model of Freilich and Guza (1984) (. .); Fully Nonlinear Extended Boussinesq Model (- . -) 87

4.23 Effect of Truncation of Experimental Data of Mase and Kirby (1992) on H_{rms} Variation. Full Spectra (–); Spectra Truncated at 300 Components (- -) 88

4.24 Variation of Skewness of Experimental Data of Mase and Kirby (1992) with Depth. Skewness Averaged Over Seven Realizations (–), Average Skewness with One Standard Deviation Added or Subtracted (- -). (Top) Data Truncated At 300 Components; (Bottom) Full Spectrum. 90

4.25 Variation of Skewness of Model Result with Depth. Skewness Averaged Over Seven Realizations (–), Average Skewness with One Standard Deviation Added or Subtracted (- -). (Top) Fully Dispersive Nonlinear Shoaling Model; (Middle) Consistent Shoaling Model of Freilich and Guza (1984); (Bottom) Fully Nonlinear Extended Boussinesq Model 91

4.26 Comparison of Average Skewness. Experimental Data of Mase and Kirby (1992) Truncated at 300 Components (–); Fully Dispersive Nonlinear Shoaling Model (- -); Consistent Shoaling Model of Freilich and Guza (1984) (. .); Fully Nonlinear Extended Boussinesq Model (- .) 92

4.27 Effect of Truncation of Experimental Data of Mase and Kirby (1992) on Skewness Variation. Full Spectra (–); Spectra Truncated at 300 Components (- -) 93

4.28 Variation of Asymmetry of Experimental Data of Mase and Kirby (1992) with Depth. Asymmetry Averaged Over Seven Realizations (–), Average Asymmetry with One Standard Deviation Added or Subtracted (- -). (Top) Data Truncated At 300 Components; (Bottom) Full Spectrum. 96

4.29 Variation of Asymmetry of Model Result with Depth. Asymmetry Averaged Over Seven Realizations (–), Average Asymmetry with One Standard Deviation Added or Subtracted (- -). (Top) Fully Dispersive Nonlinear Shoaling Model; (Middle) Consistent Shoaling Model of Freilich and Guza (1984); (Bottom) Fully Nonlinear Extended Boussinesq Model 97

4.30 Comparison of Average Asymmetry. Experimental Data of Mase and Kirby (1992) Truncated at 300 Components (–); Fully Dispersive Nonlinear Shoaling Model (- -); Consistent Shoaling Model of Freilich and Guza (1984) (. .); Fully Nonlinear Extended Boussinesq Model (- .) 98

4.31 Effect of Truncation of Experimental Data of Mase and Kirby (1992) on Asymmetry Variation. Full Spectra (–); Spectra Truncated at 300 Components (- -) 99

6.1 Tank And Gage Layout for Experiment of Hammack et al. (1990) 126

6.2 Comparison of Different Permanent Form Solutions for Input to Evolution Models: Permanent Form Solution to KP Model of Liu et al. (1985) (–); Permanent Form Solution to Fully Nonlinear Extended Boussinesq Equation of Chapter 3 (- -); Permanent Form Solution to Nonlinear Mild-Slope Equation of Chapter 2 (. .); Permanent Form Solution to Simplified Angular Spectrum Model of Extended Boussinesq Equation of Chapter 5 (-.). . . . 129

6.3 Contours of Instantaneous Free Surface Elevation, Simplified Extended Boussinesq Angular Spectrum Model, $\Lambda = 14.5°$. . . . 133

6.4 Contours of Instantaneous Free Surface Elevation, Simplified Extended Boussinesq Angular Spectrum Model, $\Lambda = 57.6°$. . . . 134

6.5 Comparisons of Parabolic KP Model of Liu et al. (1985) to Mach Stem Reflection Data, $\Lambda = 14.5°$. Gage Array Perpendicular to Wall. Numbers on Right Side are Gage Numbers. Data (–); KP Model (- -). 136

6.6 Comparisons of Parabolic KP Model of Liu et al. (1985) to Mach Stem Reflection Data, $\Lambda = 14.5°$. Gage Array Parallel to Wall. Numbers on Right Side are Gage Numbers. Data (–); KP Model (- -). 137

6.7 Comparisons of Angular Spectrum Boussinesq Model of Kirby (1990) to Mach Stem Reflection Data, $\Lambda = 14.5°$. Gage Array Perpendicular to Wall. Numbers on Right Side are Gage Numbers. Data (–); Angular Spectrum Model of Kirby (1990) (- -). 138

6.8 Comparisons of Angular Spectrum Boussinesq Model of Kirby (1990) to Mach Stem Reflection Data, $\Lambda = 14.5°$. Gage Array Parallel to Wall. Numbers on Right Side are Gage Numbers. Data (–); Angular Spectrum Model of Kirby (1990) (- -). 139

6.9 Comparison of Simplified Extended Boussinesq Angular Spectrum Model to Mach Stem Reflection Data, $\Lambda = 14.5°$. Gage Array Perpendicular to Wall. Numbers on Right Side are Gage Numbers. Data (–); Simplified Extended Boussinesq Angular Spectrum Model (- -). 140

6.10 Comparison of Simplified Extended Boussinesq Angular Spectrum Model to Mach Stem Reflection Data, $\Lambda = 14.5°$. Gage Array Parallel to Wall. Number on Right Side are Gage Numbers. Data (–); Simplified Extended Boussinesq Angular Spectrum Model (- -). 141

6.11 Comparisons of Parabolic KP Model of Liu et al. (1985) to Mach Stem Reflection Data, $\Lambda = 57.6°$. Gage Array Perpendicular to Wall. Numbers on Right Side are Gage Numbers. Data (–); KP Model (- -). 142

6.12 Comparisons of Parabolic KP Model of Liu et al. (1985) to Mach Stem Reflection Data, $\Lambda = 57.6°$. Gage Array Parallel to Wall. Numbers on Right Side are Gage Numbers. Data (–); KP Model (- -). 143

6.13 Comparisons of Angular Spectrum Boussinesq Model of Kirby (1990) to Mach Stem Reflection Data, $\Lambda = 57.6°$. Gage Array Perpendicular to Wall. Numbers on Right Side are Gage Numbers. Data (–); Angular Spectrum Model of Kirby (1990) (- -). 144

6.14 Comparisons of Angular Spectrum Boussinesq Model of Kirby (1990) to Mach Stem Reflection Data, $\Lambda = 57.6°$. Gage Array Parallel to Wall. Numbers on Right Side are Gage Numbers. Data (–); Angular Spectrum Model of Kirby (1990) (- -). 145

6.15 Comparisons of Simplified Extended Boussinesq Angular Spectrum Model to Mach Stem Reflection Data, $\Lambda = 57.6°$. Gage Array Perpendicular to Wall. Numbers on Right Side are Gage Numbers. Data (–); Simplified Extended Boussinesq Angular Spectrum Model (- -). 146

6.16 Comparisons of Simplified Extended Boussinesq Angular Spectrum Model to Mach Stem Reflection Data, $\Lambda = 57.6°$. Gage Array Perpendicular to Wall. Numbers on Right Side are Gage Numbers. Data (–); Simplified Extended Boussinesq Angular Spectrum Model (- -). 147

6.17 Comparison of $\overline{\rho'}$ for Three Models: Angular Spectrum Boussinesq Model of Kirby (1990) (–); Simplified Extended Boussinesq Angular Spectrum Model (- -); Parabolic KP Model of Liu et al. (1985) (. .). 151

6.18 Comparison of $\overline{e_{rms}}$ for Angular Spectrum Models: Angular Spectrum Boussinesq Model of Kirby (1990) (–); Simplified Extended Boussinesq Angular Spectrum Model (- -). 154

LIST OF TABLES

4.1 Wave Parameters of Experiment of Whalin (1971) Used In Data-Model Comparisons. ($h_1 = 45.7\ cm$; $h_2 = 15.2\ cm$.) 54

4.2 Table of Frequencies Analyzed for Error Comparison Between Shoaling Models Used for Case 2 of Mase and Kirby (1992) . . . 74

6.1 Gage Locations of Mach Stem Reflection Experiments of Hammack et al. (1990). 127

6.2 Paddle Phase Angles Λ and Directed Wave Angles Ψ. Model 1 is Kirby (1990); Model 2 is Simplified Extended Boussinesq Angular Spectrum Model 131

6.3 Correlation Coefficients ρ' (Each Gage and Average) for Parabolic KP Model Runs 149

6.4 Correlation Coefficients ρ' (Each Gage and Average) for Angular Spectrum Boussinesq Model of Kirby (1990). 150

6.5 Correlation Coefficients ρ' (Each Gage and Average) for Simplified Extended Boussinesq Angular Spectrum Model 150

6.6 Root-Mean-Square Error e_{rms} (Each Gage and Average) for Angular Spectrum Boussinesq Model of Kirby (1990) 153

6.7 Root-Mean-Square Error e_{rms} (Each Gage and Average) for Simplified Extended Boussinesq Angular Spectrum Model 154

Chapter 1

INTRODUCTION

The propagation of nonlinear water waves in shallow water has been investigated by numerous researchers during the last several years. The problem is significant from both a scientific and engineering point of view. It is mathematically and computationally demanding, since certain nonlinear effects which can be assumed small in deeper water become more important nearer the breaker line. It is also of considerable engineering importance, since sediment transport processes and longshore bar formation depend heavily on the nearshore wavefield.

Since Peregrine (1967) formulated one of the first applications of Boussinesq theory in the context of shallow water wave propagation over variable depth, much progress has been made on wave modeling in this area. Boussinesq theory is an advance on linear shallow water theory. Its formulation depends on weak dispersion (weak dependence of wave speed on frequency) and weak nonlinearity (small but finite amplitude). In contrast as well to the nonlinear long wave problem, these two weak dependencies are assumed to balance each other identically. Mathematically, this balance can be expressed by the Ursell number:

$$U_r = \frac{\delta}{\mu^2} \tag{1.1}$$

where δ is the nonlinearity parameter:

$$\delta = \frac{a_0}{h_0} \tag{1.2}$$

and μ is the dispersion parameter:

$$\mu = k_0 h_0 \tag{1.3}$$

where h_0 is a characteristic water depth, k_0 is a characteristic wave number, a_0 is a characteristic wave amplitude and g is gravitational acceleration. Thus, in shallow water, $\mu^2 \ll 1$, and the relative size of δ defines the classification of the wave theory in question:

1. $U_r << 1$ - Linear
2. $U_r = 1$ - Boussinesq
3. $U_r >> 1$ - Nonlinear long wave

It is the regime with $U_r = 1$ that is of immediate interest.

1.1 General Definition of Domain of Problem

Before we begin detailing existing theories, it would be prudent to discuss the domain, the coordinate system and some of the variables used in this study. We will consider a three-dimensional wave field propagating over a spatially-varying bottom. The Cartesian coordinate system (x, y, z) is located at the still water level, with z being positive upwards from the origin. The wave field is denoted in terms of the free surface elevation $\eta(x, y, t)$ (where t is time), which is defined relative to the still water level $z = 0$. The water depth is denoted $h(x, y)$. The flow is assumed to be irrotational, and the fluid is incompressible and inviscid.

1.2 Boussinesq Equations of Peregrine (1967) and Associated Models

Peregrine (1967) formulated the Boussinesq equations for variable depth. He started from the Euler equations, and then used an asymptotic expansion on the dependent variables. He carried the derivation to second order in velocity and free surface elevation, taking care to incorporate second-order terms in the first-order variables because these second-order effects become important in shallow water. Substituting these expansions into the Euler equations, integrating the vertical momentum equation and averaging the horizontal velocity over the depth leads to an equation for conservation of mass:

$$\eta_t + \nabla \cdot (h + \eta)\overline{\mathbf{u}} = 0 \tag{1.4}$$

and an equation for conservation of momentum:

$$\overline{\mathbf{u}}_t + \overline{\mathbf{u}} \cdot \nabla_h \overline{\mathbf{u}} + g \nabla_h \eta = \frac{h}{2} \nabla_h [\nabla_h \cdot (h \overline{\mathbf{u}}_t)] - \frac{h^2}{6} \nabla_h [\nabla_h \cdot \overline{\mathbf{u}}] \tag{1.5}$$

where $\overline{\mathbf{u}}$ is the depth-averaged horizontal velocity, ∇_h refers to the the horizontal gradient operator in (x, y), and the subscript t denotes differentiation with respect to time. In the context of this study, Equations (1.4) and (1.5) will often be referred to as the "standard" Boussinesq equations of Peregrine (1967). Implicit in the derivation of (1.4) and (1.5) is a quadratic variation in horizontal velocity with depth and a linear decrease in vertical velocity with an increase in depth. This vertical velocity is much smaller in magnitude than the horizontal velocity. The dispersion relation for the Boussinesq equations is:

$$\omega^2 = \frac{g k^2 h}{\left[1 + \frac{1}{3}(kh)^2\right]} \tag{1.6}$$

where k is the wave number.

The Korteweg-deVries (KdV) equation and the Kadomtsev-Petviashvili (KP) equations are wave equations (with η as their only dependent variable) which are essentially reductions of the Boussinesq equations (1.4) and (1.5). The KdV equation for variable depth was formulated by Svendsen (1976):

$$\frac{1}{c}\eta_t + \eta_x + \frac{h_x}{4h}\eta + \frac{3}{2h}\eta\eta_x + \frac{h^2}{6}\eta_{xxx} = 0 \tag{1.7}$$

where the subscripts x and y refer to differentiation with respect to x and y, respectively. This equation is exactly integrable for the case of a flat bottom. Solutions are expressible in terms of the Jacobian *cn* elliptic functions; hence, these permanent-form solutions are called *cnoidal waves.* The KdV equation is limited to one-dimensional wave propagation. The variable depth KP equation was first developed by Liu et al. (1985):

$$\left(\frac{1}{c}\eta_t + \eta_x + \frac{h_x}{4h}\eta + \frac{3}{2h}\eta\eta_x + \frac{h^2}{6}\eta_{xxx}\right)_x + \frac{1}{2h}(h\eta_y)_y = 0 \tag{1.8}$$

This equation is also exactly integrable for a flat bottom; solutions are expressed in terms of Riemann theta functions (e.g., Segur and Finkel 1985). The dispersion relation associated with the KdV and KP models is:

$$\omega = \sqrt{gh}k\left[1 - \frac{1}{6}(kh)^2\right] \tag{1.9}$$

The dispersion relations (1.6) and (1.9) are essentially two-term expansions of the dispersion relation from linear theory:

$$\omega^2 = gk\tanh kh \tag{1.10}$$

All three dispersion relations are asymptotically equal in shallow water ($kh \ll 1$), but exhibit different behavior in intermediate or deep water. Figure (1.1) shows the ratio of the wave celerity to the shallow water wave speed against the parameter kh. It is apparent that the three dispersion relations tend toward the shallow water wave speed (ratio $\frac{C}{\sqrt{gh}}$ approaching unity) in shallow water but diverge rapidly as kh increases.

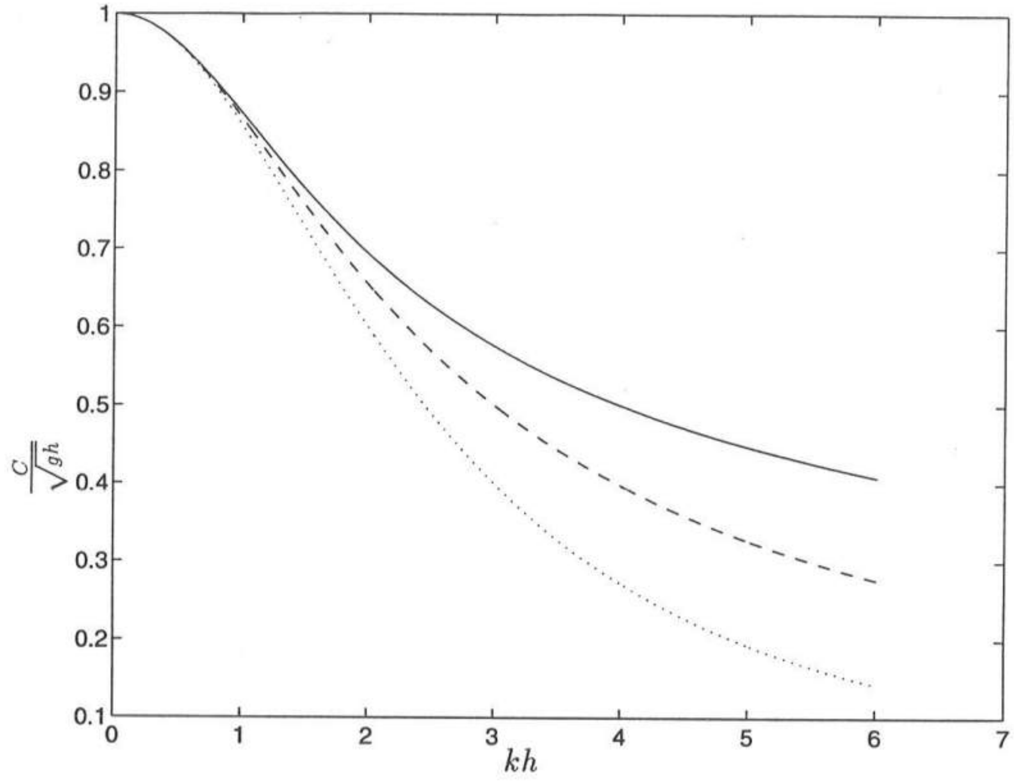

Figure 1.1: Comparison of Three Dispersion Relations. Linear Dispersion Relation (–); Dispersion Relation of the Boussinesq Equations (- -); Dispersion Relation of the KdV Equation (..).

1.3 Implications of the Shallow Water Assumption

The models described in the previous section (and their frequency-domain counterparts) are fairly robust models of nonlinear water wave propagation in shallow water as long as $kh \ll 1$. Violation of this assumption can produce erroneous predictions of such first-order quantities as wave shoaling and celerity. We saw in the previous section that weakly-dispersive wave celerity deviates from that of linear theory in deeper water. As for shoaling, the mechanism inherent in a *consistent* frequency-domain treatment of the Boussinesq equations (e.g., the "consistent" model of Freilich and Guza 1984) is Green's Law:

$$\left(\frac{a}{a_0}\right) = \left(\frac{h}{h_0}\right)^{\frac{1}{4}} \tag{1.11}$$

which predicts a monotonic increase in wave amplitude with a decrease in depth. (The word "consistent" in this sense means that all the terms of the equation are valid to the same order of approximation.) As will be shown in later chapters of this study, this usually results in an overprediction of amplitude for waves not in shallow water. This is the situation when a wind-wave spectrum, for example, has frequency components which are actually in intermediate or deep water ($\mu^2 = O(1)$), even though the peak frequency component may be in shallow enough water to validate the use of the Boussinesq equation.

This study investigates two different approaches to circumvent the problems associated with the assumption of shallow water in these weakly-nonlinear models. One method (outlined in Chapter 2) involves the formulation of a weakly-nonlinear mild-slope equation, which uses full linear theory for its dispersion and transformation properties. The resulting model thus has linear properties which are applicable to all water depths, and the same degree of nonlinearity found in the Boussinesq models. The second approach (detailed in Chapter 3) involves the formulation of a fully nonlinear extended Boussinesq equation. The linear dispersion relation associated with these extended Boussinesq models is accurate to $O(\mu^2)$ as with the Boussinesq models of the previous section, but is of such a form that it can mimic the properties of the full linear dispersion relation (1.10) for a wide range of water depths. This model represents an advance over existing extended Boussinesq models in that it is fully nonlinear, so that dispersive terms are retained in the nonlinear parts of the equations. This has important implications for modeling superharmonic and subharmonic energy transfer in a random second-order sea (Kirby and Wei 1994). Both models will be treated in the frequency domain in one-dimensional and parabolic two-dimensional forms, and compared to data in Chapter 4. We make an additional assumption of longshore periodicity in Chapter 5, and develop both a simplified angular spectrum model with improved dispersion characteristics and an angular spectrum treatment of the fully nonlinear extended Boussinesq equations. Comparisons to data will follow in Chapter 6. Conclusions and recommendations for further study will be discussed in Chapter 7.

Chapter 2

NONLINEAR MILD-SLOPE EQUATION

2.1 Introduction

The principal aim of this chapter is to derive a set of time-periodic, spatially varying nonlinear mild slope equations to govern the evolution of a wavefield propagating from deep to shallow water. The *linear* mild-slope equation (Berkhoff 1972; Smith and Sprinks 1975) is well entrenched in the literature, and has been solved by a variety of methods. Because the equation is elliptic, prior specification of the conditions on the *entire* boundary is required. This is generally not possible for an open coastal region. Additionally, fine resolution is required to resolve the wave field sufficiently. The parabolic approximation (Radder 1979; Lozano and Liu 1980) has eased the computational demands somewhat by reducing the boundary value problem to an initial value parabolic problem, where only lateral boundaries and the initial condition need be specified and the solution allowed to march forward in the propagation direction. This solution technique is somewhat problematic (it is limited by, for example, an assumption of a small angle of approach), but is sufficiently accurate for modeling waves in a straight wave flume with two-dimensional topography, which is our primary two-dimensional application for both this model and the model to be explained in the next chapter. Several investigators have previously worked on models similar to the one described in this chapter. Bryant (1973, 1974) formulated a model from the boundary value problem for water waves over a flat bottom by specifying spatially periodic Fourier expansions for the variables ϕ and η which would satisfy the Laplace equation and the bottom boundary condition, substituting these into the two free surface boundary conditions, and then integrating to solve for the amplitude coefficients, which vary slowly in time. The interaction coefficients which would determine the degree of energy exchange among resonant triads were derived without restrictions on the size of the dispersion parameter μ. However, the time-varying, spatially periodic formulation is not suitable for most applications, since spectral wave information is usually taken and stored by means of a frequency-domain Fast Fourier Transform (FFT), which presupposes equal intervals of frequencies rather than wave numbers. Keller (1988) developed a set of equations describing the evolution of two interacting wave components. He demonstrated that, in the nondispersive limit, this same set of evolution equations can be derived from the exact Euler equations, the nonlinear shallow water equations, and the Boussinesq equations. The model described in this section would match his model before the nondispersive limit is taken if the number of frequency components is truncated to two and slow time dependence is reincorporated. Agnon et al. (1993) derived a one-dimensional nonlinear shoaling model for time-periodic, spatially varying waves from the boundary value problem. Their model is similar in form to the one-dimensional model described in this chapter. Specific differences and similarities between Agnon et al. (1993) and the present model will be described in a later section in this chapter.

2.2 Boundary Value Problem

Here we use the water wave boundary value problem for the velocity potential ϕ:

$$\nabla^2\phi = \nabla_h^2\phi + \phi_{zz} = 0; \qquad -h \le z \le \eta \tag{2.1}$$

$$\phi_z = -\nabla_h h \cdot \nabla_h \phi; \qquad z = -h \tag{2.2}$$

$$g\eta + \phi_t + \frac{1}{2}(\nabla_h\phi)^2 + \frac{1}{2}(\phi_z)^2 = 0 \qquad z = \eta \tag{2.3}$$

$$\eta_t - \phi_z + \nabla_h\eta \cdot \nabla_h\phi = 0; \qquad z = \eta \tag{2.4}$$

where all pertinent variables were defined in Chapter 1. The water depth is assumed to be slowly varying to such a degree that local values of wave-related parameters can be used.

We wish to retain leading order nonlinearity in the free surface boundary conditions. Rather than scale and nondimensionalize the problem, we retain dimensional quantities and implicitly order the problem such that it is understood that leading order nonlinearity is $O(\epsilon^2)$, where $\epsilon(=ka$, where k is the wave number and a is a characteristic wave amplitude) is the nonlinearity parameter. The free surface boundary conditions are both nonlinear and applied at a position not known *a priori*; thus we expand these in Taylor series about $z = 0$ and retain terms to $O(\epsilon^2)$. The truncated boundary value problem is now:

$$\nabla_h^2\phi + \phi_{zz} = 0; \qquad -h \le z \le 0 \tag{2.5}$$

$$\phi_z = -\nabla_h h \cdot \nabla_h \phi; \qquad z = -h \tag{2.6}$$

$$g\eta + \phi_t + \frac{1}{2}(\nabla_h\phi)^2 + \frac{1}{2}(\phi_z)^2 + \eta\phi_{zt} = O(\epsilon^3); \qquad z = 0 \tag{2.7}$$

$$\eta_t - \phi_z + \nabla_h\eta \cdot \nabla_h\phi - \eta\phi_{zz} = O(\epsilon^3); \qquad z = 0 \tag{2.8}$$

Instead of using the approach of Bryant (1973), whereby he substituted an appropriate form for ϕ that would satisfy the Laplace equation and the bottom boundary condition, we instead use the approach of Smith and Sprinks (1975), who used Green's second identity to derive a linear mild-slope equation. We first assume a superposition of solutions:

$$\phi(x,y,z,t)=\sum_{n=1}^{N} f_n(k_n,h,z)\tilde{\phi}_n(k_n,\omega_n,x,y,t) \tag{2.9}$$

where ω_n is the radian frequency and k_n is the wave number of the n^{th} frequency component, and:

$$f_n=\frac{\cosh k_n(h+z)}{\cosh k_n h} \tag{2.10}$$

or the usual depth dependence dictated by linear theory. The frequency ω_n and the wave number k_n are related by the linear dispersion relation:

$$\omega_n^2=gk_n\tanh k_n h \tag{2.11}$$

It is convenient to combine the two surface boundary conditions (2.7) and (2.8) into a single equation for ϕ only. Eliminating η from the surface boundary conditions leads to:

$$\phi_z=-\frac{1}{g}\left[\phi_{tt}+\frac{1}{2}(\nabla_h\phi)_t^2+\frac{1}{2}(\phi_z)_t^2-\frac{1}{2g}(\phi_t)_{zt}^2+\nabla_h\cdot(\phi_t\nabla_h\phi)\right];\quad z=0 \tag{2.12}$$

In the manner of Smith and Sprinks (1975), we will use Green's second identity on the variables f_n and $\tilde{\phi}_n$, as follows:

$$\nabla_h\cdot\left(\int_{-h}^{0} f_n^2 dz\nabla_h\tilde{\phi}_n\right)-\int_{-h}^{0} f_{nz}^2 dz\tilde{\phi}_n=-f_n\tilde{\phi}_{nz}\mid_{z=0}+O(\epsilon,\alpha^2) \tag{2.13}$$

where α is a parameter characterizing the bottom slope. For our purposes it is assumed that

$$\alpha\leq\ O(\epsilon) \tag{2.14}$$

In this manner we can eliminate bottom boundary terms in comparison to $O(\epsilon^2)$ terms from the free surface. Development of the linear part of the models is identical to Smith and Sprinks (1975); reference is made to their paper. We simply note that:

$$\begin{aligned}
f_n(0) &= 1 && (2.15)\\
f_{nz}(0) &= \frac{\omega_n^2}{g} && (2.16)\\
\int_{-h}^{0} f_n^2 dz &= \frac{(CC_g)_n}{g} && (2.17)\\
\int_{-h}^{0} (f_{nz})^2 dz &= \frac{\omega_n^2}{g}\left(1-\frac{C_{gn}}{C_n}\right) && (2.18)
\end{aligned}$$

where C_n is the wave celerity and C_{gn} the group velocity of the n^{th} component. The subscript z refers to partial differentiation with respect to z. Substituting (2.9), (2.12), (2.15), (2.16), (2.17), and (2.18) into (2.13) yields a time-dependent mild-slope equation with nonlinear coupling between modes:

$$\begin{aligned}
&\tilde{\phi}_{tt} - \nabla_h \cdot \left[(CC_g)_n \nabla_h \tilde{\phi}_n\right] + \omega_n^2 \left(1-\frac{C_{gn}}{C_n}\right)\tilde{\phi}_n \\
= \; & \frac{1}{2}\left\{\sum_l \sum_m \left[\frac{\omega_l^2+\omega_m^2}{g^2}(\tilde{\phi}_{l_t}\tilde{\phi}_{m_t})_t - \frac{\omega_l^2\omega_m^2}{g^2}(\tilde{\phi}_l\tilde{\phi}_m)_t\right]\right. \\
- \; & \left.\sum_l \sum_m \left[(\nabla_h\tilde{\phi}_l \cdot \nabla_h\tilde{\phi}_m)_t + \nabla_h \cdot (\tilde{\phi}_{l_t}\nabla_h\tilde{\phi}_m) + \nabla_h \cdot (\tilde{\phi}_{m_t}\nabla_h\tilde{\phi}_l)\right]\right\}_n \qquad (2.19)
\end{aligned}$$

where the nonlinear summations on the right-hand side contain only terms that oscillate near the frequency ω_n. Despite the fact that we have decomposed the wavefield into individual components, we have not made any assumptions concerning the behavior of these components; they could represent propagating or standing waves with characteristics that vary slowly in time and space. It is noted here that as ϵ approaches zero, Equation (2.19) approaches a representation of decoupled, independent waves. In the shallow water limit (as $k_n h$ approaches zero) we approach a frequency-domain representation of Boussinesq-type shallow water waves. Additionally, Bryant (1974) showed that a system like Equation (2.19), with coefficients expressed as a power series in ϵ, will join smoothly to a solution for Stokes waves in deep water for $N = 3$ components.

2.3 Resonant Triad Interaction

In order to completely transform the equations into the frequency domain, we must assume periodicity in time and factor out this time dependence. This will allow us to formulate evolution equations for the spatially varying amplitudes of the wave components. Thus, it would be in order to embark on a brief discussion of triad resonant interactions. This discussion is an overview of Section 2.8 of Phillips (1977); reference is made to his work for more detailed explanations. Implications of triad resonance interactions will be described later in this chapter. We note here that the notation and ordering presented in this section applies to this section only, and will not enter our discussion of the model formulation.

The combined boundary condition (2.8) is truncated to $O(\epsilon^2)$. This retains quadratic nonlinearity (squares or products of unknowns). Due to this quadratic nonlinearity we can investigate the interactions of three wave modes of the wave field. If we had to retain *cubic* nonlinearity, we would need to turn to four wave interactions.

We can symbolically represent small perturbations to the linear approximation of the water wave problem as:

$$\mathcal{L}(p) = \hat{\epsilon}\mathcal{N}(p) \tag{2.20}$$

where $\hat{\epsilon}$ is a small parameter representing the wave amplitude, $\mathcal{L}$ is a linear operator, $\mathcal{N}$ is a nonlinear operator, and p is some local property of the wavefield. The exact nature of $\mathcal{L}$ and $\mathcal{N}$ depends on the problem being considered. We will assume that the *linear* part of a spatially uniform solution for p is in the form of a plane wave:

$$p = \frac{1}{2}\left[a_n(\hat{\epsilon}\omega t)e^{i\psi_n} + a_n^*(\hat{\epsilon}\omega t)e^{-i\psi_n}\right] \tag{2.21}$$

where the asterisk denotes the complex conjugate amplitude. This assumption ensures that p remains real. The phase function ψ is:

$$\psi = (\vec{k} \cdot \vec{x} - \omega t) \tag{2.22}$$

where $\vec{k}$ is the wave number vector. We allow a and a^* to vary slowly in time, and allow ω and $\vec{k}$ to satisfy the linear dispersion relation. Addressing the nonlinear problem, we can examine the interaction of three wave modes and presuppose a solution for p in the following form:

$$p = \sum_{n=1}^{3} \frac{1}{2} \left[a_n(\hat{\epsilon}\omega t) e^{i\psi_n} + a_n^*(\hat{\epsilon}\omega t) e^{-i\psi_n} \right] + \hat{\epsilon} P \tag{2.23}$$

where $\hat{\epsilon}P$ represents small nonlinear corrections to the linear problem at $O(\hat{\epsilon})$. Thus, at $O(\hat{\epsilon})$, the quadratic terms in the nonlinear operator $\mathcal{N}$ gives rise to products of amplitudes:

$$a_l a_m e^{i(\psi_l + \psi_m)} \tag{2.24}$$

$$a_l a_m^* e^{i(\psi_l - \psi_m)} \tag{2.25}$$

$$a_l^* a_m e^{i(-\psi_l + \psi_m)} \tag{2.26}$$

$$a_l^* a_m^* e^{i(-\psi_l - \psi_m)} \tag{2.27}$$

Because the homogeneous solution for P resembles:

$$P_h \sim \frac{b_n}{2} e^{i\psi_n} + c.c. \tag{2.28}$$

(where *c.c.* denotes the complex conjugate) the product terms will oscillate at ψ_n if any of the following conditions are satisfied:

$$\psi_n = \psi_l + \psi_m \tag{2.29}$$

$$\psi_n = \psi_l - \psi_m \tag{2.30}$$

$$\psi_n = -\psi_l + \psi_m \tag{2.31}$$

$$\psi_n = -\psi_l - \psi_m \tag{2.32}$$

implying:

$$\vec{k}_n = \vec{k}_l + \vec{k}_m \tag{2.33}$$

$$\vec{k}_n = \vec{k}_l - \vec{k}_m \tag{2.34}$$

$$\vec{k}_n = -\vec{k}_l + \vec{k}_m \tag{2.35}$$

$$\vec{k}_n = -\vec{k}_l - \vec{k}_m \tag{2.36}$$

and

$$\omega_n = \omega_l + \omega_m \tag{2.37}$$

$$\omega_n = \omega_l - \omega_m \tag{2.38}$$

$$\omega_n = -\omega_l + \omega_m \tag{2.39}$$

$$\omega_n = -\omega_l - \omega_m \tag{2.40}$$

In order to completely factor out the time dependence, (2.37), (2.38), (2.39) and (2.40) must be satisfied so that the differences in the frequency portion of the phase function ψ cancel. This is resonant triad interaction among three frequency components, and the interaction coefficients that arise from substitution of this resonance condition into the time derivatives in the nonlinear right-hand side of (2.19) determine the energy exchange between the three interacting modes. Thus, transforming a set of equations with quadratic nonlinearities requires resonant triad interactions among frequency components to factor out the time dependence.

2.4 Time-Harmonic Wave Propagation in Two Dimensions

We wish to develop a series of evolution equations for the propagation of time-harmonic waves in two spatial dimensions. Hence, we can factor out the time dependence by assuming:

$$\tilde{\phi}_n(x,y,t) = \frac{\hat{\phi}_n}{2} e^{-i\omega_n t} + \frac{\hat{\phi}_n^*}{2} e^{i\omega_n t} \tag{2.41}$$

and using the concept of resonant triad interactions discussed in the previous section. This yields a time-harmonic wave equation with modification by nonlinearity:

$$\begin{aligned}
&\nabla_h \cdot \left[(CC_g)_n \nabla_h \hat{\phi}_n\right] + k_n^2 (CC_g)_n \hat{\phi}_n = -\frac{i}{4} \left[\sum_{l=1}^{n-1} 2\omega_n \nabla_h \hat{\phi}_l \cdot \nabla_h \hat{\phi}_{n-l} \right. \\
+ &\left. \omega_l \hat{\phi}_l \nabla_h^2 \hat{\phi}_{n-l} + \omega_{n-l} \hat{\phi}_{n-l} \nabla_h^2 \hat{\phi}_l + \frac{\omega_l \omega_{n-l} \omega_n}{g^2} (\omega_l^2 + \omega_l \omega_{n-l} + \omega_{n-l}^2) \hat{\phi}_l \hat{\phi}_{n-l} \right] \\
- &\frac{i}{2} \left[\sum_{l=1}^{N-n} 2\omega_n \nabla_h \hat{\phi}_l^* \cdot \nabla_h \hat{\phi}_{n+l} + \omega_{n+l} \hat{\phi}_{n+l} \nabla_h^2 \hat{\phi}_l^* - \omega_l \hat{\phi}_l^* \nabla_h^2 \hat{\phi}_{n+l} \right. \\
- &\left. \frac{\omega_l \omega_{n+l} \omega_n}{g^2} (\omega_l^2 - \omega_l \omega_{n+l} + \omega_{n+l}^2) \hat{\phi}_l^* \hat{\phi}_{n+l} \right]
\end{aligned} \tag{2.42}$$

While we have incorporated an assumption for time periodicity into our problem, we have not explicitly specified the spatial variation of the wavefield. Equation (2.42) can describe standing or propagating waves, or any combination. Additionally, (2.42) is elliptic, with the linear terms being essentially the elliptic mild-slope equation models of Berkhoff (1972) and Smith and Sprinks (1975). The computational difficulties associated with elliptic models have been discussed earlier in this chapter.

2.5 Parabolic Approximation

We will restrict the problem to that of a progressive wave field with the following form:

$$\hat{\phi}_n(x,y) = -\frac{ig}{\omega_n} A_n(x,y) e^{i\int k_n(x,y)dx} \tag{2.43}$$

$$\hat{\phi}_n^*(x,y) = \frac{ig}{\omega_n} A_n^*(x,y) e^{-i\int k_n(x,y)dx} \tag{2.44}$$

where the complex amplitude A_n is assumed to be a slowly varying function of the spatial coordinates (x, y), and the wave is assumed to be traveling primarily in the x direction. Substituting (2.44) into (2.42) gives:

$$\begin{aligned} & [(CC_g)_n A_{nx}]_x + 2i(kCC_g)_n A_{nx} + i(kCC_g)_{nx} A_n \\ + & \left[(CC_g)_n \left(A_n e^{i\int k_n(x,y)dx}\right)_y\right]_y e^{-i\int k_n(x,y)dx} \\ = & \frac{1}{4}\sum_{l=1}^{n-1} RA_l A_{n-l} e^{i\int(k_l+k_{n-l}-k_n)dx} + \frac{1}{2}\sum_{l=1}^{N-n} SA_l^* A_{n+l} e^{i\int(k_{n+l}-k_l-k_n)dx} \end{aligned} \tag{2.45}$$

where

$$R = \frac{g}{\omega_l \omega_{n-l}}\left[\omega_n^2 k_l k_{n-l} + (k_l + k_{n-l})(\omega_{n-l} k_l + \omega_l k_{n-l})\omega_n\right] - \frac{\omega_n^2}{g}(\omega_l^2 + \omega_l \omega_{n-l} + \omega_{n-l}^2) \tag{2.46}$$

$$S = \frac{g}{\omega_l \omega_{n+l}}\left[\omega_n^2 k_l k_{n+l} + (k_{n+l} - k_l)(\omega_{n+l} k_l + \omega_l k_{n+l})\omega_n\right] - \frac{\omega_n^2}{g}(\omega_l^2 - \omega_l \omega_{n+l} + \omega_{n+l}^2) \tag{2.47}$$

Equation (2.45) is still elliptic, so we need to explicitly invoke the parabolic approximation. We have assumed that the wave propagates primarily in the x-direction, so that we retain fast wave-like variations in the x-direction but not in the y-direction. The fast variations in the x-direction are accounted for by the complex exponential in Equations (2.43) and (2.44). We use the scaling approach of Yue and Mei (1980) to order the derivatives of A_n as follows:

$$\frac{\partial A_n}{\partial x} = O(\epsilon^2) \tag{2.48}$$

$$\frac{\partial A_n}{\partial y} = O(\epsilon) \tag{2.49}$$

since the fast variations in x have already been factored out. The ordering of the y-derivative in (2.49) allows us to keep $\frac{\partial^2 A_n}{\partial y^2}$, thereby allowing us to model the slow phase-like variations of the wave in the y-direction that occur when it is turned at a small angle to the x-direction. Additionally, since we assume the wave to propagate primarily in the x-direction, changes in the amplitude A_n would be due mostly to x-derivatives of the depth h. Thus, the order of bottom slope in the x-direction (h_x), as well as x-derivatives of depth-dependent properties (e.g., C, C_g), should also be $O(\epsilon^2)$. This allows us to set the relative amplitudes of the first two terms of Equation (2.45) as:

$$\epsilon^4[(CC_g)_n A_{nx}]_x \ll \epsilon^2[2i(kCC_g)_n A_{nx}] \tag{2.50}$$

where the subscript x refers to differentiation with respect to x. Since we are keeping terms to $O(\epsilon^2)$ we drop the first term in Equation (2.47). Additionally, we need to factor out any y dependence from the phase function. This must be done since we are only integrating the phase in x, but the wavenumber k_n is a function of both x and y. There are several ways to address this; we choose the method of Lozano and Liu (1980), whereby they defined a y-averaged wavenumber $\overline{k}_{n0}(x)$ as a reference phase function. Thus, we rewrite (2.43) and (2.44) as:

$$\hat{\phi}_n(x,y) = -\frac{ig}{\omega_n} a_n(x,y) e^{i\int \overline{k}_{n0}(x)dx} \tag{2.51}$$

$$\hat{\phi}_n(x,y) = \frac{ig}{\omega_n} a_n^*(x,y) e^{-i\int \overline{k}_{n0}(x)dx} \tag{2.52}$$

which gives:

$$A_n(x,y) = a_n(x,y) e^{i(\int \overline{k}(x)_{n0}dx - \int k_n(x,y)dx)} \tag{2.53}$$

and:

$$A_n^*(x,y) = a_n^*(x,y) e^{-i(\int \overline{k}(x)_{n0}dx - \int k_n(x,y)dx)} \tag{2.54}$$

Substituting this into (2.45) yields:

$$\begin{aligned} & 2i(kCC_g)_n a_{nx} - 2(kCC_g)_n(\overline{k}_{n0} - k_n)a_n + i(kCC_g)_{nx}a_n + [(CC_g)_n(a_n)_y]_y \\ = \; & \frac{1}{4}\left(\sum_{l=1}^{n-1} Ra_l a_{n-l} e^{i\int(\overline{k}_{l0}+\overline{k}_{n-l0}-\overline{k}_{n0})dx} + 2\sum_{l=1}^{N-n} Sa_l^* a_{n+l} e^{i\int(\overline{k}_{n+l0}-\overline{k}_{l0}-\overline{k}_{n0})dx}\right) \end{aligned} \tag{2.55}$$

This is our parabolic model of the nonlinear mild-slope equation. In Chapter 4 we will compare this model to the parabolic KP frequency-domain model of Liu et al. (1985), so we write that model here:

$$\begin{aligned} & 2ink_o A_{nx} + \frac{k_o}{kG_n}(hA_{ny})_y + \frac{A_n}{G_n}\left[\frac{ink_o}{2}G_{nx} - 2n^2k_o(k_o - k)G_n + \frac{n^4k_o\omega^4h}{3g^2k}\right] \\ = \; & \frac{3n^2kk_o}{4G_n}\left(\sum_{l=1}^{n-1} A_l A_{n-l} + 2\sum_{l=1}^{N-n} A_l^* A_{n+l}\right) \end{aligned} \tag{2.56}$$

where k_o is a constant reference wave number and:

$$G_n = h\left(1 - \frac{n^2\omega^2h}{3g}\right) \tag{2.57}$$

This model has lowest-order Green's Law shoaling. We will also use the one-dimensional version of Equation (2.55) in our applications:

$$\begin{aligned} & A_{nx} + \frac{(kCC_g)_{nx}}{2(kCC_g)_n}A_n = \\ - \; & \frac{i}{8(kCC_g)_n}\left(\sum_{l=1}^{n-1} RA_l A_{n-l} e^{i\int(k_l+k_{n-l}-k_n)dx} + 2\sum_{l=1}^{N-n} SA_l^* A_{n+l} e^{i\int(k_{n+l}-k_l-k_n)dx}\right) \end{aligned} \tag{2.58}$$

where we revert back to the A_n notation because the reference wavenumber $\overline{k}_{n0}$ is identical to k_n. Equation (2.58) will be referred to as the "fully dispersive nonlinear shoaling model" in later chapters. Taking Equation (2.58) to its shallow water limit yields:

$$A_{nx} + \frac{h_x}{4h}A_n - \frac{in^3k^3h^2}{6}A_n + \frac{3ink}{8h}\left(\sum_{l=1}^{n-1} A_l A_{n-l} + 2\sum_{l=1}^{N-n} A_l^* A_{n+l}\right) = 0 \tag{2.59}$$

which is essentially the "consistent shoaling model" of Freilich and Guza (1984). Integration of the first two terms of Equation (2.59) yields Green's Law (Equation 1.11). We use Equation (2.59) in our data-model comparisons in the next chapter.

The two-dimensional parabolic equation (2.55) was modeled with the Crank-Nicholson numerical scheme. This scheme is unconditionally stable for linear problems, and is second-order accurate in x and y. The parabolic model (2.55) was converted to finite differences much like the KP model of Liu et al. (1985), where the numerical scheme was written out; thus, it will not be shown here. The one-dimensional shoaling model (2.58) was modeled with a fourth-order Runge-Kutta scheme with a variable step-size adaptor (Press, et al. 1986).

2.6 Comparison with Agnon et al. (1993)

As mentioned previously in this chapter, Agnon et al. (1993) developed a one-dimensional shoaling model based on the same concepts employed by the present model, but using a different approach. They divided the solution into free waves, which satisfy the linear dispersion relation, and "locked" waves, which do not satisfy the linear dispersion relation and are forced by the interactions of two free waves. It was reasoned that the "locked" waves would travel bound to the sum or difference of the two forcing frequencies in deep water. As the water depth decreases, the "locked" waves begin to propagate at the same speed as their free wave counterparts, and the interaction becomes resonant, with the forced component no longer limited to be smaller in amplitude to the forcing components. Rather than using a discrete Fourier transform for the frequency-domain tranformation, they used a continuous Fourier integral, which required the use of a delta function to pick out the resonant frequencies. For the periodic form of their dependent variable ϕ, they used:

$$\phi = \int_{-\infty}^{\infty} \hat{\phi} e^{-iwt} dt \tag{2.60}$$

which is the continuous form of (2.41), except for a factor of 2. After substituting this into their equations they then assume the following form for $\hat{\phi}$:

$$\hat{\phi} = A e^{i \int k dx} \tag{2.61}$$

This is different from (2.43) in that the complex factor $\frac{ig}{\omega_n}$ present in (2.43) allows us to model the amplitude of the free surface elevation η rather than ϕ, at least to first order. The evolution equation of Agnon et al. (1993) for the amplitudes of ϕ are:

$$\begin{aligned} &A_{nx} + \frac{C_{gnx}}{2C_{gn}} A_n = \\ &- \frac{i}{C_{gn}} \left(\sum_{l=1}^{n-1} \pi V_1 A_l A_{n-l} e^{i \int (k_l + k_{n-l} - k_n) dx} - 2 \sum_{l=1}^{N-n} \pi V_2 A_l^* A_{n+l} e^{i \int (k_{n+l} - k_l - k_n) dx} \right) \end{aligned} \tag{2.62}$$

where the interaction coefficients are:

$$V_1 = \frac{1}{4\pi} \left(2k_l k_{n-l} + \frac{\omega_l^2 \omega_{n-l}^2}{g^2} + \frac{k_l^2 \omega_{n-l}}{\omega_n} + \frac{k_{n-l}^2 \omega_l}{\omega_n} - \frac{\omega_n^2 \omega_l \omega_{n-l}}{g^2} \right) \tag{2.63}$$

and:

$$V_2 = \frac{1}{4\pi} \left(2k_l k_{n+l} + \frac{\omega_l^2 \omega_{n+l}^2}{g^2} + \frac{k_l^2 \omega_{n+l}}{\omega_n} - \frac{k_{n+l}^2 \omega_l}{\omega_n} + \frac{\omega_n^2 \omega_l \omega_{n+l}}{g^2} \right) \tag{2.64}$$

If we use (2.43) to recast (2.62) so that we model the amplitudes of η (here denoted a_n) instead of those of ϕ, we obtain (after some rearrangement):

$$\begin{aligned} &a_{nx} + \frac{C_{gnx}}{2C_{gn}} a_n = \\ &- \frac{i}{4\omega_n C_{gn}} \left(\sum_{l=1}^{n-1} \mathcal{V}_1 a_l a_{n-l} e^{i \int (k_l + k_{n-l} - k_n) dx} + 2 \sum_{l=1}^{N-n} \mathcal{V}_2 a_l^* a_{n+l} e^{i \int (k_{n+l} - k_l - k_n) dx} \right) \end{aligned} \tag{2.65}$$

where:

$$\mathcal{V}_1 = \frac{g\pi\omega_n^2}{\omega_l\omega_{n-l}}V_1 \tag{2.66}$$

and

$$\mathcal{V}_2 = \frac{g\pi\omega_n^2}{\omega_l\omega_{n+l}}V_2 \tag{2.67}$$

It can be shown that $\mathcal{V}_1$ and $\mathcal{V}_2$ are exactly equal to R from (2.46) and S from (2.47), respectively. Allowing for the aforementioned difference of a factor of 2 from the definition of the Fourier transform of ϕ, we find that (2.65) is equal to (2.58). Thus, our model is an extension of Agnon et al. (1993) in that it allows for two horizontal dimensions; the characteristics of one-dimensional wave propagation and nonlinearity are the same between the two models. The one-dimensional and parabolic two-dimensional models will be compared to data in Chapter 4.

2.7 Implications of Resonant Triad Interaction Theory

As previously mentioned, we made use of resonant triad interactions to treat the quadratic nonlinear terms. This assumes that retention of *only* resonant interactions between triads of frequency components is sufficient to adequately describe a wave field. This assumption marks a departure from time-domain modeling, in which all interactions, resonant or non-resonant, between frequencies are retained, since there is no explicit distinction between them. One of the consequences of the use of resonant interaction theory is the assumption of slow variation in time and/or space. Because the nonlinear terms oscillate at the same frequency as the linear terms (written schematically in Equation 2.23), singular perturbation theory maintains that we can formulate a multiple-scale solution in terms of a slowly varying amplitude and fast varying phase. This was assumed in (2.43) and (2.44). It would stand to reason, then, that the arguments in the complex exponentials in (2.58) remain small, such that the slowly-varying assumption is satisfied. These arguments are:

$$k_l + k_{n-l} - k_n \tag{2.68}$$

and:

$$k_{n+l} - k_l - k_n \tag{2.69}$$

If, for the sake of illustration, we wish to look at the interactions between a frequency component ω_1 and itself for a two-component system, we could write (2.58) for the amplitude of the second harmonic A_2 as follows:

$$A_{2x} + \frac{(kCC_g)_{2x}}{2(kCC_g)_2} A_2 = -\frac{i}{8(kCC_g)_2}\left(RA_1^2 e^{i\int(k_2-2k_1)dx}\right) \tag{2.70}$$

The phase function $k_2 - 2k_1$ (often referred to as "phase mismatch") is the difference in the phases between the free second harmonic k_2 and the bound second harmonic $2k_1$. In order for the slowly-varying assumption to remain valid, this difference must remain small. In shallow water, it is indeed small, as the bound second harmonic begins to satisfy the linear dispersion relation and become a free wave. In deeper water, however, this difference can become quite large. It is instructive to quantify this difference in terms of a nondimensional mismatch; thus we define:

$$\chi = \frac{\mid k_2 - 2k_1 \mid}{k_1} \tag{2.71}$$

so that we can determine the relative size of the mismatch. Figure 2.1 shows the trend in χ as $\frac{h}{L_0}$ increases. As deep water is approached, χ can reach a value of 2, indicating that the magnitude of the phase mismatch can increase to twice

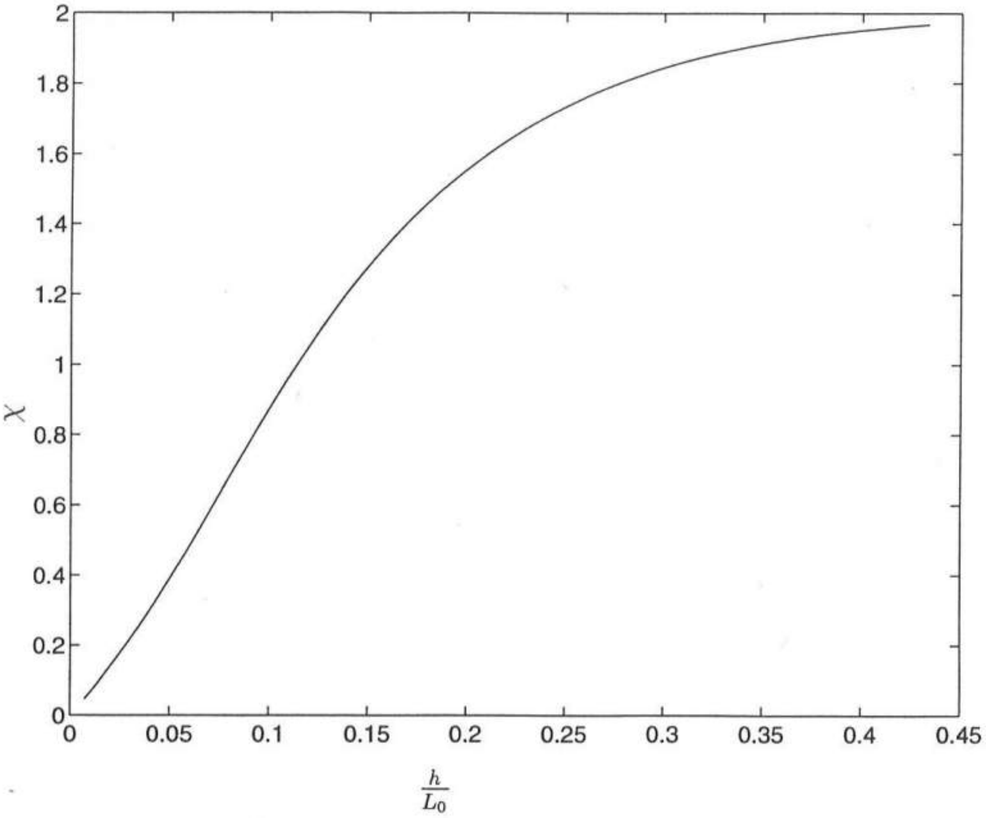

Figure 2.1: Relative Magnitude of Phase Mismatch $k_2 - 2k_1$

the magnitude of the wave number of the first component ω_1. It is clear that the assumption of slow variation of A_n would not be valid in deep water since the phase mismatch can oscillate as fast as the wave itself.

Chen and Liu (1993), in comparing their extended Boussinesq frequency domain model to the deep water case of Whalin (1971), indicate that the size of the mismatch would preclude modeling both the free and bound second harmonic. They eliminated consideration of the free second harmonic and reduced the equation for the second harmonic to evolve only the bound component for this case. Madsen and Sørensen (1992), on the other hand, made no such restriction to their time-domain extended Boussinesq model when modeling the same experimental case. However, Madsen and Sørensen's model is not subject to possible violations of the slowly varying assumption because of the time-domain formulation; they do not exclusively retain only resonant interactions. In contrast, Chen and Liu's model *is* vulnerable to large values of phase mismatch in deep water. The frequency-domain model of this chapter, and indeed of the next as well, share the same difficulties with large phase mismatches as the model of Chen and Liu (1993).

2.8 Summary

In this chapter we derived a frequency domain parabolic nonlinear mild-slope equation model. We started from the boundary value problem for water waves, truncated to $O(\epsilon^2)$ in wave slope, where properties associated with the wave motion are $O(\epsilon)$. We used the methodology of Smith and Sprinks (1975) to develop a time-dependent mild-slope equation for ϕ modified by nonlinear coupling between components of the wave field, the exact nature of which have not yet been specified. The linear dispersion relation associated with this model is the dispersion relation from linear theory, thus insuring validity of the linear portions of the equations in arbitrary water depth. We discussed some of the details of resonant triad interaction, and applied them to the model to reduce the nonlinear summations and completely factor out the time dependence. We then assumed that the solution for the Fourier transform of ϕ is expressible as a slowly varying amplitude and a fast varying phase. We thus develop evolution equations (both two-dimensional parabolic and one-dimensional) for this slowly varying amplitude. We showed that the resulting one-dimensional model is equivalent to the model of Agnon et al. (1993), with the interaction coefficients being exactly equal between the two models. We finished the chapter with a discussion of the consequences of using resonant triad interactions, especially with regards to deep water propagation problems. In Chapter 4 we will compare the parabolic nonlinear mild-slope equation model to experimental data and to other models.

Chapter 3

FULLY NONLINEAR EXTENDED BOUSSINESQ EQUATION

3.1 Introduction

Most shallow water propagation problems can be adequately described by the standard Boussinesq equations of Peregrine (1967) or related variants. However, the lack of validity of these equations in deeper water has a marked effect on the accuracy of the prediction of even the linear properties of wave propagation. Unlike the approach of the previous chapter, the Boussinesq format has the advantage of having a convenient time-domain form; thus it would be helpful to be able to include more dispersion in these Boussinesq-type equations. There are several precedents in the literature. Witting (1984) developed a one-dimensional Boussinesq-type equation from the exact, fully nonlinear depth-integrated equations for incompressible, inviscid flow. He then used a Taylor series expansion on the velocity variables about the bottom, and selected the coefficients of this expansion such that the resulting dispersion relation (which was in rational polynomial form) best matched that of full linear theory for a wide range of water depths. However, his approach would not be straightforward to generalize for two horizontal dimensions. McCowan and Blackman (1989) used a slightly different approach, and limited the integrated range of the depth to a certain "effective depth." This "effective depth" was then chosen to "best-fit" linear theory. Unfortunately, this approach would not apply to irregular waves. Madsen, et al. (1991) introduced additional terms in the momentum equation to recapture the excellent dispersion characteristics of the rational polynomial form of Witting (1984). Nwogu (1993), using the inviscid Euler equations, developed a set of extended Boussinesq equations by choosing an arbitrary depth z_α where the velocity variables are taken. The resulting dispersion relation (which resembled that of Witting 1984) was then expressed in terms of this arbitrary depth, and thus "best-fit" to the dispersion relation of full linear theory from deep to shallow water. Chen and Liu (1993) rederived Nwogu's equations using the velocity potential ϕ_α rather than the velocity vector, and transformed the equations into the frequency domain. They also refined the "best-fit" of the free parameter in the dispersion relation somewhat. All three studies demonstrated improved dispersion and transformation characteristics compared to those of standard Boussinesq theory. Unfortunately, the equations of both these investigations were truncated such that dispersive effects in the nonlinear terms were omitted. Kirby and Wei (1994) determined that this truncation affected, for example, the accuracy of the energy transfer from a primary wave to its subharmonics and superharmonics in deep water. Madsen and Sørensen (1993) and Nwogu (1994) derived transfer functions based on their respective equations that dictated this energy transfer, and compared them to those predicted by second-order Stokes theory (Dean and Sharma 1981). They found good agreement in intermediate water depth, but differences as high as 50% in deeper water. Kirby and Wei (1994), as an extension of Nwogu (1993), derived a fully nonlinear extended Boussinesq equation, and derived transfer coefficients that essentially matched those of Dean and Sharma (1981), save for differences in the calculation of the wavenumber between linear theory and this approximate theory. It is this model that we wish to treat in the frequency domain.

3.2 Derivation of a Fully-Nonlinear, Extended Boussinesq Equation

This section highlights the derivation of the fully nonlinear extended Boussinesq equation of Kirby and Wei (1994). Only the primary features of the derivation will be explained, as it in itself is not the main goal of this chapter. Details can be found in Kirby and Wei (1994).

We begin from the non-dimensionalized boundary value problem, scaled for shallow water:

$$\mu^2\nabla^2\phi + \phi_{zz} = 0; \qquad -h < z \leq \delta\eta \tag{3.1}$$

$$\phi_z = \mu^2(\eta_t + \delta\nabla\phi\cdot\nabla\eta); \qquad z = \delta\eta \tag{3.2}$$

$$\phi_z = -\mu^2\nabla\phi\cdot\nabla h; \qquad z = -h \tag{3.3}$$

$$\phi_t + \eta + \frac{\delta}{2}\left[(\nabla\phi)^2 + \frac{1}{\mu^2}(\phi_z)^2\right] = 0; \qquad z = \delta\eta \tag{3.4}$$

where δ and μ were defined in Equations (1.2) and (1.3), respectively. Integrating the Laplace equation (3.1) in the vertical coordinate z yields the continuity equation:

$$\eta_t + \nabla\cdot\int_{-h}^{\delta\eta}\nabla\phi dz = 0 \tag{3.5}$$

where the bottom boundary condition (3.3) and the kinematic free surface boundary condition (3.2) are used to eliminate boundary terms generated by the Leibnitz differentiation. We will derive our momentum equation from the dynamic free surface boundary condition (3.4). We use the relation of Chen and Liu (1993) to relate the surface potential ϕ to the velocity potential at an arbitrary depth z_α:

$$\phi = \phi_\alpha + \mu^2(z_\alpha - z)\nabla\cdot(h\nabla\phi_\alpha) + \frac{1}{2}\mu^2(z_\alpha^2 - z^2)\nabla^2\phi_\alpha + O(\mu^4) \tag{3.6}$$

Substituting (3.6) into (3.5) and integrating yields:

$$\eta_t + \nabla\cdot[(h+\delta\eta)\nabla\phi_\alpha] + \mu^2\nabla\cdot\{(h+\delta\eta)\nabla[z_\alpha\nabla\cdot(h\nabla\phi_\alpha)]\}$$

$$+(h+\delta\eta)\nabla\left(\frac{z_\alpha^2}{2}\nabla^2\phi_\alpha\right)+\mu^2\nabla\cdot\left\{\frac{1}{2}[h^2-(\delta\eta)^2]\nabla[\nabla\cdot(h\nabla\phi_\alpha)]\right\}$$
$$-\mu^2\nabla\cdot\left\{\frac{1}{6}[h^3+(\delta\eta)^3]\nabla(\nabla^2\phi_\alpha)\right\}=O(\mu^4) \qquad (3.7)$$

and substituting (3.6) into (3.4) yields:

$$\begin{aligned}\phi_{\alpha t}+\eta+\mu^2\left\{(z_\alpha-\delta\eta)\nabla\cdot(h\nabla\phi_{\alpha t})+\frac{1}{2}[z_\alpha^2-(\delta\eta)^2]\nabla^2\phi_{\alpha t}\right\}\\ +\frac{\delta}{2}(\nabla\phi_\alpha)^2+\delta\mu^2\left\{\nabla\phi_\alpha\cdot[\nabla z_\alpha\nabla\cdot(h\nabla\phi_\alpha)]+\right.\\ (z_\alpha-\delta\eta)(\nabla\phi_\alpha\cdot\nabla)[\nabla\cdot(h\nabla\phi_\alpha)]+\nabla\phi_\alpha\cdot(z_\alpha\nabla z_\alpha\nabla^2\phi_\alpha)\\ \left.+\frac{1}{2}\nabla\phi_\alpha\cdot[z_\alpha^2-(\delta\eta)^2]\nabla(\nabla^2\phi_\alpha)+\frac{1}{2}[\nabla\cdot(h\nabla\phi_\alpha)+(\delta\eta)\nabla^2\phi_\alpha]^2\right\}=O(\mu^4) \qquad (3.8)\end{aligned}$$

We note here that truncation of (3.7) and (3.8) to $O(\delta,\mu^2)$ recovers the equations of Chen and Liu (1993). Further, substitution of $\mathbf{u}_\alpha=(\nabla\phi)_\alpha$ into (3.7) and (3.8) and truncation to $O(\delta,\mu^2)$ recovers the equations of Nwogu (1993).

3.3 Linear Dispersion

The properties of the dispersion relation of equations similar to (3.7) and (3.8) have been discussed by Nwogu (1993) and Chen and Liu (1993). The most straightforward way to derive the dispersion relation from this system is to linearize the one-dimensional versions of the equations and then assume wave-like forms for the dependent variables η and ϕ_α, as follows:

$$\eta=ae^{i(kx-\omega t)} \qquad (3.9)$$

$$\phi_\alpha=be^{i(kx-\omega t)} \qquad (3.10)$$

These are then substituted into (3.7) and (3.8), and the determinant allowed to vanish to ensure non-trivial solutions of the system. The resulting dispersion relation is:

$$C^2 = gh\left[\frac{1-(\alpha+\frac{1}{3})(kh)^2}{1-\alpha(kh)^2}\right] \tag{3.11}$$

where C is the wave celerity and:

$$\alpha = \frac{z_\alpha^2}{2h^2}+\frac{z_\alpha}{h} \tag{3.12}$$

An explicit expression for the wave number k is found by:

$$k = \sqrt{\frac{g+\alpha\omega^2 h-\sqrt{(g+\alpha\omega^2 h)^2-4g\left(\alpha+\frac{1}{3}\right)\omega^2 h}}{2gh^2\left(\alpha+\frac{1}{3}\right)}} \tag{3.13}$$

The group velocity C_g is found by:

$$C_g = \frac{\partial\omega}{\partial k} = C\left\{1-\frac{(kh)^2/3}{[1-\alpha(kh)^2][1-(\alpha+\frac{1}{3})(kh)^2]}\right\} \tag{3.14}$$

The one-dimensional equation of Witting (1984) was found to have (3.11) as its dispersion relation as well. Using Pade approximants to match (3.11) to the linear dispersion relation, Witting found the optimum α to be $\alpha = -\frac{2}{5}$. Nwogu (1993), using a least squares numerical technique, refined the estimate of an optimum α to be -0.390. However, this least squares technique was performed on the dispersion relation only. Chen and Liu (1993) used a least squares technique on both the linear dispersion relation (3.11) and the group velocity expression (3.14) from deep to shallow water. This resulted in a slightly different value of α, $\alpha = -0.3855$, corresponding to a value of $z_\alpha = -0.522h$. Figure 3.1 shows the ratio of $\frac{C}{C_L}$ and $\frac{C_g}{C_{gL}}$ (where C_L is the wave celerity and C_{gL} is the group velocity from linear theory) against $\frac{h}{L_0}$ (where L_0 is the linear wavelength in deep water), for various values of α. The deep water limit is reached when $\frac{h}{L_0} = 0.5$, while shallow water is reached when $\frac{h}{L_0} = 0.02$. It is apparent that the best results (where the ratios $\frac{C}{C_L}$ and $\frac{C_g}{C_{gL}}$ are closest to one) are obtained for the widest range of water depths if $\alpha = -0.3855$, while the poorest results are obtained when $\alpha = -\frac{1}{3}$, which corresponds to the dispersion relation of standard Boussinesq theory. Nwogu's (1993) value of $\alpha = -0.390$ and Witting's (1984) value of $\alpha = -\frac{2}{5}$ work well, but do not match linear theory as well as Chen and Liu's (1993) value of $\alpha = -0.3855$. Thus we use Chen and Liu's value of $\alpha = -0.3855$ in this study.

3.4 Frequency Domain Transformation

Equations (3.7) and (3.8) represent an extension of previous work done in this vein, since the nonlinearity is no longer assumed small. These equations can be modeled (with some effort) in the time domain. However, we are concerned here with the frequency domain and the retention of triad interactions; thus, we must truncate (3.7) and (3.8) to eliminate cubic ($O(\delta^2)$) and quartic ($O(\delta^3)$) nonlinearities, since these cannot be treated in this manner. These truncated equations are (in dimensional form):

$$\begin{aligned}\eta_t + \nabla \cdot [(h+\eta)\nabla\phi_\alpha] + \nabla \cdot \{(h+\eta)\nabla[z_\alpha \nabla \cdot (h\nabla\phi_\alpha)]\} \\ +(h+\eta)\nabla\left(\frac{z_\alpha^2}{2}\nabla^2\phi_\alpha\right) + \nabla \cdot \left\{\frac{1}{2}h^2\nabla[\nabla \cdot (h\nabla\phi_\alpha)]\right\} \\ -\nabla \cdot \left[\frac{1}{6}h^3\nabla(\nabla^2\phi_\alpha)\right] = O(\delta^2\mu^2, \delta^3\mu^2, \mu^4)\end{aligned} \tag{3.15}$$

$$\begin{aligned}\phi_{\alpha t} + g\eta + (z_\alpha - \eta)\nabla \cdot (h\nabla\phi_{\alpha t}) + \frac{1}{2}z_\alpha^2\nabla^2\phi_{\alpha t} \\ +\frac{1}{2}(\nabla\phi_\alpha)^2 + \nabla\phi_\alpha \cdot [\nabla z_\alpha \nabla \cdot (h\nabla\phi_\alpha)] + \\ \nabla\phi_\alpha \cdot z_\alpha\nabla[\nabla \cdot (h\nabla\phi_\alpha)] + \nabla\phi_\alpha \cdot (z_\alpha\nabla z_\alpha\nabla^2\phi_\alpha) \\ +\frac{1}{2}\nabla\phi_\alpha \cdot z_\alpha^2\nabla(\nabla^2\phi_\alpha) + \frac{1}{2}[\nabla \cdot (h\nabla\phi_\alpha)]^2 = O(\delta^2\mu^2, \delta^3\mu^2, \mu^4)\end{aligned} \tag{3.16}$$

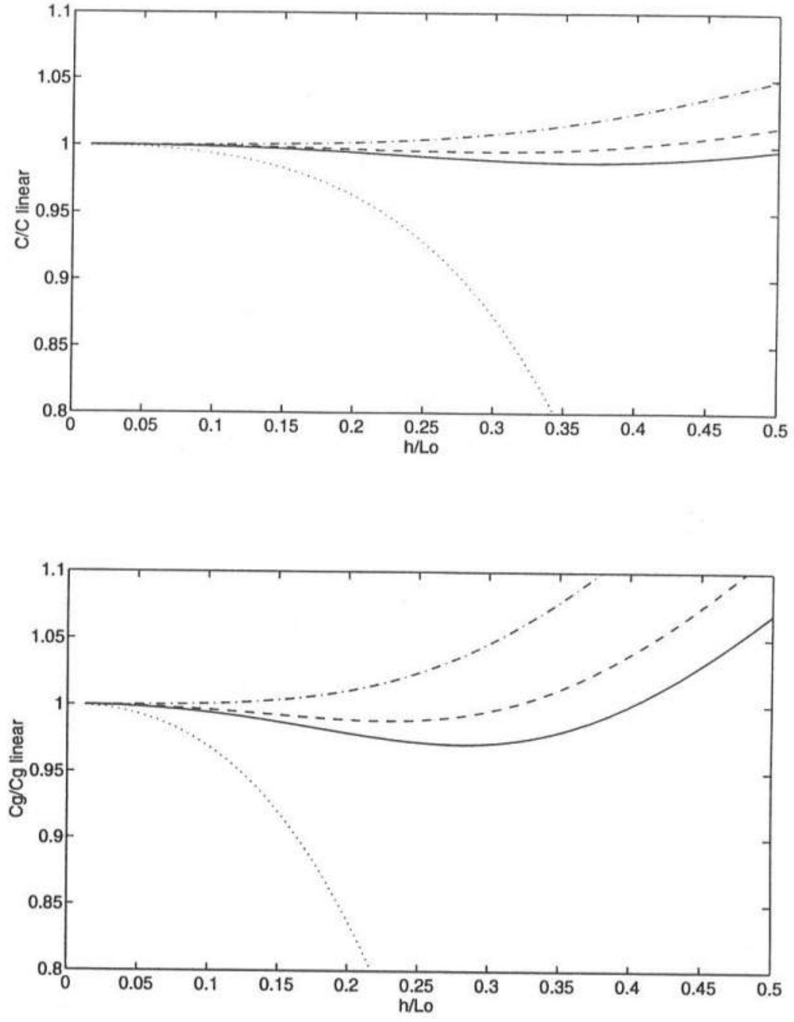

Figure 3.1: Comparison of Wave Celerities and Group Velocities to Those of Linear Theory for Several Values of α: $\alpha = -0.3855$ (—); $\alpha = -0.390$ (- - -); $\alpha = -1/3$ (. . .); $\alpha = -2/5$ (- . -). (Top) Normalized Wave Celerity; (Bottom) Normalized Group Velocity.

The first step in frequency-domain transformation is the assumption of periodicity in time:

$$\eta = \sum_{n=1}^{\infty} \frac{\hat{\eta}_n}{2} e^{-in\omega t} + \frac{\hat{\eta}_n^*}{2} e^{in\omega t} \tag{3.17}$$

$$\phi_\alpha = \sum_{n=1}^{\infty} \frac{\hat{\phi}_{\alpha n}}{2} e^{-in\omega t} + \frac{\hat{\phi}_{\alpha n}^*}{2} e^{in\omega t} \tag{3.18}$$

Substitution of this into (3.15) and (3.16) and making use of resonant interactions between a triad of components (as we did in the previous chapter) yields a transformed continuity equation:

$$\begin{aligned}
& -in\omega\hat{\eta}_n + \nabla\cdot(h\nabla\hat{\phi}_{\alpha n}) + \nabla\cdot[h\nabla(z_\alpha\nabla h\cdot\nabla\hat{\phi}_{\alpha n} + \alpha h^2\nabla^2\hat{\phi}_{\alpha n})] \\
+ & \ \nabla\cdot\left\{\frac{h^2}{2}\nabla[\nabla\cdot(h\nabla\hat{\phi}_{\alpha n})]\right\} - \nabla\cdot\left[\frac{h^3}{6}\nabla(\nabla^2\hat{\phi}_{\alpha n})\right] \\
+ & \ \frac{1}{4}\nabla\cdot\left(\sum_{l=1}^{n-1}\hat{\eta}_l\nabla\hat{\phi}_{\alpha n-l} + \hat{\eta}_{n-l}\nabla\hat{\phi}_{\alpha l} + 2\sum_{l=1}^{N-n}\hat{\eta}_l^*\nabla\hat{\phi}_{\alpha n+l} + \hat{\eta}_{n+l}\nabla\hat{\phi}_{\alpha l}^*\right) \\
+ & \ \frac{\alpha h^2}{4}\nabla\cdot\Bigg[\sum_{l=1}^{n-1}\hat{\eta}_l\nabla(\nabla^2\hat{\phi}_{\alpha n-l}) + \hat{\eta}_{n-l}\nabla(\nabla^2\hat{\phi}_{\alpha l}) \\
+ & \ 2\sum_{l=1}^{N-n}\hat{\eta}_l^*\nabla(\nabla^2\hat{\phi}_{\alpha n+l}) + \hat{\eta}_{n+l}\nabla(\nabla^2\hat{\phi}_{\alpha l}^*)\Bigg] = 0
\end{aligned} \tag{3.19}$$

and a transformed momentum equation:

$$\begin{aligned}
& -in\omega\hat{\phi}_{\alpha n} + g\hat{\eta}_n - in\omega z_\alpha\nabla h\cdot\nabla\hat{\phi}_{\alpha n} - in\omega\alpha h^2\nabla^2\hat{\phi}_{\alpha n} + \frac{1}{4}\Bigg(\sum_{l=1}^{n-1}\nabla\hat{\phi}_{\alpha l}\cdot\nabla\hat{\phi}_{\alpha n-l} \\
+ & \ 2\sum_{l=1}^{N-n}\nabla\hat{\phi}_{\alpha l}^*\cdot\nabla\hat{\phi}_{\alpha n+l}\Bigg) + \frac{i\omega h}{4}\Bigg[\sum_{l=1}^{n-1}(n-l)\hat{\eta}_l\nabla^2\hat{\phi}_{\alpha n-l} + l\hat{\eta}_{n-l}\nabla^2\hat{\phi}_{\alpha l} \\
+ & \ 2\sum_{l=1}^{N-n}(n+l)\hat{\eta}_l^*\nabla^2\hat{\phi}_{\alpha n+l} - l\hat{\eta}_{n+l}\nabla^2\hat{\phi}_{\alpha l}^*\Bigg] + \frac{\alpha h^2}{4}\Bigg[\sum_{l=1}^{n-1}\nabla\hat{\phi}_{\alpha l}\cdot\nabla(\nabla^2\hat{\phi}_{\alpha n-l}) \\
+ & \ \nabla\hat{\phi}_{\alpha n-l}\cdot\nabla(\nabla^2\hat{\phi}_{\alpha l}) + 2\sum_{l=1}^{N-n}\nabla\hat{\phi}_{\alpha l}^*\cdot\nabla(\nabla^2\hat{\phi}_{\alpha n+l}) + \nabla\hat{\phi}_{\alpha n+l}\cdot\nabla(\nabla^2\hat{\phi}_{\alpha l}^*)\Bigg] \\
+ & \ \frac{h^2}{4}\left(\sum_{l=1}^{n-1}\nabla^2\hat{\phi}_{\alpha l}\nabla^2\hat{\phi}_{\alpha n-l} + 2\sum_{l=1}^{N-n}\nabla^2\hat{\phi}_{\alpha l}^*\nabla^2\hat{\phi}_{\alpha n-l}\right) = 0
\end{aligned} \tag{3.20}$$

The next step involves combining (3.19) and (3.20) into a single equation for a single variable. This must be done in such as way as to maintain the dispersion relation (3.11). Here, we use a first order relationship between $\hat{\phi}_{\alpha n}$ and $\hat{\eta}_n$ from the transformed continuity equation (3.19) to eliminate $\hat{\eta}_n$ from the nonlinear terms of (3.20):

$$\hat{\eta}_n = -\frac{ih}{n\omega}\nabla^2\hat{\phi}_{\alpha n} \tag{3.21}$$

where we have assumed that the bottom slope is small compared to the gradient of $\hat{\phi}_{\alpha n}$. Then, we rearrange the momentum equation (3.20) to isolate $\hat{\eta}_n$, and substitute this into the continuity equation (3.19), always keeping track of the order of the various terms to insure consistency with the order of truncation. After rearranging the linear terms somewhat, the following time-periodic equation for $\hat{\phi}_{\alpha n}$ results:

$$\begin{aligned}
& \frac{n^2\omega^2}{g}\hat{\phi}_{\alpha n} + \left(1+\frac{n^2\omega^2 z_\alpha}{g}\right)\nabla h\cdot\nabla\hat{\phi}_{\alpha n} + \left(h+\frac{n^2\omega^2h^2\alpha}{g}\right)\nabla^2\hat{\phi}_{\alpha n} \\
+ \;& \left(1+5\alpha+\sqrt{1+2\alpha}\right)h^2\nabla h\cdot\nabla(\nabla^2\hat{\phi}_{\alpha n}) + \left(\alpha+\frac{1}{3}\right)h^3\nabla^2\nabla^2\hat{\phi}_{\alpha n} \\
+ \;& \frac{in\omega}{4g}\left(\sum_{l=1}^{n-1}\nabla\hat{\phi}_{\alpha l}\cdot\nabla\hat{\phi}_{\alpha n-l} + 2\sum_{l=1}^{N-n}\nabla\hat{\phi}^*_{\alpha l}\cdot\nabla\hat{\phi}_{\alpha n+l}\right) \\
+ \;& \frac{in\omega\alpha h^2}{4g}\Biggl[\sum_{l=1}^{n-1}\nabla\hat{\phi}_{\alpha l}\cdot\nabla(\nabla^2\hat{\phi}_{\alpha n-l}) + \nabla\hat{\phi}_{\alpha n-l}\cdot\nabla(\nabla^2\hat{\phi}_{\alpha l}) \\
+ \;& 2\sum_{l=1}^{N-n}\nabla\hat{\phi}^*_{\alpha l}\cdot\nabla(\nabla^2\hat{\phi}_{\alpha n+l}) + \nabla\hat{\phi}_{\alpha n+l}\cdot\nabla(\nabla^2\hat{\phi}^*_{\alpha l})\Biggr] \\
+ \;& \frac{in\omega h^2}{4g}\left(\sum_{l=1}^{n-1}\tau_{n,l}\nabla^2\hat{\phi}_{\alpha l}\nabla^2\hat{\phi}_{\alpha n-l} - 2\sum_{l=1}^{N-n}\zeta_{n,l}\nabla^2\hat{\phi}^*_{\alpha l}\nabla^2\hat{\phi}_{\alpha n+l}\right) \\
+ \;& \frac{i\omega}{4g}\nabla\cdot\Biggl[\sum_{l=1}^{n-1}l(\hat{\phi}_{\alpha l}+\alpha h^2\nabla^2\hat{\phi}_{\alpha l})\nabla\hat{\phi}_{\alpha n-l} + (n-l)(\hat{\phi}_{\alpha n-l}+\alpha h^2\nabla^2\hat{\phi}_{\alpha n-l})\nabla\hat{\phi}_{\alpha l} \\
+ \;& 2\sum_{l=1}^{N-n}(n+l)(\hat{\phi}_{\alpha n+l}+\alpha h^2\nabla^2\hat{\phi}_{\alpha n+l})\nabla\hat{\phi}^*_{\alpha l} - l(\hat{\phi}^*_{\alpha l}+\alpha h^2\nabla^2\hat{\phi}^*_{\alpha l})\nabla\hat{\phi}_{\alpha n+l}\Biggr] \\
+ \;& \frac{i\omega\alpha h^2}{4g}\nabla\cdot\Biggl[\sum_{l=1}^{n-1}l\hat{\phi}_{\alpha l}\nabla(\nabla^2\hat{\phi}_{\alpha n-l}) + (n-l)\hat{\phi}_{\alpha n-l}\nabla(\nabla^2\hat{\phi}_{\alpha l})
\end{aligned}$$

$$+ \quad 2\sum_{l=1}^{N-n}(n+l)\hat{\phi}_{\alpha n+l}\nabla(\nabla^2\hat{\phi}^*_{\alpha l}) - l\hat{\phi}^*_{\alpha l}\nabla(\nabla^2\hat{\phi}_{\alpha n+l})\Big] = 0 \tag{3.22}$$

where:

$$\tau_{n,l} = \frac{(n-l)^2 + l(n-l) + l^2}{l(n-l)} \tag{3.23}$$

$$\zeta_{n,l} = \frac{(n+l)^2 - l(n+l) + l^2}{l(n+l)} \tag{3.24}$$

Equation (3.22) governs the potential $\hat{\phi}_{\alpha n}$. We use (3.20) to determine the transformed free surface elevation η_n.

3.5 Parabolic Approximation

As in the previous chapter, we wish to create a parabolic model which will evolve the amplitudes of the wave field (in this case, the amplitudes of $\hat{\phi}_{\alpha n}$) throughout the domain. Thus we assume a propagating wave form for $\hat{\phi}_{\alpha n}$ and $\hat{\eta}_n$ in terms of an amplitude that varies slowly in space and a fast varying phase:

$$\hat{\phi}_{\alpha n} = B_n(x,y)e^{i\int k(x,y)dx} \tag{3.25}$$

$$\hat{\eta}_n = A_n(x,y)e^{i\int k(x,y)dx} \tag{3.26}$$

Rather than explicitly invoking the parabolic approximation, we substitute (3.25) into (3.20) and neglect B_{nxx} that arise. This results in the following evolution equation for the amplitudes of the velocity potential $\hat{\phi}_{\alpha n}$:

$$\left[h + \frac{n^2\omega^2h^2\alpha}{g} - 2\left(\alpha + \frac{1}{3}\right)h^3k_n^2\right]\left(B_n e^{i\int k_n dx}\right)_{yy} e^{-i\int k_n dx}$$
$$+ \quad 2i\left[k_n\left(h + \frac{n^2\omega^2h^2\alpha}{g}\right) - 2k_n^3h^3\left(\alpha + \frac{1}{3}\right)\right]B_{nx}$$

$$\begin{aligned}
&+ \left[1 + \frac{n^2\omega^2 z_\alpha}{g} - (1 + 5\alpha + \sqrt{1+2\alpha})k_n^2 h^2\right] h_y \left(B_n e^{i\int k_n dx}\right)_y e^{-i\int k_n dx} \\
&+ i\left\{k_n\left(1 + \frac{n^2\omega^2 z_\alpha}{g}\right) - \left[k_n^3 h^2(1 + 5\alpha + \sqrt{1+2\alpha})\right]\right\} h_x B_n \\
&+ i\left[h + \frac{n^2\omega^2 h^2 \alpha}{g} - 6\left(\alpha + \frac{1}{3}\right) h^3 k_n^2\right] k_{nx} B_n \\
&- \frac{i\omega}{4g}\left(\sum_{l=1}^{n-1} \tilde{R} B_l B_{n-l} e^{i\int(k_l + k_{n-l} - k_n)dx} + 2\sum_{l=1}^{N-n} \tilde{S} B_l^* B_{n+l} e^{i\int(k_{n+l} - k_l - k_n)dx}\right) \\
&= 0 \qquad (3.27)
\end{aligned}$$

where:

$$\begin{aligned}
&\tilde{R} = (n-l)k_l^2 + 2nk_l k_{n-l} + lk_{n-l}^2 - nh^2\tau_{n,l}k_l^2 k_{n-l}^2 \\
&- \alpha h^2[(n-l)k_l^4 + 2nk_l^3 k_{n-l} + nk_l^2 k_{n-l}^2 + 2nk_l k_{n-l}^3 + lk_{n-l}^4] \qquad (3.28)
\end{aligned}$$

$$\begin{aligned}
&\tilde{S} = (n+l)k_l^2 - 2nk_l k_{n+l} - lk_{n+l}^2 + nh^2\zeta_{n,l}k_l^2 k_{n+l}^2 \\
&- \alpha h^2[(n+l)k_l^4 - 2nk_l^3 k_{n+l} + nk_l^2 k_{n+l}^2 - 2nk_l k_{n+l}^3 - lk_{n+l}^4] \qquad (3.29)
\end{aligned}$$

Similarly, substituting (3.25) and (3.26) into (3.22) and again neglecting the A_{nxx} terms yields the following evolution equation for the amplitudes of the free surface elevation $\hat{\eta}_n$:

$$\begin{aligned}
&A_n = \frac{in\omega}{g}\alpha h^2 \left(B_n e^{i\int k_n dx}\right)_{yy} e^{-i\int k_n dx} + \frac{in\omega z_\alpha}{g} h_y \left(B_n e^{i\int k_n dx}\right)_y e^{-i\int k_n dx} \\
&- \frac{2n\omega\alpha h^2 k_n}{g} B_{nx} - \frac{n\omega z_\alpha k_n}{g} h_x B_n - \frac{n\omega\alpha h^2}{g} k_{nx} B_n + \frac{in\omega}{g}(1 - \alpha k_n^2 h^2) B_n \\
&+ \frac{1}{4g}\left(\sum_{l=1}^{n-1} \tilde{R}' B_l B_{n-l} e^{i\int(k_l + k_{n-l} - k_n)dx} - 2\sum_{l=1}^{N-n} \tilde{S}' B_l^* B_{n+l} e^{i\int(k_{n+l} - k_l - k_n)dx}\right) \\
&\qquad (3.30)
\end{aligned}$$

where:

$$\tilde{R}' = k_l k_{n-l} - \alpha h^2\left(k_l k_{n-l}^3 + k_l^3 k_{n-l}\right) - h^2\tau_{n,l}k_l^2 k_{n-l}^2 \qquad (3.31)$$

$$\tilde{S}' = k_l k_{n+l} - \alpha h^2 \left(k_l k_{n+l}^3 + k_l^3 k_{n+l} \right) - h^2 \zeta_{n,l} k_l^2 k_{n+l}^2 \tag{3.32}$$

As we did in the previous chapter, we must employ a reference phase function to isolate the y-dependence of the wavenumber. We again use the y-averaged wavenumber $\overline{k}_{n0}(x)$ in our reference phase function (Lozano and Liu, 1980). The amplitudes for the velocity potential and the free surface are redefined as b_n and a_n respectively, and are related to the original amplitudes B_n and A_n by:

$$B_n(x,y) = b_n(x,y) e^{i(\int \overline{k}(x)_{n0} dx - \int k_n(x,y) dx)} \tag{3.33}$$

$$A_n(x,y) = a_n(x,y) e^{i(\int \overline{k}(x)_{n0} dx - \int k_n(x,y) dx)} \tag{3.34}$$

Substituting (3.33) into (3.29) yields:

$$\begin{aligned}
& \left[h + \frac{n^2\omega^2 h^2 \alpha}{g} - 2\left(\alpha + \frac{1}{3}\right) h^3 k_n^2 \right] b_{nyy} + 2i \left[k_n \left(h + \frac{n^2\omega^2 h^2 \alpha}{g} \right) \right. \\
- & \left. 2k_n^3 h^3 \left(\alpha + \frac{1}{3}\right) \right] b_{nx} + \left[1 + \frac{n^2\omega^2 z_\alpha}{g} - (1 + 5\alpha + \sqrt{1+2\alpha}) k_n^2 h^2 \right] h_y b_{ny} \\
+ & \; i \left\{ k_n \left(1 + \frac{n^2\omega^2 z_\alpha}{g} \right) - \left[k_n^3 h^2 (1 + 5\alpha + \sqrt{1+2\alpha}) \right] \right\} h_x b_n \\
- & \; 2 \left[k_n \left(h + \frac{n^2\omega^2 h^2 \alpha}{g} \right) - 2k_n^3 h^3 \left(\alpha + \frac{1}{3}\right) \right] (\overline{k}_{n0} - k_n) b_n \\
+ & \; i \left[h + \frac{n^2\omega^2 h^2 \alpha}{g} - 6\left(\alpha + \frac{1}{3}\right) h^3 k_n^2 \right] k_{nx} b_n \\
- & \; \frac{i\omega}{4g} \left(\sum_{l=1}^{n-1} \tilde{R} b_l b_{n-l} e^{i\int(\overline{k}_{l0} + \overline{k}_{n-l0} - \overline{k}_{n0})dx} + 2 \sum_{l=1}^{N-n} \tilde{S} b_l^* b_{n+l} e^{i\int(\overline{k}_{n+l0} - \overline{k}_{l0} - \overline{k}_{n0})dx} \right) \\
= & \; 0
\end{aligned} \tag{3.35}$$

while substituting (3.33) and (3.34) into (3.30) gives:

$$\begin{aligned}
a_n = & \frac{in\omega}{g} \alpha h^2 b_{nyy} + \frac{in\omega z_\alpha}{g} h_y b_{ny} - \frac{2n\omega\alpha h^2 k_n}{g} b_{nx} - \frac{n\omega z_\alpha k_n}{g} h_x b_n \\
- & \frac{n\omega\alpha h^2}{g} k_{nx} b_n + \frac{in\omega}{g} [1 - \alpha k_n^2 h^2 - 2\alpha h^2 k_n (\overline{k}_{n0} - k_n)] b_n
\end{aligned}$$

$$+ \quad \frac{1}{4g}\left(\sum_{l=1}^{n-1}\tilde{R}'b_l b_{n-l}e^{i\int(\overline{k}_{l0}+\overline{k}_{n-l0}-\overline{k}_{n0})dx} + 2\sum_{l=1}^{N-n}\tilde{S}'b_l^* b_{n+l}e^{i\int(\overline{k}_{n+l0}-\overline{k}_{l0}-\overline{k}_{n0})dx}\right) \tag{3.36}$$

Equations (3.35) and (3.36) are the parabolic evolution equations used to model the fully nonlinear extended Boussinesq equations of Kirby and Wei (1994). They are an extension of Chen and Liu (1993) due to the retention of $O(\delta\mu^2)$ terms. The linear terms are identical to those of Chen and Liu (1993), save for a difference in the definition of the reference phase function. For later reference, we write the one-dimensional version of (3.35):

$$\begin{aligned} & 2k_n h\left[1+\frac{n^2\omega^2 h\alpha}{g}-2k_n^2h^2\left(\alpha+\frac{1}{3}\right)\right]B_{nx} \\ + \quad & k_n\left[1+\frac{n^2\omega^2 z_\alpha}{g}-k_n^2h^2(1+5\alpha+\sqrt{1+2\alpha})\right]h_x B_n \\ + \quad & \left[h+\frac{n^2\omega^2h^2\alpha}{g}-6\left(\alpha+\frac{1}{3}\right)k_n^2h^3\right]k_{nx}B_n \\ - \quad & \frac{\omega}{4g}\left(\sum_{l=1}^{n-1}\tilde{R}B_lB_{n-l}e^{i\int(k_l+k_{n-l}-k_n)dx}+2\sum_{l=1}^{N-n}\tilde{S}B_l^*B_{n+l}e^{i\int(k_{n+l}-k_l-k_n)dx}\right)=0 \end{aligned} \tag{3.37}$$

and the one-dimensional version of (3.36):

$$\begin{aligned} & A_n=\frac{n\omega}{g}\left[i(1-\alpha k_n^2h^2)B_n-2k_nh^2\alpha B_{nx}-h^2\alpha k_{nx}B_n-z_\alpha k_n h_x B_n\right] \\ + \quad & \frac{1}{4g}\left(\sum_{l=1}^{n-1}\tilde{R}'B_lB_{n-l}e^{i\int(k_l+k_{n-l}-k_n)dx}-2\sum_{l=1}^{N-n}\tilde{S}'B_l^*B_{n+l}e^{i\int(k_{n+l}-k_l-k_n)dx}\right) \end{aligned} \tag{3.38}$$

where, again, we revert back to the original B_n and A_n since there is no difference between the actual and reference wavenumbers in one-dimensional wave propagation. As with the model of the last chapter, we use the Crank-Nicholson scheme for the parabolic equation set (3.35) and (3.36), and a step-size adaptive fourth-order Runge-Kutta method (Press, et al. 1986) for the one-dimensional shoaling equations (3.37) and (3.38).

We wish to emphasize here that frequency-domain transformation of the fully nonlinear extended Boussinesq equations in effect creates a different model, with properties that do not *necessarily* match those of the time-domain model from which it was derived. Indeed, as we will see in the next section, there are myriad ways to perform the combination and transformation of these equations to gain the frequency domain formulation. Each method has its own advantages and disadvantages, and care must be taken in inferring the behavior of the time-domain model based on the behavior of the frequency-domain model. With this *caveat* in mind, we note here that references to the "fully nonlinear extended Boussinesq equation" in later sections of this work apply to the frequency-domain form (Equations 3.35 and 3.36 for the parabolic model, and Equations 3.37 and 3.38 for the one dimensional shoaling model), unless explicit reference is made to the formulation in the time domain.

3.6 Linear Shoaling

We have seen that the dispersion relation (3.11) compares well to that of linear theory from deep to shallow water. This is no assurance, however, that the shoaling characteristics would compare equally well to shoaling from linear theory. In this section we will look at how well the linearized version of (3.37) and (3.38) compare to the linearized version of the fully dispersive nonlinear shoaling model (Equation 2.58). We will also examine other linear shoaling models derived from the fully nonlinear extended Boussinesq equations.

3.6.1 Shoaling Models Derived from the $(\eta, \mathbf{u}_\alpha)$ Form of the Fully Nonlinear Extended Boussinesq Equations

One reason that the fully nonlinear extended Boussinesq equations were derived in terms of the velocity potential ϕ_α instead of the velocity vector $\mathbf{u}_\alpha$ is that the resulting equations (3.7) and (3.8) are simpler to treat in the frequency domain. Transforming these equations involves unfolding every derivative of the vector differential operators in (3.7) and (3.8), a task made much more tedious if the gradient of the equations had to be taken to make the substitution $\mathbf{u}_\alpha = (\nabla\phi)_\alpha$. Indeed, Chen and Liu (1993) maintain that it is not possible to reduce the $(\eta, \mathbf{u}_\alpha)$ to one in terms of η and still maintain the linear dispersion relation (3.11). This is not true; it *is* possible, but doing so involves first-order substitutions between η and $\mathbf{u}_\alpha$ that are ambiguous. We shall see, however, that by using a free parameter to circumvent the ambiguities in the linear terms, we will obtain an excellent linear shoaling model compared to linear theory.

The first step in obtaining the $(\eta, \mathbf{u}_\alpha)$ equations from the (η, ϕ_α) equations is to take the gradient of (3.6), evaluate z at z_α, and substitute $\mathbf{u}_\alpha = (\nabla\phi)_\alpha$. This results in:

$$\nabla\phi_\alpha = \mathbf{u}_\alpha - \mu^2 \nabla z_\alpha \nabla\cdot(h\nabla\phi_\alpha) + \frac{1}{2}\mu^2(2z_\alpha\nabla z_\alpha\nabla^2\phi_\alpha) \tag{3.39}$$

We then substitute this into the continuity equation (3.7). This yields:

$$\begin{aligned} &\eta_t + \nabla\cdot[(h+\delta\eta)\mathbf{u}_\alpha] \\ +\ &\mu^2\nabla\cdot\left\{\left[(h+\delta\eta)z_\alpha + \frac{1}{2}(h^2-(\delta\eta)^2)\right]\nabla[\nabla\cdot(h\mathbf{u}_\alpha)]\right\} \\ +\ &\mu^2\nabla\cdot\left\{\left[(h+\delta\eta)\frac{z_\alpha^2}{2} - \frac{1}{6}(h^3+(\delta\eta)^3)\right]\nabla(\nabla\cdot\mathbf{u}_\alpha)\right\} = 0 \end{aligned} \tag{3.40}$$

Substituting (3.39) into the momentum equation (3.8) and taking the gradient results in:

$$\mathbf{u}_{\alpha t} + \nabla\eta + \delta(\mathbf{u}_\alpha\cdot\nabla)\mathbf{u}_\alpha$$

$$
\begin{aligned}
&+\quad \mu^2\left\{\frac{1}{2}z_\alpha^2\nabla(\nabla\cdot\mathbf{u}_{\alpha t})+z_\alpha\nabla[\nabla\cdot(h\mathbf{u}_\alpha)]-\nabla\left[\frac{1}{2}(\delta\eta)^2\nabla\cdot\mathbf{u}_{\alpha t}+\delta\eta\nabla\cdot(h\mathbf{u}_{\alpha t})\right]\right\}\\
&+\quad \delta\mu^2\nabla\left\{(z_\alpha-\delta\eta)(\mathbf{u}_\alpha\cdot\nabla)[\nabla\cdot(h\mathbf{u}_{\alpha t})]\right.\\
&+\quad \left.\frac{1}{2}[z_\alpha^2-(\delta\eta)^2](\mathbf{u}_\alpha\cdot\nabla)(\nabla\cdot\mathbf{u}_\alpha)+\frac{1}{2}[\nabla\cdot(h\mathbf{u}_\alpha)+\delta\eta\nabla\mathbf{u}_\alpha]^2\right\}=0
\end{aligned}
\tag{3.41}
$$

These equations are modeled by Kirby and Wei (1994).

Linearizing (3.40) and (3.41) and neglecting the y-direction yields (in dimensional form):

$$\eta_t+(hu_\alpha)_x+\left[\left(\frac{z_\alpha^2}{2}-\frac{h^2}{6}\right)hu_{\alpha xx}+\left(z_\alpha+\frac{h}{2}\right)h(hu_\alpha)_{xx}\right]_x=0 \tag{3.42}$$

and:

$$u_{\alpha t}+g\eta_x+\frac{z_\alpha^2}{2}u_{\alpha txx}+z_\alpha(hu_{\alpha t})_{xx}=0 \tag{3.43}$$

We make use of the following first-order relations to eliminate u_α for η:

$$\eta_t = -(hu_\alpha)_x \tag{3.44}$$

$$\eta_{tt} = -(hu_{\alpha t})_x \tag{3.45}$$

$$u_{\alpha t} = -g\eta_x \tag{3.46}$$

We differentiate (3.42) once with respect to time, expand the derivatives (neglecting terms like h_{xx} and $(h_x)^2$), and substitute (3.46) to eliminate u_α in all but one term, resulting in:

$$\eta_{tt}+(hu_{\alpha t})_x-g\left(3\alpha+2\frac{z_\alpha}{h}+2\right)h^2h_x\eta_{xxx}-gh^3\left(\alpha+\frac{1}{3}\right)\eta_{xxxx}=0 \tag{3.47}$$

We then multiply (3.43) by h, and substitute *the x-derivative* of (3.45) into the result. This yields:

$$hu_{\alpha t}=-gh\eta_x+\alpha h^2\eta_{xtt}-gh^2\left(\frac{z_\alpha}{h}\right)^2h_x\eta_{xx} \tag{3.48}$$

The x-derivative of (3.46) is taken before substitution because earlier attempts have revealed that a relatively poor linear shoaling model results if (3.46) were substituted directly. This is an example of the ambiguous nature of the substitutions used to collapse the two equations into one for η only; (3.44), (3.45) and (3.46) can either be substituted directly into (3.42) and (3.43), or derivatives with respect to time and/or space can be taken first and then substituted. Each approach yields a different shoaling model which compares differently to shoaling from linear theory. In any case, substitution of (3.48) into (3.47) yields the linear wave equation:

$$\begin{aligned} &\eta_{tt} + gh_x\eta_x + gh\eta_{xx} + 2\alpha hh_x\eta_{xtt} + \alpha h^2\eta_{xxt} - gh^2(5\alpha+2)h_x\eta_{xxx} \\ - \;& gh^3\left(\alpha + \frac{1}{3}\right)\eta_{xxxx} = 0 \end{aligned} \tag{3.49}$$

Derivation of a shoaling model directly from (3.49) has resulted in extremely poor comparisons to shoaling from linear theory. This is probably due to incorrectly choosing the first-order substitutions required to derive the wave equation (3.49). Rather than iteratively choose different first-order substitutions, we isolate the terms proportional to hh_x:

$$2\alpha\eta_{xtt} - gh(5\alpha+2)\eta_{xxx} \tag{3.50}$$

We add a two-dimensional wave equation to (3.50):

$$\beta[\eta_{tt} - g(h\eta_{xx})]_x = 0 \tag{3.51}$$

which simply adds zero to these terms (β is a free parameter). We neglect the h_x in (3.51) since (3.50) is already proportional to it. We then obtain the following term:

$$(2\alpha+\beta)\eta_{xtt} - gh(5\alpha+2+\beta)\eta_{xxx} \tag{3.52}$$

which modifies (3.49) to:

$$\begin{aligned}\eta_{tt} + gh_x\eta_x + gh\eta_{xx} + (2\alpha+\beta)hh_x\eta_{xtt} + \alpha h^2\eta_{xxt} - gh^2(5\alpha+2+\beta)h_x\eta_{xxx} \\ - \quad gh^3\left(\alpha+\frac{1}{3}\right)\eta_{xxxx} = 0 \qquad (3.53)\end{aligned}$$

We obtain a shoaling model, and ascertain whether we have retained the dispersion relation (3.11), by substituting:

$$\eta = Ae^{i(kx-\omega t)} \qquad (3.54)$$

into (3.53) and isolating the bottom slope terms from the flat-bottom terms. The terms not proportional to bottom slope reduce to the dispersion relation. The remaining terms make up the linear shoaling model:

$$A_x + QA = 0 \qquad (3.55)$$

where:

$$\begin{aligned} Q &= \frac{Ek_x + Fh_x}{G} & (3.56)\\ E &= gh + \omega^2h^2\alpha - 6gh^3\left(\alpha+\frac{1}{3}\right)k^2 & (3.57)\\ F &= gk + (2\alpha+\beta)\omega^2kh - gh^2(5\alpha+2+\beta)k^3 & (3.58)\\ G &= 2\left[gkh + \omega^2h^2\alpha k - 2gk^3h^3\left(\alpha+\frac{1}{3}\right)\right] & (3.59)\end{aligned}$$

where k is found from Equation (3.13). The linear shoaling model from linear theory is derived from the conservation of energy flux:

$$(C_g \mid A \mid^2)_x = 0 \qquad (3.60)$$

which yields:

$$A_x + \left(\frac{C_{gx}}{2C_g}\right)A = 0 \qquad (3.61)$$

We can use a least squares best-fit to find the value of β that will best mimic shoaling from linear theory from deep to shallow water. This involves minimizing the integral:

$$I = \int_0^{0.5} \left[Q - \left(\frac{C_{gx}}{2C_g} \right)_{linear} \right]^2 d\left(\frac{h}{L_o} \right) \tag{3.62}$$

which resulted in $\beta = -0.354$ as our optimum value. For comparison, Madsen and Sørensen (1992) performed a shoaling analysis with their extended Boussinesq model (Madsen, et al. 1991); their equivalent β was equal to $-\frac{1}{3}$. Figure 3.2 shows a comparison of shoaling coefficient found by linear theory against those found by (3.55) for several values of β. It is apparent that $\beta = -0.354$ best matches linear theory from deep to shallow water. In contrast, $\beta = 0$ performs poorly; this value of β comes from failing to recognize the ambiguous nature of the first-order substitutions.

Though this is promising, the ambiguous nature of the first-order substitutions affects the manipulation of the nonlinear terms as well. Model behavior varied drastically when different first-order substitutions were used. For example, if nonlinearity had not been dropped, Equation (3.53) would have read:

$$\begin{aligned} &\eta_{tt} + gh_x\eta_x + gh\eta_{xx} + (2\alpha+\beta)hh_x\eta_{xtt} + \alpha h^2\eta_{xxt} - gh(5\alpha+2+\beta)h_x\eta_{xxx} \\ -\ & gh^3\left(\alpha + \frac{1}{3}\right)\eta_{xxxx} - h(u_\alpha u_{\alpha x})_x + (\eta u_\alpha)_{xt} = 0 \end{aligned} \tag{3.63}$$

We wish to eliminate u_α in favor of η in the nonlinear terms. We do this by substituting first-order relations between η and u_α. Let us isolate one nonlinear term:

$$(\eta u_\alpha)_{xt} \tag{3.64}$$

and examine two possible substitutions. Expanding the t-derivative and using (3.46) as a substitution yields:

$$(\eta_t u_\alpha - g\eta\eta_x)_x \tag{3.65}$$

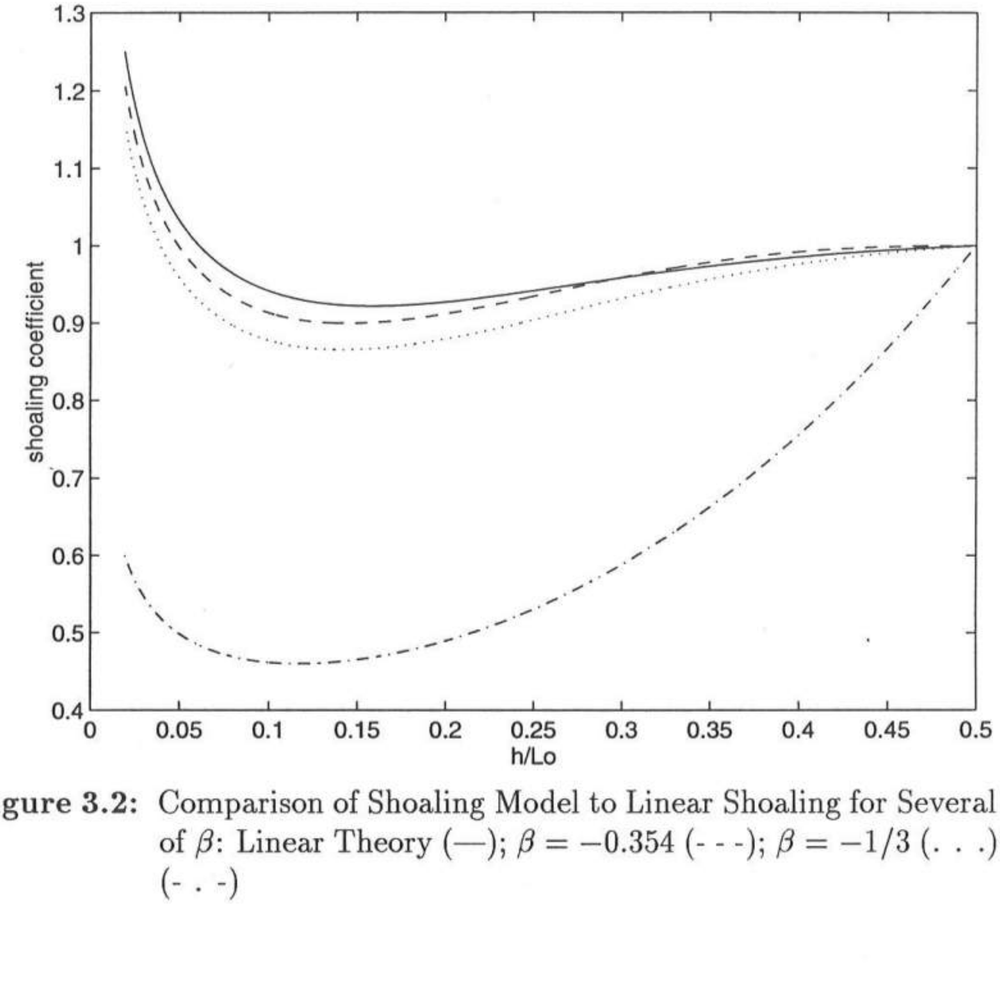

Figure 3.2: Comparison of Shoaling Model to Linear Shoaling for Several Values of β: Linear Theory (—); $\beta = -0.354$ (- - -); $\beta = -1/3$ (. . .); $\beta = 0$ (- . -)

Taking the Fourier transform of this term and seeking an evolution equation for the amplitudes of η (as was done for the amplitudes of ϕ_α) would result in the following term being present in the resulting interaction coefficient analogous to the coefficient $\tilde{R}$ of Equation (3.28):

$$\frac{n(lk_{n-l}^2 + nk_l k_{n-l} + (n-l)k_l^2)}{l(n-l)} \tag{3.66}$$

The resulting interaction coefficient analogous to $\tilde{S}$ of Equation (3.29) would contain:

$$\frac{n(lk_{n+l}^2 + nk_l k_{n+l} - (n+l)k_l^2)}{l(n+l)} \tag{3.67}$$

Different terms can be calculated by expanding (3.64) completely in x-and-t-derivatives:

$$\eta_{xt}u_\alpha + \eta_t u_{\alpha x} + \eta_x u_{\alpha t} + \eta u_{\alpha xt} \tag{3.68}$$

Then, making use of the following substitution:

$$u_{\alpha x} = -\frac{\eta_t}{h} \tag{3.69}$$

as well as (3.46), the resulting evolution equation for the amplitudes of η includes the following term in the interaction coefficient analogous to $\tilde{R}$ in Equation (3.28):

$$\frac{n^2 k_l k_{n-l}}{l(n-l)} + \frac{n^2\omega^2}{gh} \tag{3.70}$$

and the following term in the interaction coefficient analogous to $\tilde{S}$ in Equation (3.29):

$$\frac{n^2 k_l k_{n+l}}{l(n+l)} + \frac{n^2\omega^2}{gh} \tag{3.71}$$

It is likely that (3.66) and (3.70) would behave quite differently. This can be said of (3.67) and (3.71) as well. These are only two ambiguities of many. In addition, unlike the linear shoaling problem, we do not have a benchmark model to which we can compare. However, the derivation of (3.7) and (3.8) involved no ambiguities in the linear terms, and only one very straightforward ambiguity in the nonlinear terms which was very easily resolved. Additionally, as stated in Chen and Liu (1993), the dispersion relation (3.11) was maintained. Thus, we derived the fully nonlinear extended Boussinesq equations in terms of (η, ϕ_α) rather than $(\eta, \mathbf{u}_\alpha)$.

3.6.2 Comparison of Linear Shoaling Models

So far, we have four linear shoaling models: that of linear theory (3.61), the β-dependent model described in the previous section (with $\beta = -0.354$), Green's Law (1.11), and the linearized version of (3.37) and (3.38). Another linear shoaling model can be derived by simply changing the group velocity calculation in (3.61) from linear theory to (3.14):

$$A_x + \left(\frac{C_{gx}}{2C_g}\right)_{(3.14)} A = 0 \tag{3.72}$$

Figures (3.3) and (3.4) show comparisons between all five shoaling models for two ranges of water depths. Figure (3.3) shows shoaling coefficents from the deep water limit of $\frac{h}{L_o}$ to shallow water. It appears that for this case the β-dependent model of (3.55) exhibits excellent agreement to shoaling from linear theory. As expected, Green's Law performs poorly compared to linear theory. This occurred because we started our simulation in deep water, well outside the range of validity for this shallow water shoaling model. What is surprising is that the simple relation (3.72) compares better to linear theory than the linearized version of (3.37) and (3.38). This clearly indicates that improved linear dispersion does not guarantee improved linear shoaling characteristics. It may be argued that the fully nonlinear extended Boussinesq equation, for all the improvements to linear

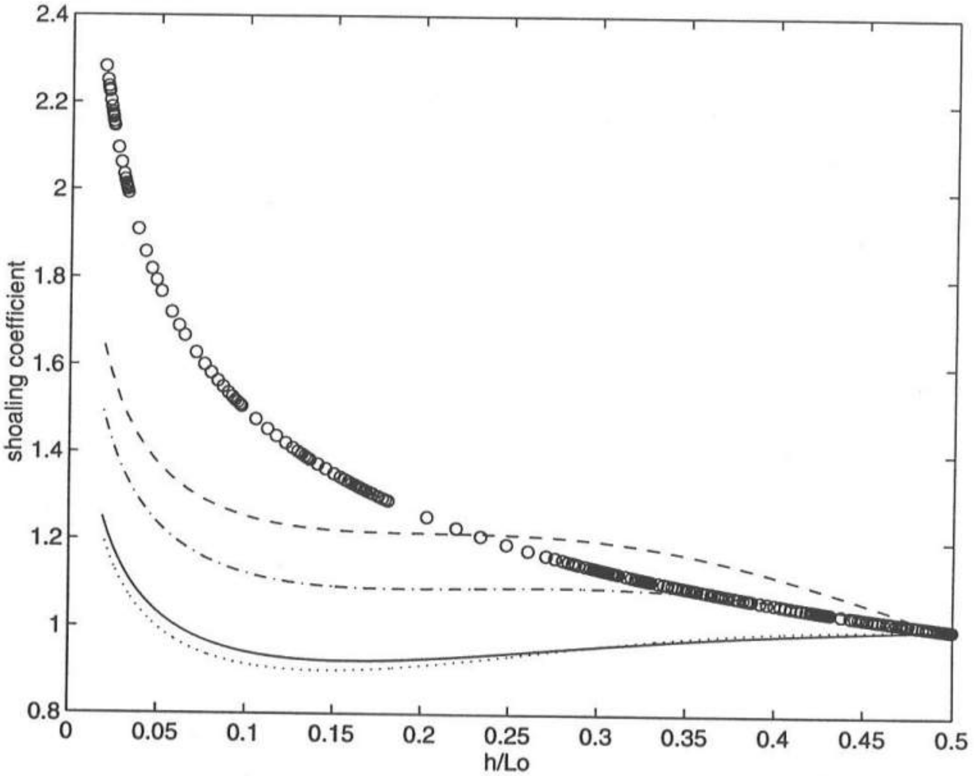

Figure 3.3: Comparison of Shoaling Models (Deep Water): Linear Theory (–); Linearized (η, ϕ_α) Equations (- -); β-Dependent Shoaling Model with $\beta = -0.354$ (. .); Energy Flux Conservation Model Using Approximate Group Velocity Expression (- .); Green's Law (oo)

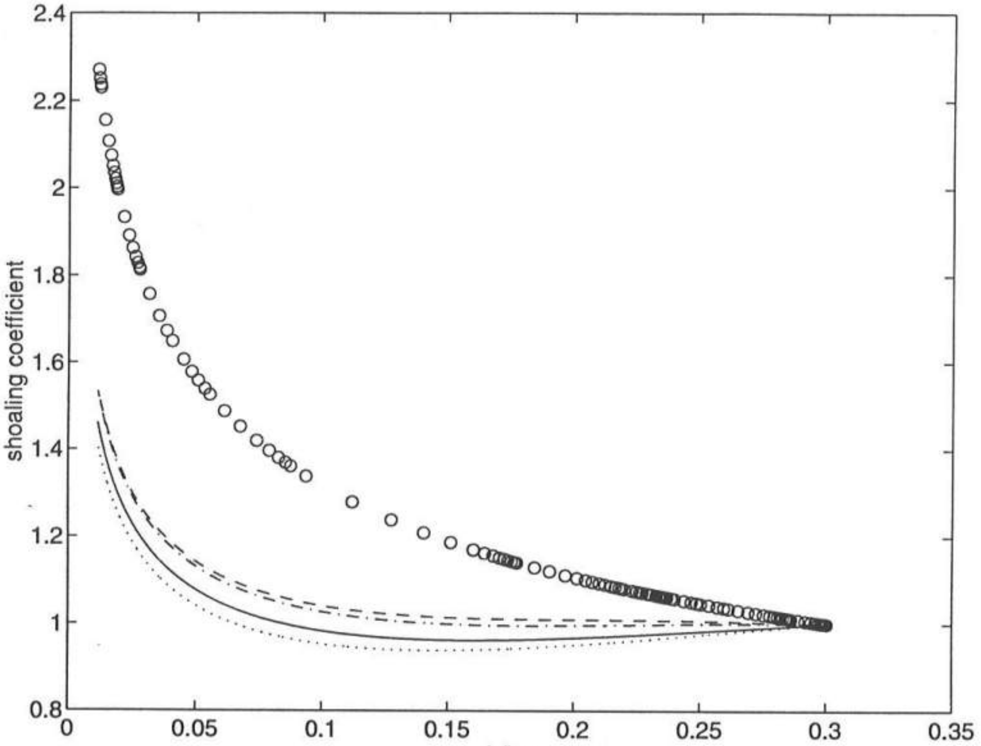

Figure 3.4: Comparison of Shoaling Models (Intermediate Water): Linear Theory (—); Linearized (η, ϕ_α) Equations (- -); β-Dependent Shoaling Model with $\beta = -0.354$ (. .); Energy Flux Conservation Model Using Approximate Group Velocity Expression (- .); Green's Law (oo)

dispersion in deeper water, is still limited to at most intermediate water depth because the horizontal velocity profile is still quadratic with depth. Additionally, as we outlined in the last chapter, the use of resonant triads, as we have done here, can be problematic in deep water. Thus we should investigate the behavior of these shoaling models starting from a point in intermediate water depth rather than deep water. Figure (3.4) shows a comparison between all five shoaling models beginning from $\frac{h}{L_o} = 0.3$. This is the $\frac{h}{L_o}$ value of the peak frequency of Case 2 of the experiment of Mase and Kirby (1992) at the wavemaker. We will compare this model to that experiment. The figure shows that all the more dispersive shoaling models (all except Green's Law) begin to approach shoaling by linear theory. In contrast, Green's Law again does poorly. Thus, we can expect that the model equations (3.37) and (3.38) would perform well for wave parameters in the intermediate water depth range.

3.7 Summary

In this chapter we have outlined the derivation of the fully nonlinear extended Boussinesq equations of Kirby and Wei (1994). We then truncated them to $O(\delta\mu^2)$ in order to retain only quadratic nonlinearity, and transformed the equations into the frequency domain using triad resonant interactions between components. We then assumed a propagating wave train, and obtained two parabolic equations, one for the evolution of the amplitudes of ϕ_α, Equation (3.35), and one for the evolution of the amplitudes of η, Equation (3.36), which is calculated directly from the amplitudes of ϕ_α. For completeness we also reduced the two-dimensional parabolic equations to one dimension, yielding (3.37) and (3.38). While the linear terms are essentially those of Chen and Liu (1993), it is an advance on their work due to the retention of $O(\delta\mu^2)$ terms.

The final section in this chapter discussed linear shoaling. We saw that a linear shoaling model based on the fully nonlinear extended Boussinesq equations expressed in terms of $(\eta, \mathbf{u}_\alpha)$ as opposed to (η, ϕ_α) required a best-fit free parameter β in order to compare well to linear theory. This is because the substitutions of first-order terms to eliminate $\mathbf{u}_\alpha$ in favor of η are ambiguous, in that these first-order relations between $\mathbf{u}_\alpha$ and η can be differentiated freely with respect to x or t before substitution, yielding different shoaling models that compare by varying degrees to linear theory. This β correction term was input into the wave equation (3.49), and the shoaling term calculated. This shoaling term was calibrated to match the shoaling term from linear theory, which occurs if $\beta = -0.354$. This β factor circumvented the ambiguities in the first-order substitutions used to develop (3.53). We saw in Figure (3.3) that the β-dependent model compared better to linear theory than the linear shoaling model from (3.37) and (3.38). Despite this, we will continue to use the (η, ϕ_α) model. We have shown that the ambiguities in the first-order substitutions that were overcome by the β factor in the $(\eta, \mathbf{u}_\alpha)$ affected the nonlinear terms as well, yielding different terms in the nonlinear interaction coefficients that may yield drastically different model behavior. In contrast, the (η, ϕ_α) model was derived without any ambiguities in the first-order substitutions for the linear terms and only one ambiguity in the nonlinear terms. Additionally, (3.4) shows that the linearized (η, ϕ_α) model compares as well to linear theory as the other dispersive shoaling models if started in intermediate water depth. This is a reasonable restriction, as the quadratic horizontal velocity profile and the use of resonant triad interactions may preclude the model from being fully applicable to deep water. Thus we use the (η, ϕ_α) equations in our simulations.

Chapter 4

COMPARISONS TO DATA - ONE-DIMENSIONAL AND PARABOLIC MODELS

In this chapter, we will present comparisons of the models described in the previous two chapters to experimental data. In addition, we will also compare them with previously-formulated models to determine the degree of improvement exhibited by the models in this study.

4.1 Comparison of Parabolic Models to Whalin (1971)

Whalin (1971) conducted a laboratory experiment to investigate the limits of linear refraction theory. He generated sinusoidal waves of 1, 2, and 3 second periods and ran them over bathymetry that resembled a tilted cylinder. The bottom contours and tank dimensions are shown in Figure 4.1. We only compare the 2 and 3 second cases; the 1 second case will be discussed later in this section. The wave parameters for the cases used in the comparison are shown in Table 4.1, where the tank depth used in calculating the nonlinearity parameter $\frac{a_o}{h}$ and the dispersion parameter $\frac{\omega^2 h}{g}$ was chosen to maximize the values of these parameters. He placed gages at certain locations along the centerline, and calculated the amplitudes of the first three harmonics. This experiment demonstrated the inadequacy of non-diffractive linear refraction theory as a modeling methodology; a strong

Table 4.1: Wave Parameters of Experiment of Whalin (1971) Used In Data-Model Comparisons. ($h_1 = 45.7\ cm$; $h_2 = 15.2\ cm$.)

T (sec)	a_0 (cm)	$\frac{a_o}{h_2}$	$\frac{\omega^2 h_1}{g}$
3	0.68	0.0446	0.2044
3	0.98	0.0643	0.2044
3	1.46	0.0958	0.2044
2	0.75	0.0490	0.4599
2	1.06	0.0675	0.4599
2	1.49	0.0949	0.4599

focal point downwave of the top of the tilted cylinder would indicate an infinite waveheight per linear refraction theory, which would be impossible. Diffraction is very prevalent there. Additionally, using a linear sinusoidal wave generates higher harmonics since the nonlinear boundary conditions cannot be satisfied by a single harmonic.

We ran the parabolic nonlinear mild-slope model (Equation 2.55) and the parabolic fully nonlinear extended Boussinesq model (Equations 3.35 and 3.36) against the data of Whalin (1971) using the parameters shown in Table 4.1. We also ran the parabolic frequency-domain KP model of Liu et al. (1985) (Equation 2.56) and the extended Boussinesq model of Chen and Liu (1993). We used a grid spacing of $\Delta x = 0.12m$ and $\Delta y = 0.08m$. No substantial improvement was noted when the stepsizes were halved. Because Equation (3.35) is in terms of the amplitudes of ϕ_α, we must convert the initial amplitudes of the free surface elevation as reported by Whalin (1971) as follows:

$$b_{n0} = \frac{-ig}{\omega_n[1 - \alpha(k_{n0}h_0)^2]} a_{n0} \tag{4.1}$$

This relationship is found from the linear terms of Equation 3.16.

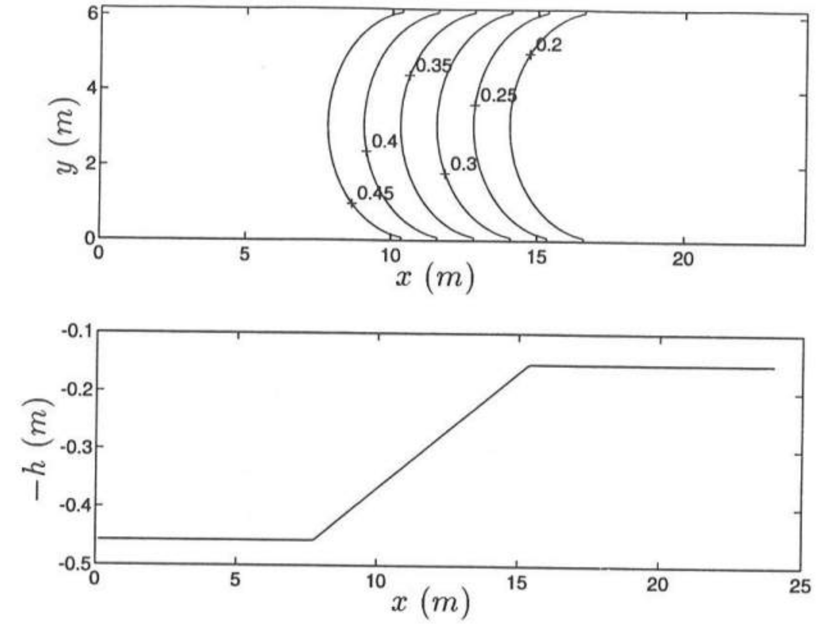

Figure 4.1: Wavetank Layout of Experiment of Whalin (1971): (Top) Bottom Contours; (Bottom) Centerline Depth.

Figures 4.2 through 4.4 show the comparisons between the models and Whalin's data for the case of $T = 3$ seconds. It is apparent that neither model predicts the first harmonic amplitudes particularly well. This seems to be endemic of most data-model comparisons done in the literature where Whalin's 3 second data were used (e.g., Rygg 1988; Madsen and Sørensen 1992; Nwogu 1994). Liu et al. (1985) maintain that the relatively short evolution distance for a 3 second wave period (roughly two wavelengths) may at least partially violate the slowly varying assumption used to derive their frequency-domain KP model, though they do allow for some possible inconsistency in Whalin's data. In any case, all four models show reasonable comparison with the 3 second data for the second and third harmonics.

The $T = 2$ second case is more demonstrative of the advantages of the dispersive models. The value of the dispersion parameter $\frac{\omega^2 h}{g}$ in the deep portion of the tank is 0.46, which may violate the shallow water assumption used in the KP model of Liu et al. (1985). Figures 4.5 through 4.7 show these results. It is clear that the KP model overpredicts the amplitudes of all the harmonics, most notably the first. This is most likely due to the effect of Green's Law shoaling. Additionally, the parabolic fully nonlinear extended Boussinesq model of Chapter 3 appears to demonstrate the best comparison to data of all the dispersive models for this case. This is surprising, since the nonlinear mild-slope parabolic model of Chapter 2 is essentially truncated to the same order in nonlinearity and uses the *exact* dispersion relation of linear theory for the propagation characteristics. In contrast, the fully nonlinear extended Boussinesq model has a dispersion relation that *approximates* that of linear theory. One would expect the nonlinear mild-slope parabolic model to show the best agreement. Another noticible feature of the $T = 2$ second comparisons is the effect of the retention of $O(\delta\mu^2)$ terms on the second harmonic. These terms comprise the primary difference between Equations (3.35) and (3.36) and the model of Chen and Liu (1993). One would expect that, as nonlinear effects begin to influence wave shoaling, the water depth actually increases, so models with insufficient dispersion in their nonlinear terms would not react to this depth change and would likely overpredict wave amplitudes. This is analogous to the effect of insufficient dispersion in a *linear* shoaling wave model when compared to shoaling from linear theory. Figure 4.5, for example, shows this occurrence in the second harmonic. The extended Boussinesq model of Chen and Liu (1993), which is truncated to $O(\delta, \mu^2)$, overshoals the amplitude of this harmonic compared with the fully nonlinear extended Boussinesq model of Chapter 3, where terms up to $O(\delta\mu^2)$ are kept for the frequency domain treatment.

It can be argued that, in order to best demonstrate the superiority of the parabolic frequency domain models of Chapters 2 and 3, they should be compared to Whalin's $T = 1$ second case. Both Madsen and Sørensen (1992) and Nwogu (1994) compare their time-domain extended Boussinesq equations to Whalin's data for this case. They both demonstrate what they consider to be reasonable data-model agreement. The simulations of Madsen and Sørensen (1992) show a distinctive oscillation pattern over the shoal in the second harmonic. This is likely due to the celerity discrepancy between the free and bound second harmonic, as each component would travel at a significantly different speed at this water depth ($\frac{h}{L_0} = 1.118$ for the second harmonic). Chen and Liu (1993), because of their use of resonant triad interactions in their frequency domain extended Boussinesq model, explicitly separated the free second harmonic from the bound second harmonic. They then reasoned that the evolution of the bound wave would occur at a rate an order of magnitude slower than the evolution of the forcing wave, and thus eliminated all derivative terms for their evolution equation for the second harmonic. This yielded an explicit relationship between the amplitudes of this bound harmonic and the amplitudes of the primary forcing harmonic, with no consideration of the free second harmonic whatsoever. Using this reduced model, they compared their results to Whalin's experiment for $T = 1$ second, and also achieved reasonable agreement. However, since they modeled only the primary and bound harmonics, they did not achieve the oscillation pattern present in Madsen and Sørensens' model and also present in the experimental data. A similar treatment could be performed for the present parabolic models, but is not done here. It is felt that the $T = 2$ second case simulations adequately demonstrates the utility of a more dispersive nonlinear wave propagation model.

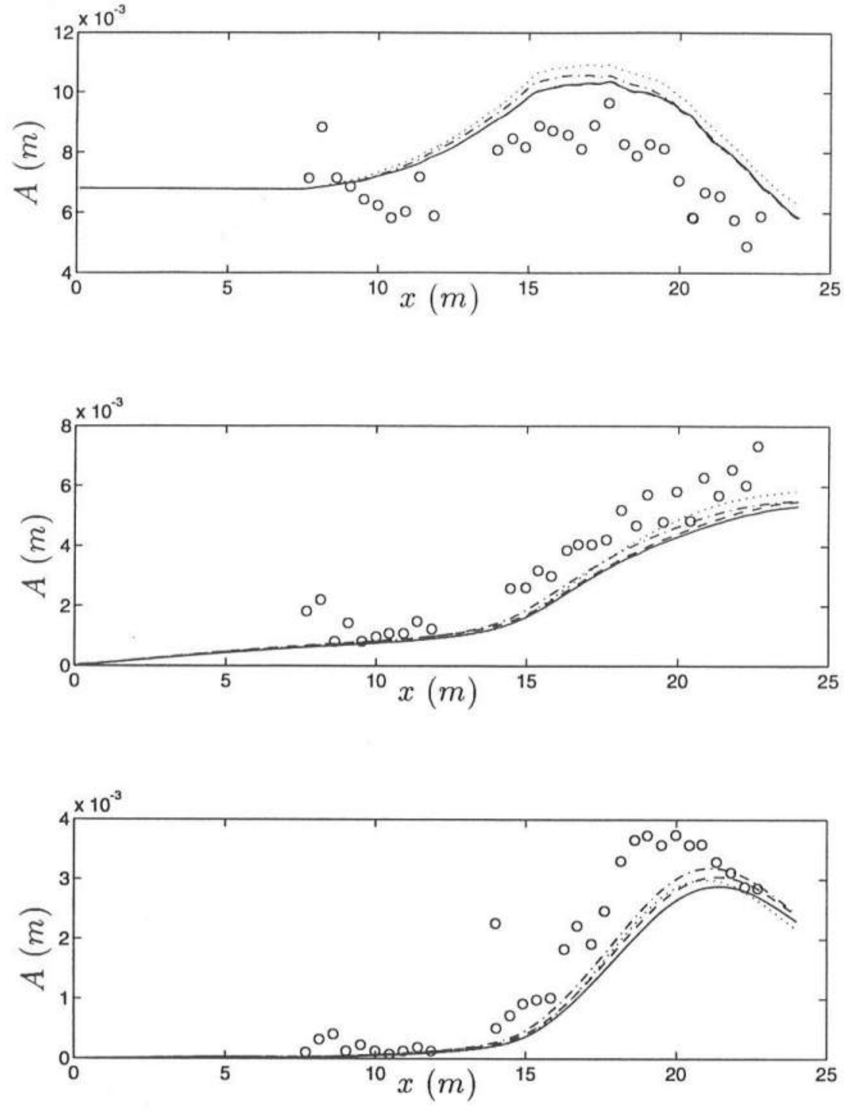

Figure 4.2: Comparisons Between Models and Whalin's Experiment, $T = 3$s, $a_o = 0.68$cm. Fully Nonlinear Extended Boussinesq Model (–), Extended Boussinesq Model of Chen and Liu (1993) (- -), Nonlinear Mild-Slope Model (-.-), KP Model of Liu et al. (1985) (..), Data of Whalin (1971) (oo). (Top) First Harmonic; (Middle) Second Harmonic; (Bottom) Third Harmonic.

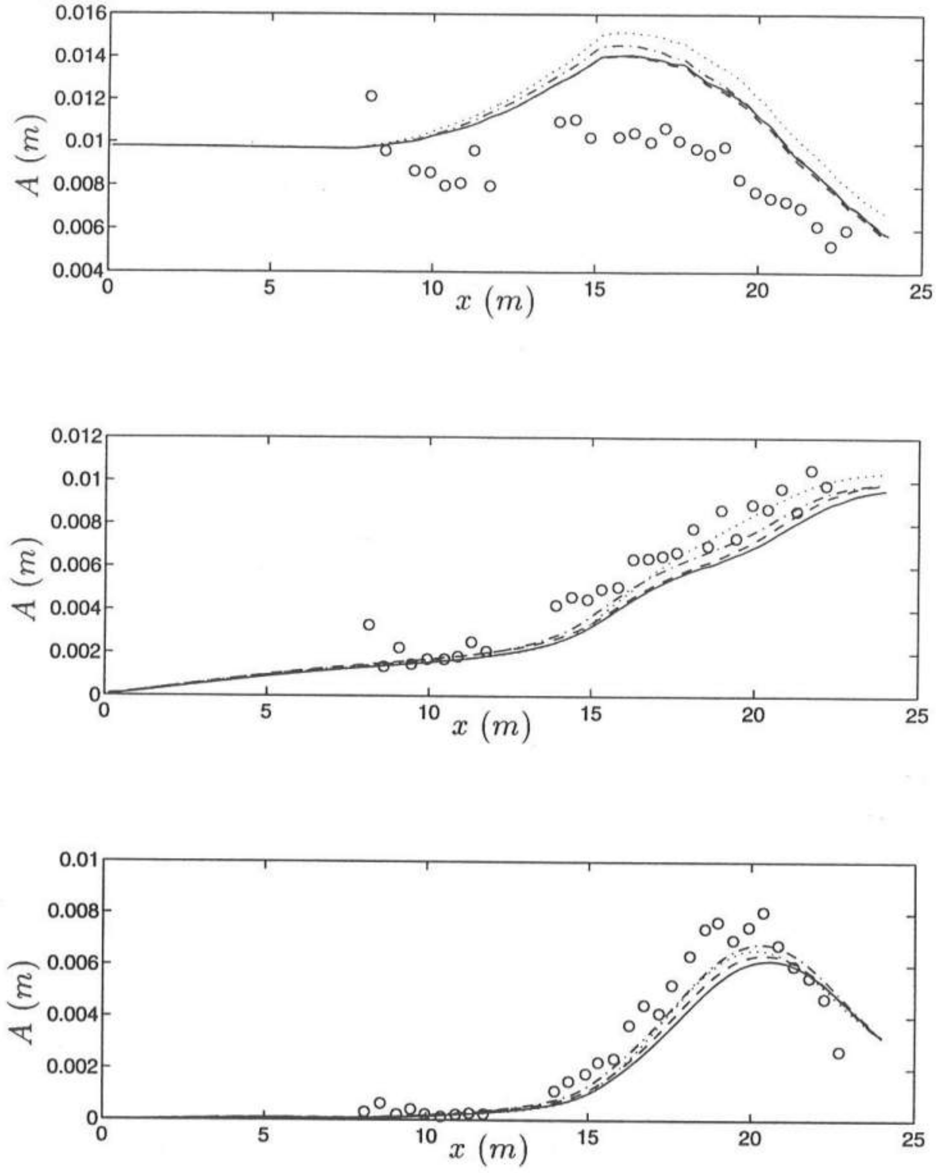

Figure 4.3: Comparisons Between Models and Whalin's Experiment, $T = 3\text{s}$, $a_o = 0.98\text{cm}$. Fully Nonlinear Extended Boussinesq Model (–), Extended Boussinesq Model of Chen and Liu (1993) (- -), Nonlinear Mild-Slope Model (-.-), KP Model of Liu et al. (1985) (..), Data of Whalin (1971) (oo). (Top) First Harmonic; (Middle) Second Harmonic; (Bottom) Third Harmonic.

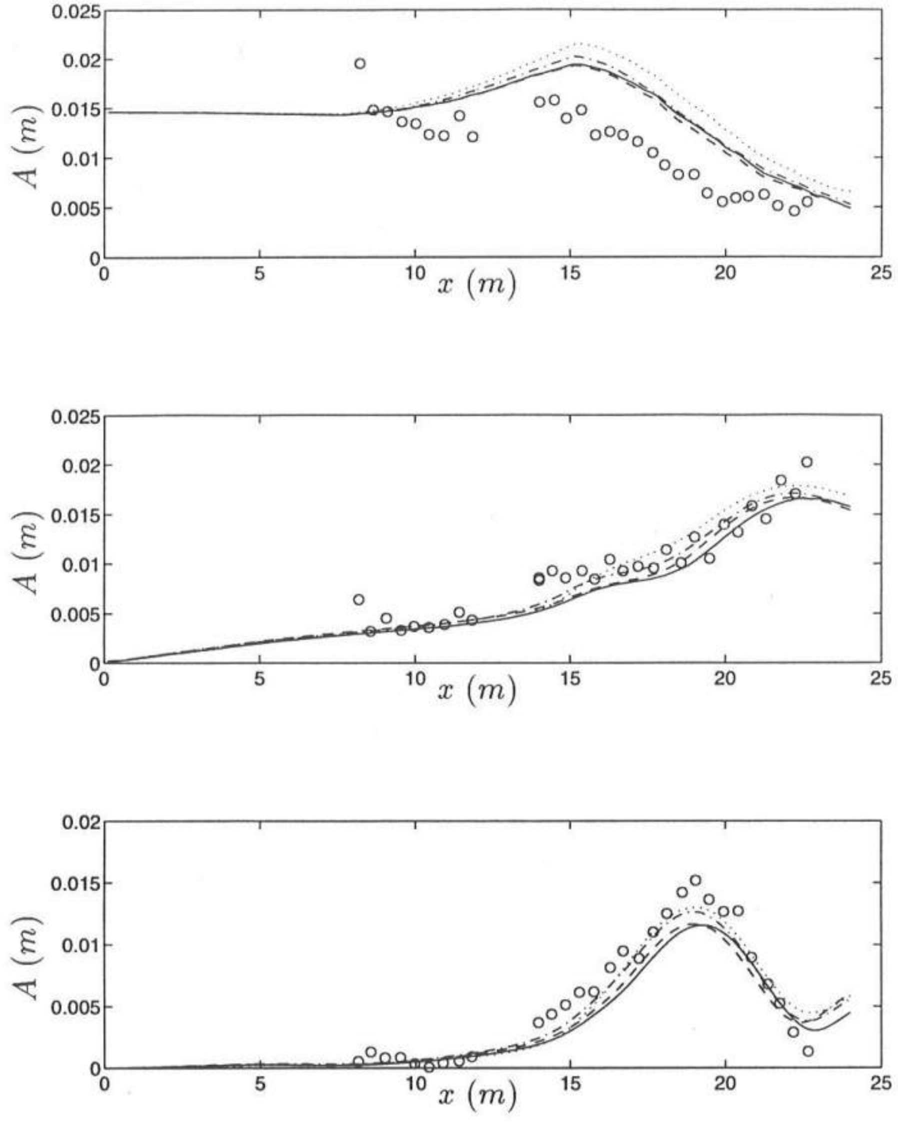

Figure 4.4: Comparisons Between Models and Whalin's Experiment, $T = 3$s, $a_o = 1.46$cm. Fully Nonlinear Extended Boussinesq Model (–), Extended Boussinesq Model of Chen and Liu (1993) (- -), Nonlinear Mild-Slope Model (-.-), KP Model of Liu et al. (1985) (..), Data of Whalin (1971) (oo). (Top) First Harmonic; (Middle) Second Harmonic; (Bottom) Third Harmonic.

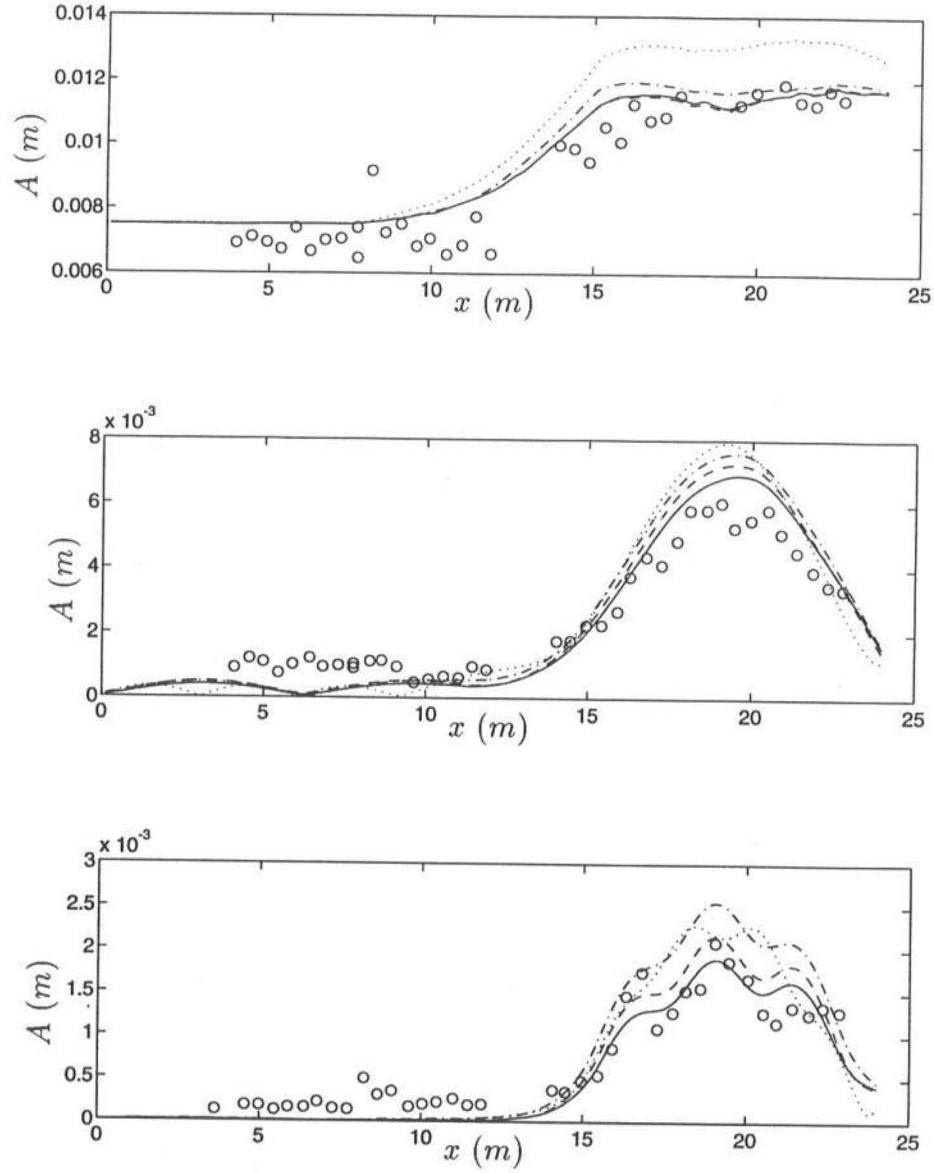

Figure 4.5: Comparisons Between Models and Whalin's Experiment, $T = 2$s, $a_o = 0.75$cm. Fully Nonlinear Extended Boussinesq Model (–), Extended Boussinesq Model of Chen and Liu (1993) (- -), Nonlinear Mild-Slope Model (-.-), KP Model of Liu et al. (1985) (..) Data of Whalin (1971) (oo). (Top) First Harmonic; (Middle) Second Harmonic; (Bottom) Third Harmonic.

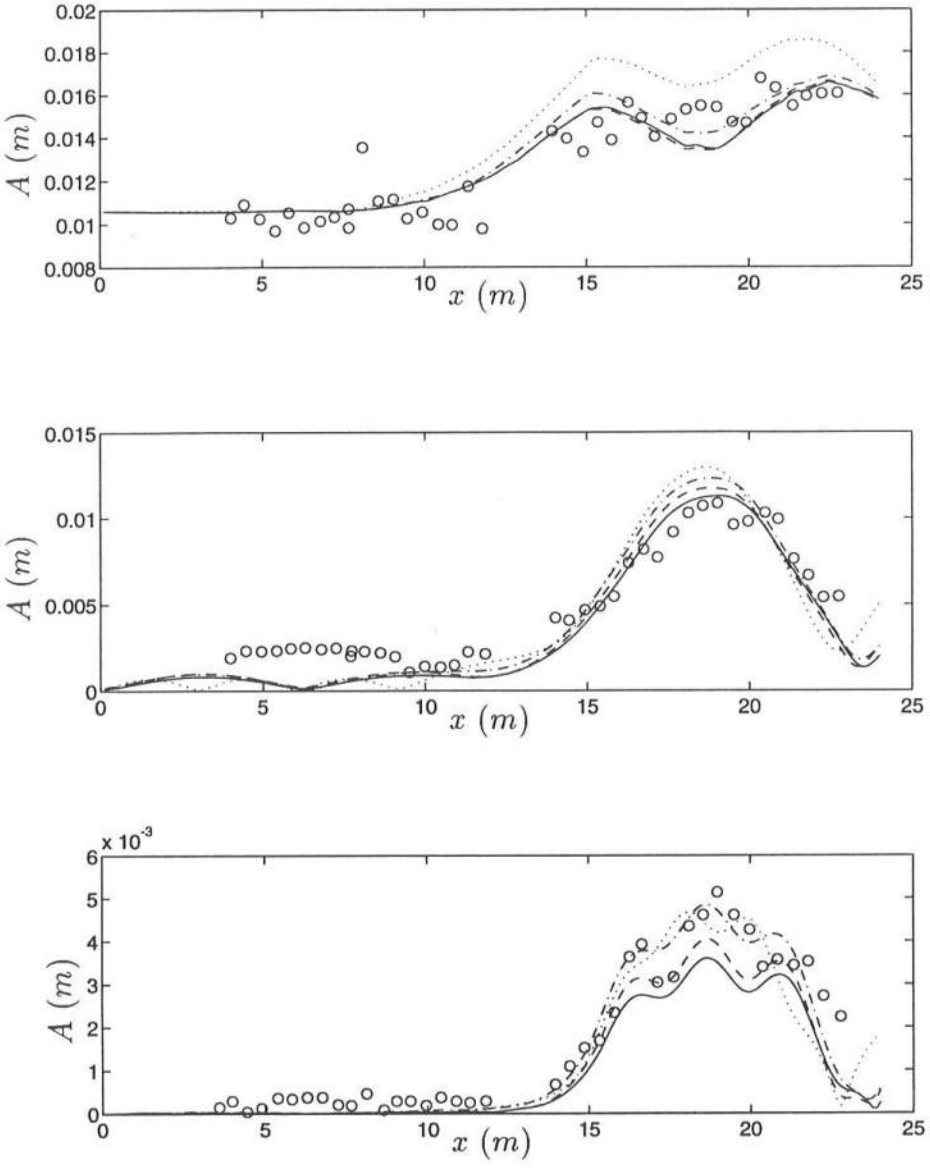

Figure 4.6: Comparisons Between Models and Whalin's Experiment, $T = 2$s, $a_o = 1.06$cm. Fully Nonlinear Extended Boussinesq Model (–), Extended Boussinesq Model of Chen and Liu (1993) (- -), Nonlinear Mild-Slope Model (-.-), KP Model of Liu et al. (1985) (..), Data of Whalin (1971) (oo). (Top) First Harmonic; (Middle) Second Harmonic; (Bottom) Third Harmonic.

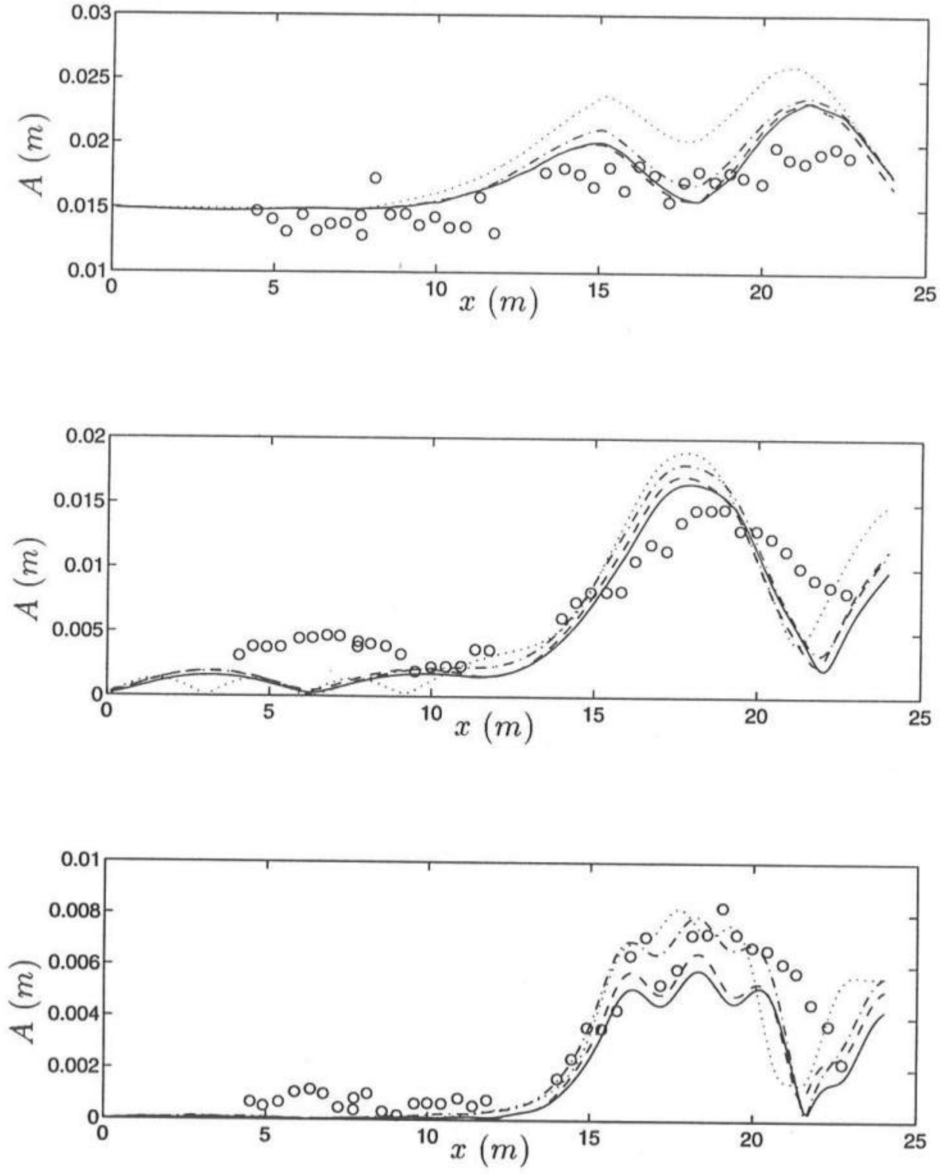

Figure 4.7: Comparisons Between Models and Whalin's Experiment, $T = 2$s, $a_o = 1.49$cm. Fully Nonlinear Extended Boussinesq Model (–), Extended Boussinesq Model of Chen and Liu (1993) (- -), Nonlinear Mild-Slope Model (-.-), KP Model of Liu et al. (1985) (..), Data of Whalin (1971) (oo). (Top) First Harmonic; (Middle) Second Harmonic; (Bottom) Third Harmonic.

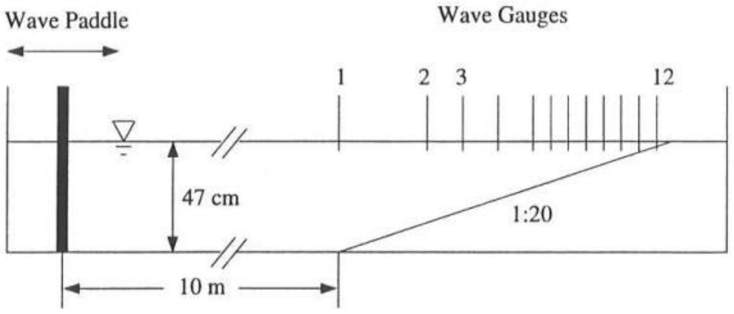

Figure 4.8: Experimental Setup of Mase and Kirby (1992) (from Wei and Kirby 1994)

4.2 Comparison to Mase and Kirby (1992)

4.2.1 Introduction

Mase and Kirby (1992) conducted an irregular wave shoaling experiment in a wave flume with a sloping bottom. This experiment was performed to study the process of shoaling and breaking of spectral waves in which the peak frequency component was outside the shallow water range. The experimental setup is shown in Figure 4.8, which was taken from Wei and Kirby (1994).

They generated a Pierson-Moskowitz spectrum at the wavemaker for two different values of peak frequency. Case 1 had a peak frequency of $f_p = 0.6Hz$, resulting in a surf zone where plunging breakers dominated. Case 2, the experiment of interest to the present study, had a peak frequency of $f_p = 1.0Hz$; this caused spilling breakers to dominate the surf zone. The experiment is useful for verification because though the peak frequency is in intermediate water depth, there is significant energy in frequency bands that are in deep water. This would be a demanding test for the dispersive models detailed so far in this study. We will simulate the experiment with three shoaling models: the fully dispersive nonlinear shoaling model (Equation 2.58), which has linear shoaling properties from linear theory; the consistent shoaling model of Freilich and Guza (1984) (Equation 2.59), which uses Green's Law for its shoaling mechanism; and the fully nonlinear extended Boussinesq model (Equations 3.37 and 3.38). The results of these simulations will be compared to the experimental data.

4.2.2 Energy Dissipation

Because we will be operating the shoaling models of this study in the surf zone, we require a dissipation mechanism by which we can drain energy out of the system. The basic dissipation model is detailed in Kirby, et al. (1992a) and Mase and Kirby (1992). We outline the basic features here.

In general, our shoaling models take the following form after linearization:

$$A_{nx} + \frac{C_{gnx}}{2C_{gn}} A_n = 0 \tag{4.2}$$

This is a statement of energy flux conservation. We can include a damping term:

$$A_{nx} + \frac{C_{gnx}}{2C_{gn}} A_n + \tilde{\alpha}_n A_n = 0 \tag{4.3}$$

where $\tilde{\alpha}_n$ is a damping coefficient. The form of $\tilde{\alpha}_n$ depends on the sort of frequency distribution one would use to spread the dissipation across the spectrum. If we write an equation like (4.3) for the conjugate amplitudes A_n^*, multiply each equation by its conjugate amplitude, and add, we obtain a statement of energy conservation:

$$\sum_{n=1}^{N} \left(C_{gn} \mid A_n \mid^2 \right)_x = -2 \sum_{n=1}^{N} \tilde{\alpha_n} C_g \mid A_n \mid^2 \tag{4.4}$$

If we take $C_{gn} = \sqrt{gh}$ and define the spectral energy content:

$$E = \frac{1}{2} \rho g \sum_{n=1}^{N} \mid A_n \mid^2 \tag{4.5}$$

we obtain:

$$\left(E\sqrt{gh}\right)_x = -\rho g\sqrt{gh}\left(\sum_{n=1}^{N} \tilde{\alpha}_n \mid A_n \mid^2\right) \tag{4.6}$$

where ρ is unit mass density of water. Equation (4.6) is a statement of a change in energy flux. We know that this change will be due to dissipation, so we still require a dissipation function that will drain the energy from the system. For this purpose we use the simple model of Thornton and Guza (1983), which is stated as a change of energy flux:

$$\left(E\sqrt{gh}\right)_x = -\langle\epsilon_b\rangle \tag{4.7}$$

where:

$$\langle\epsilon_b\rangle = \frac{3\sqrt{\pi}}{16}\rho g\frac{B^3\overline{f}}{\gamma^4 h^3}H_{rms}^5 \tag{4.8}$$

is a probabilistic dissipation function based on the assumption of a narrow banded distribution. H_{rms}, the root-mean-square waveheight, is defined as:

$$H_{rms} = 2\sqrt{\sum_{n=1}^{N} \mid A_n \mid^2} \tag{4.9}$$

Equation (4.8) contains the free parameters B, $\overline{f}$, and γ. They have ostensible physical meanings, however: B is the percentage of wave height covered in white water; $\overline{f}$ is an arbitrarily-defined characteristic frequency, and γ is the ratio of H_{rms} to water depth in the saturated surf zone. Mase and Kirby (1992) determined that the best results would be obtained from the following values:

$$B = 1.0 \tag{4.10}$$

$$\overline{f} = f_{peak} \tag{4.11}$$

$$\gamma = 0.6 \tag{4.12}$$

Thornton and Guza (1983) determined that a value of $\gamma = 0.42$ worked well against their field data. They then used B as a best-fit parameter, and found that

$B = 1.3 - 1.7$ for field data and $B = 0.8$ for laboratory data. The values used in this study are certainly in the range of those used by Thornton and Guza (1983). Equating the right-hand sides of (4.6) and (4.7) yields:

$$\sum_{n=1}^{N} \tilde{\alpha}_n \mid A_n \mid^2 = \frac{3\sqrt{\pi}}{16\sqrt{gh}} \frac{B^3 f_{peak} (2\sqrt{\sum_{n=1}^{N} \mid A_n \mid^2})^5}{\gamma^2 h^3} \equiv \tilde{\beta}(x) \sum_{n=1}^{N} \mid A_n \mid^2 \qquad (4.13)$$

We still require a specification for $\tilde{\alpha}_n$. Mase and Kirby (1992) investigate empirically the trends that a back-calculated $\tilde{\alpha}_n$ would have in the data. They found a strong f^2 dependence for $\tilde{\alpha}_n$, which would be analogous to the behavior of the viscous damping term of the Burger's equations after frequency-domain transformation. It was postulated by Kirby, et al. (1992a) that a reasonable representation of the trends of the dissipation across the frequency components can be achieved by writing $\tilde{\alpha}_n$ in the following form:

$$\tilde{\alpha}_n = \tilde{\alpha}_{n0} + \left(\frac{f_n}{f_{peak}} \right)^2 \tilde{\alpha}_{n1} \qquad (4.14)$$

where:

$$\begin{aligned} \tilde{\alpha}_{n0} &= \tilde{F} \tilde{\beta}(x) && (4.15) \\ \tilde{\alpha}_{n1} &= \left(\tilde{\beta}(x) - \tilde{\alpha}_{n0} \right) \frac{f_{peak}^2 \sum_{n=1}^{N} \mid A_n \mid^2}{\sum_{n=1}^{N} f_n^2 \mid A_n \mid^2} && (4.16) \end{aligned}$$

It is apparent that $\tilde{\alpha}_{n0}$ represents a constant percentage of energy drain over all frequencies, while $\tilde{\alpha}_{n1}$ weights the drain higher toward higher frequencies, and thus represents the f^2 dependence of dissipation exhibited by the data. The parameter $\tilde{F}$ determines the mixture between the different frequency distributions. In model tests of the data of Mase and Kirby (1992) using the consistent model of Freilich and Guza (1984) with this dissipation, it was determined that $\tilde{F} = 0.5$ gave the best results. Thus we use this value of $\tilde{F}$ in our simulations of this experiment. Extensive comparisons against other data sets would be required to firmly establish the generality of this dissipation model. Its primary purpose in this study is to allow us to model the wave propagation into the surf zone realistically.

For the fully nonlinear extended Boussinesq model (3.37) and (3.38), no modification is required even though we are modeling the amplitudes of ϕ_α rather than of the free surface elevation η. Thus the dissipation term that is added to the left-hand side of (3.35) is:

$$\tilde{\alpha}_n B_n \tag{4.17}$$

4.2.3 Linear Shoaling as Applicable to Mase and Kirby (1992)

We discussed the problems of linear shoaling in Chapter 3, specifically with respect to the fully nonlinear extended Boussinesq model. We saw that the linear shoaling mechanism inherent in the model followed that of linear theory reasonably well if the input wave has a $\frac{h}{L_0}$ ratio no greater than 0.3 at the start of the simulation. This would be true of the peak frequency in Case 2 of Mase and Kirby (1992). However, it is instructive to determine the linear shoaling behavior of the fully nonlinear extended Boussinesq model for the range of spectral frequencies in the experiment. We perform such an analysis here.

As was done in Section 3.6, we use Green's Law (Equation 1.11), the linearized version of Equation (2.58), which has the correct linear shoaling mechanism, and the linearized version of Equations (3.37) and (3.38) to investigate linear shoaling. However, rather than use only one wave, we use ten frequencies, spanning much of the range of the truncated Fourier spectra taken from Case 2 of the experiment of Mase and Kirby (1992). We use the same bathymetry as the experiment, and do not employ dissipation.

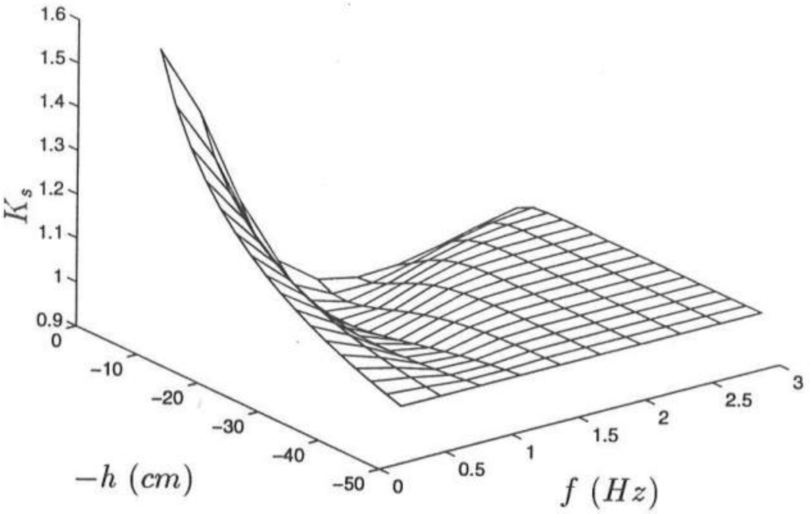

Figure 4.9: Shoaling Coefficients K_s from Linear Theory for Same Frequency Range and Bathymetry as Used in Model Comparisons to Mase and Kirby (1992)

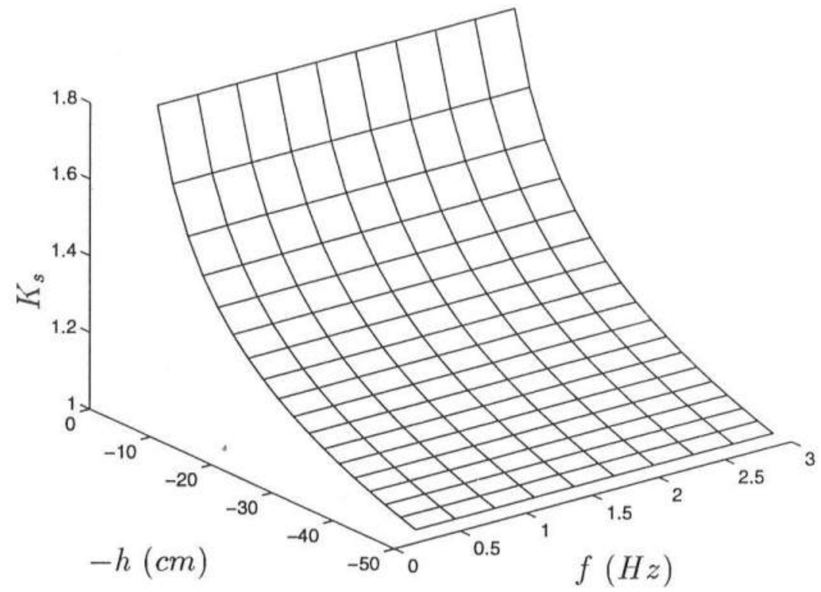

Figure 4.10: Shoaling Coefficients K_s from Green's Law, for Same Frequency Range and Bathymetry as Used in Model Comparisons to Mase and Kirby (1992)

Figure 4.9 shows the shoaling coefficients (denoted K_s) for the ten frequencies at various depths as calculated by linear theory. It demonstrates the shoaling features we are attempting to mimic with other models, namely the monotonic increase in amplitude with a decrease in water depth for the lower frequencies (shallow water) while the higher frequencies actually decrease in height with an decrease in depth for part of the propagation distance.

Figure 4.10 shows the shoaling tendencies of Green's Law (Equation 1.11) as applied to the bathymetry of Mase and Kirby (1992). As expected, there is no variation in K_s with respect to frequency. This tendency would cause overshoaling in the higher frequencies, as noted previously. Figure 4.11 shows K_s as predicted by the linearized version of the fully nonlinear extended Boussinesq equation. We

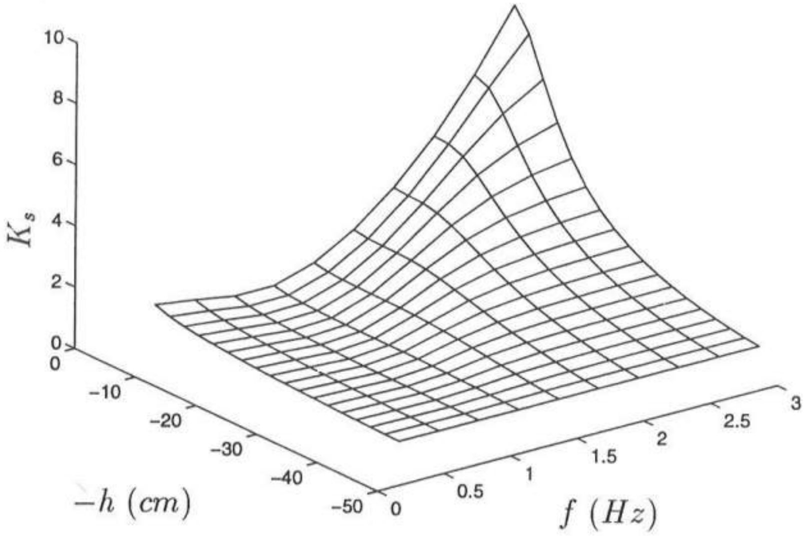

Figure 4.11: Shoaling Coefficients K_s from Fully Nonlinear Extended Boussinesq Model, for Same Frequency Range and Bathymetry as Used in Model Comparisons to Mase and Kirby (1992)

see that, while the desired tendencies seem to be exhibited for frequencies less than approximately 1 Hz, shoaling of the higher frequencies tend to be grossly overpredicted. This is symptomatic of model behavior if carried outside its range of calibration for the dispersion parameter α, which for this case would be $f \geq 1.29$ Hz.

In order to better quantify the deviation of the shoaling mechanisms of Green's Law and the fully nonlinear extended Boussinesq model, we defined a percent error as follows:

$$e(\%) = \left(\frac{\mid K_{s,approx.} - K_{s,linear} \mid}{K_{s,linear}} \right) \times 100\% \tag{4.18}$$

where $K_{s,approx.}$ denotes the shoaling coefficient from either Green's Law or the

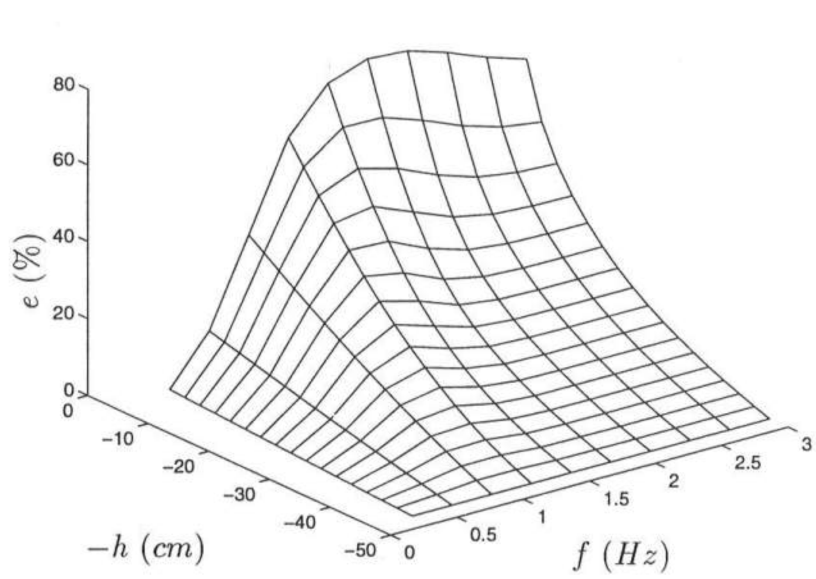

Figure 4.12: Percent Error Between Green's Law and Shoaling from Linear Theory

fully nonlinear extended Boussinesq equation.

Figure 4.12 shows the percent error incurred by using Green's Law for the experiment of Mase and Kirby (1992). It is apparent that the error climbs rapidly with an increase in frequency, as one would expect since the peak frequency for this experiment has a depth parameter $\frac{h}{L_0}$ of 0.3, well outside the range of shallow water theory. However, we note that this error curve tends to level off beyond the peak frequency. Figure 4.13 is a similar plot for the linear shoaling mechanism of the fully nonlinear extended Boussinesq model. While the error surface is fairly flat for frequencies up to the peak, it increases rapidly for the higher frequencies, finally reaching a maximum error of nearly 700% for the highest frequency. However, this frequency has a water depth parameter $\frac{h}{L_0}$ of 2.71, well beyond the calibration

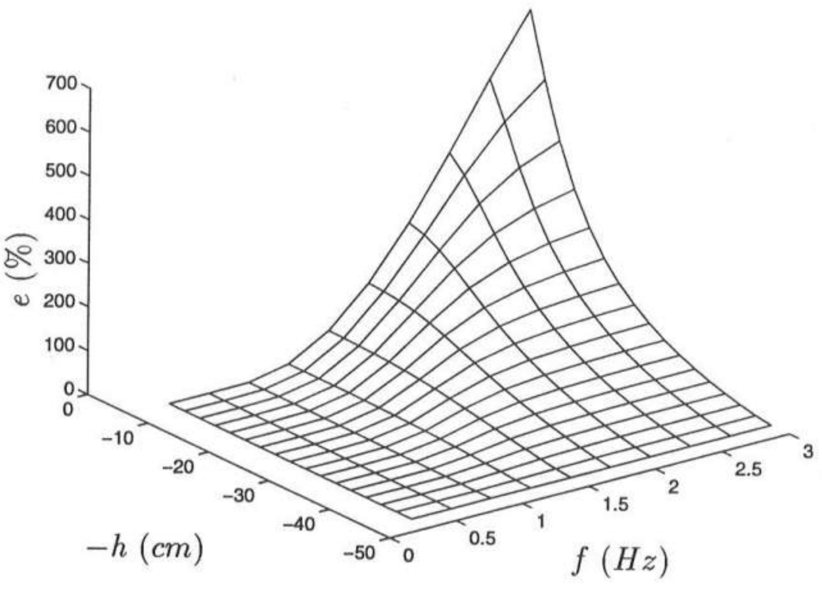

Figure 4.13: Percent Error Between Linear Shoaling from Fully Nonlinear Extended Boussinesq Equation and Shoaling from Linear Theory

Table 4.2: Table of Frequencies Analyzed for Error Comparison Between Shoaling Models Used for Case 2 of Mase and Kirby (1992)

Frequency Number	Frequency (Hz)	$\frac{h}{L_0}$
1	0.3	0.03
3	0.9	0.24
4	1.2	0.43
5	1.5	0.67
8	2.4	1.73
10	3.0	2.71

range of the dispersion parameter α shown in Section 3.3.

To look at the errors more closely, we chose several frequencies out of the range investigated, and compared the errors incurred by Green's Law to those incurred by the linear version of the fully nonlinear extended Boussinesq model. Table 4.2 shows the frequencies analyzed and their respective $\frac{h}{L_0}$ values. Figures 4.14 and 4.15 show these comparisons. It is apparent that the linear shoaling mechanism of the fully nonlinear extended Boussinesq model has lower error compared to shoaling from linear theory than Green's Law up until $f = 1.2Hz$. Beyond that the linear shoaling mechanism of the fully nonlinear extended Boussinesq model incurs much larger error than Green's Law, though both become more erroneous at these frequencies. We would thus expect that any significant deviation from the data exhibited by both the consistent shoaling model and the fully nonlinear extended Boussinesq model is a result of the partial inapplicability of these models to the range of $\frac{h}{L_0}$ of the experimental data. Additionally, based on this shoaling analysis, we would expect the fully nonlinear extended Boussinesq model to perform better than the consistent shoaling model for frequencies less than or equal to the spectral peak of the data, since the errors in linear shoaling between

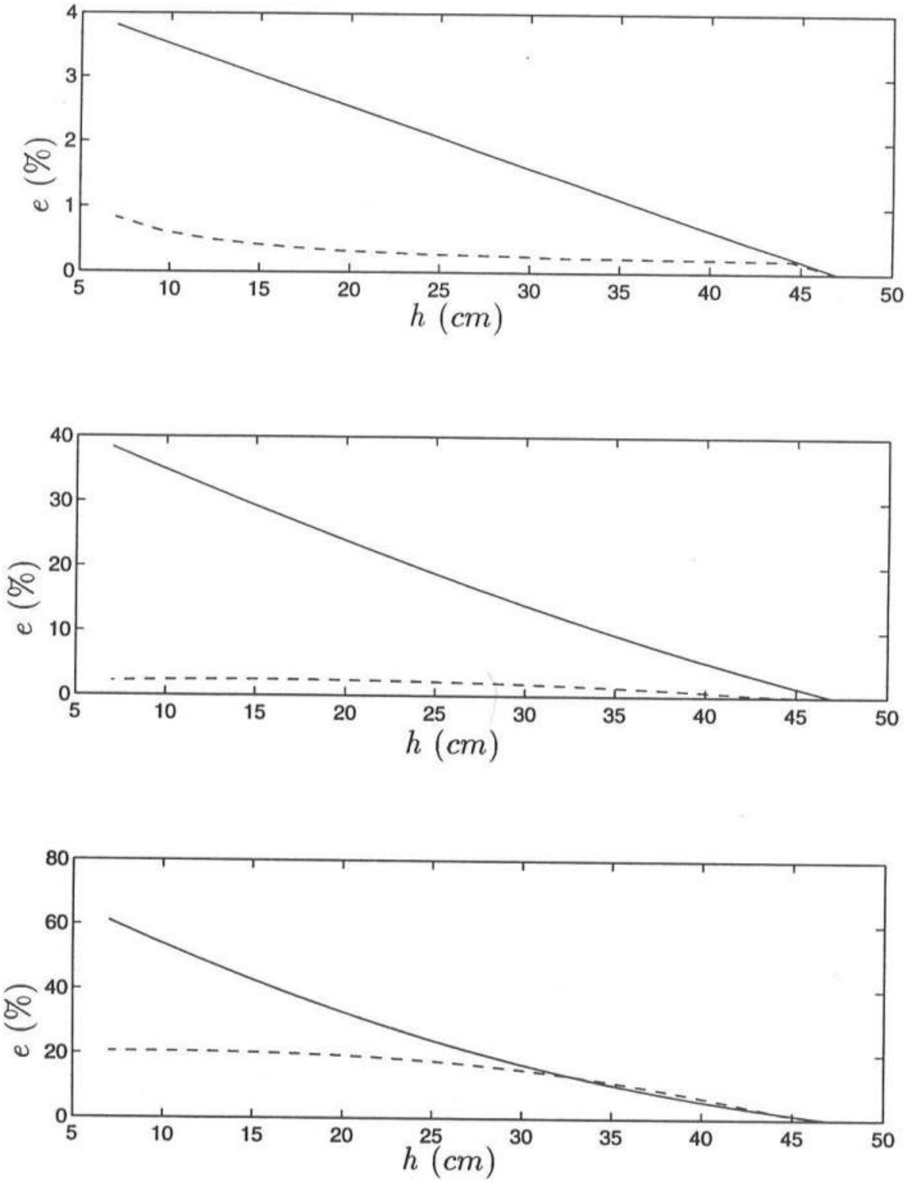

Figure 4.14: Comparison of Linear Shoaling Errors from Green's Law (–) and Fully Nonlinear Extended Boussinesq Model (- -). (Top) $f = 0.3Hz$; (Middle) $f = 0.9Hz$; (Bottom) $f = 1.2Hz$

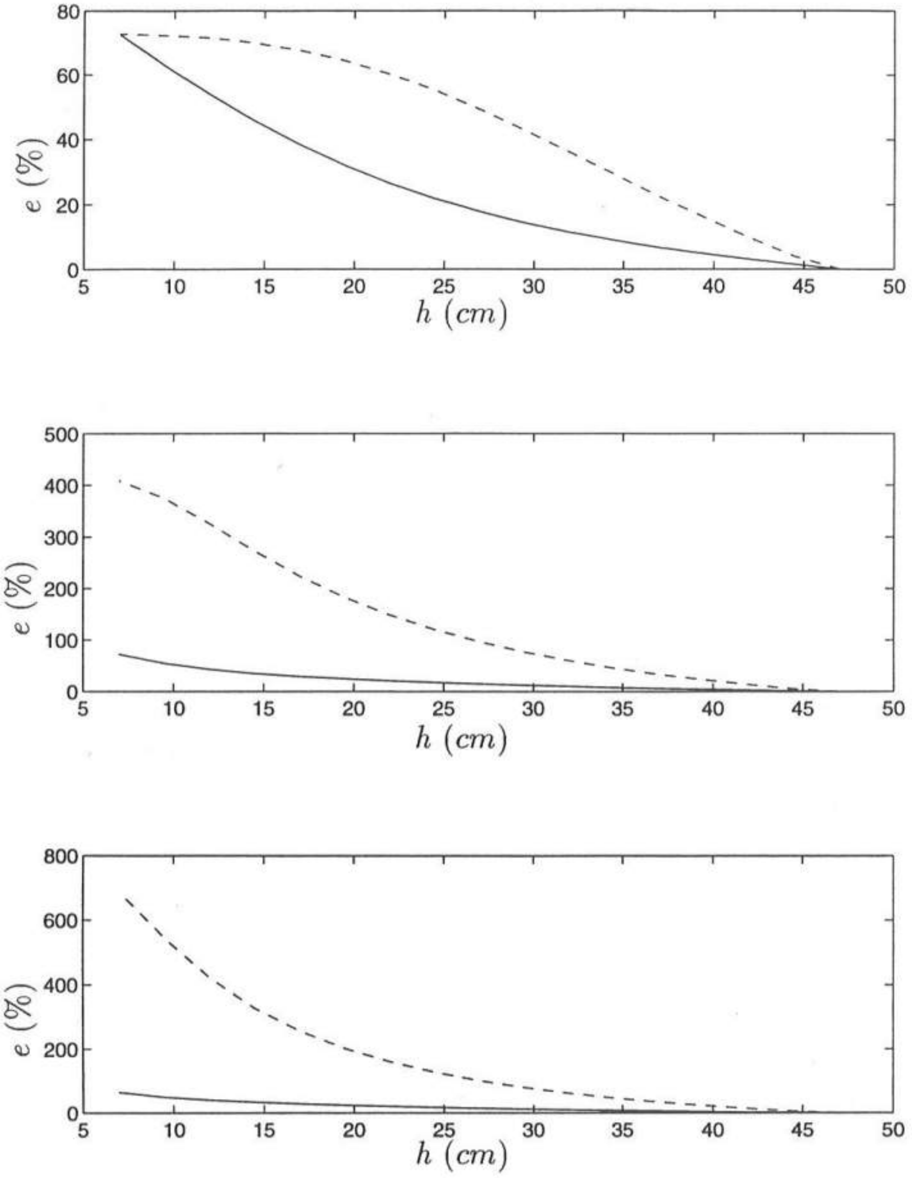

Figure 4.15: Comparison of Linear Shoaling Errors from Green's Law (–) and Fully Nonlinear Extended Boussinesq Model (- -). (Top) $f = 1.5Hz$; (Middle) $f = 2.4Hz$; (Bottom) $f = 3.0Hz$

this model and linear theory are smaller. Conversely, we would expect the consistent shoaling model to compare better to data than the fully nonlinear extended Boussinesq model for frequency ranges higher than the peak. This is not because the consistent shoaling model has small error compared to linear theory in this range, but rather because its errors are relatively smaller and level off as the frequency increases. The errors with respect to linear theory for the fully nonlinear extended Boussinesq model, on the other hand, climb almost exponentially with an increase in frequency.

4.2.4 Model to Data Comparison

As mentioned earlier, we compare three different nonlinear shoaling models to the Case 2 data of Mase and Kirby (1992). These models are: the consistent shoaling model of Freilich and Guza (1984) (Equation 2.59), the fully dispersive nonlinear shoaling model (Equation 2.58), and the frequency-domain version of the fully nonlinear extended Boussinesq model (Equations 3.37 and 3.38). All three models contain the dissipation mechanism detailed in Section 4.2.2.

Mase and Kirby (1992) took data for their Case 2 at a sampling rate of $\Delta t = 0.05\ sec$, recording a total of $15,000$ data points. For our purposes, the data were divided into seven realizations of $2,048$ points each. This number was used in order to utilize the FFT, which requires that the number of points input equals a power of 2 (in this case, 2^{11}). The complex Fourier coefficients associated with the data were calculated and a power spectrum computed and plotted. It was determined that only the lower 300 frequency components contained significant energy, so the number of frequency components to be modeled was reduced from $1,024$ (which resulted from the FFT) to 300, yielding a frequency range $0.0098\ Hz \leq f \leq 2.9297\ Hz$. As we will see later, this truncation has an impact in computing higher-order statistical properties.

The definition of the Fourier transform used in reducing the experimental data was not equal to that used in deriving any of the models. From the discrepancy of the definitions, it was determined that the data had to undergo the following transformation:

$$A_n = 2F_n^* \tag{4.19}$$

where F_n^* is the conjugate of the complex amplitude taken from the FFT used to process the time series of the experiment. This transformation was done before the data was input to the model. For the fully nonlinear extended Boussinesq model, the A_n was then transformed to B_n via Equation 4.1 before input. The model results (in the form of complex Fourier coefficients for A_n) were then transformed back into F_n, and the power spectra calculated.

The resulting comparisons are shown in Figures 4.16 through 4.19. At first glance, it appears that the fully nonlinear extended Boussinesq model compares relatively poorly to the data compared to the fully dispersive nonlinear shoaling model and (at times) the consistent shoaling model. Close inspection, however, reveals that this extended Boussinesq model actually predicts the peak frequency energy very well for most of the range of propagation. Not until $d = 10\ cm$ does the extended Boussinesq model show more deviation from the data at the peak frequency than the consistent shoaling model. However, at frequencies higher than the peak the deviation is significant, even at the first gage ($d = 35\ cm$). From our discussion of the previous section, it can be concluded that the probable cause of much of this overprediction is the poor performance of the linear shoaling mechanism of the fully nonlinear extended Boussinesq model in this frequency range. As the waves evolve and trade energy between frequencies, nonlinear effects make up a larger portion of this overprediction than at the start. The nonlinear

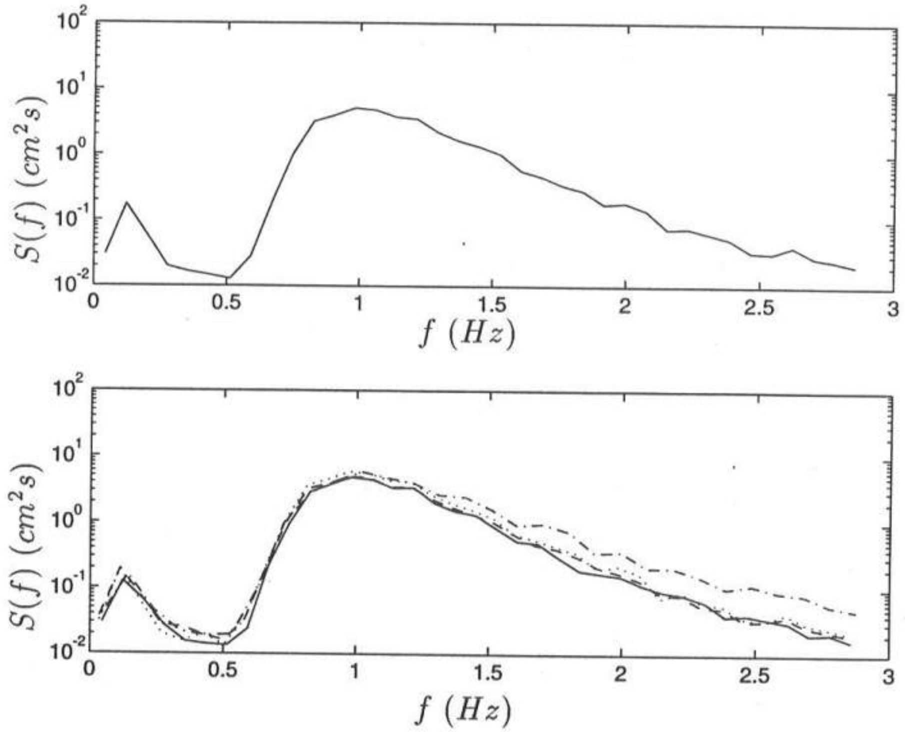

Figure 4.16: Comparison of Shoaling Models to Case 2 of Mase and Kirby (1992). Experimental Data (–), Fully Dispersive Shoaling Model (- -), Consistent Model of Freilich and Guza (1984) (. .), Fully Nonlinear Extended Boussinesq Frequency Domain Model (- .). (Top) Input Spectra at $d = 47\ cm$; (Bottom) $d = 35\ cm$.

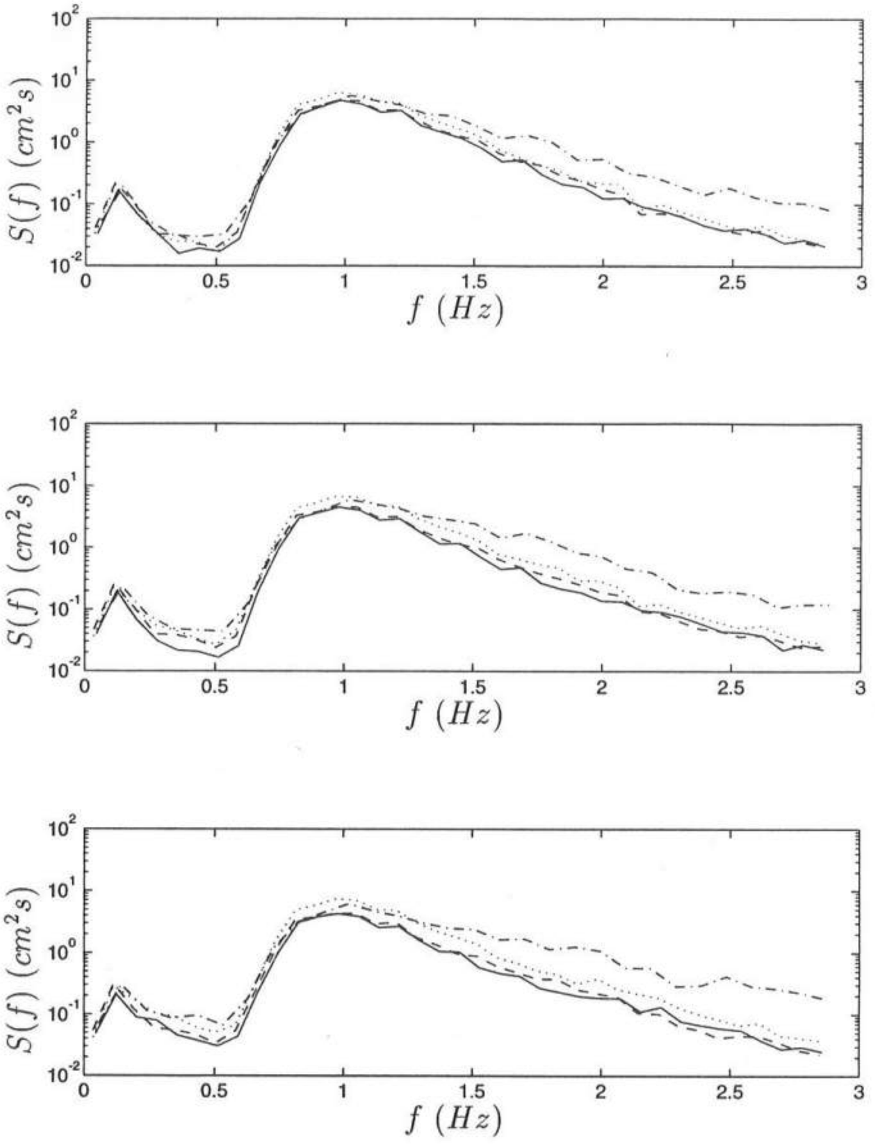

Figure 4.17: Comparison of Shoaling Models to Case 2 of Mase and Kirby (1992). Experimental Data (–), Fully Dispersive Shoaling Model (- -), Consistent Model of Freilich and Guza (1984) (. .), Fully Nonlinear Extended Boussinesq Frequency Domain Model (- .). (Top) $d = 30\ cm$; (Middle) $d = 25\ cm$; (Bottom) $d = 20\ cm$.

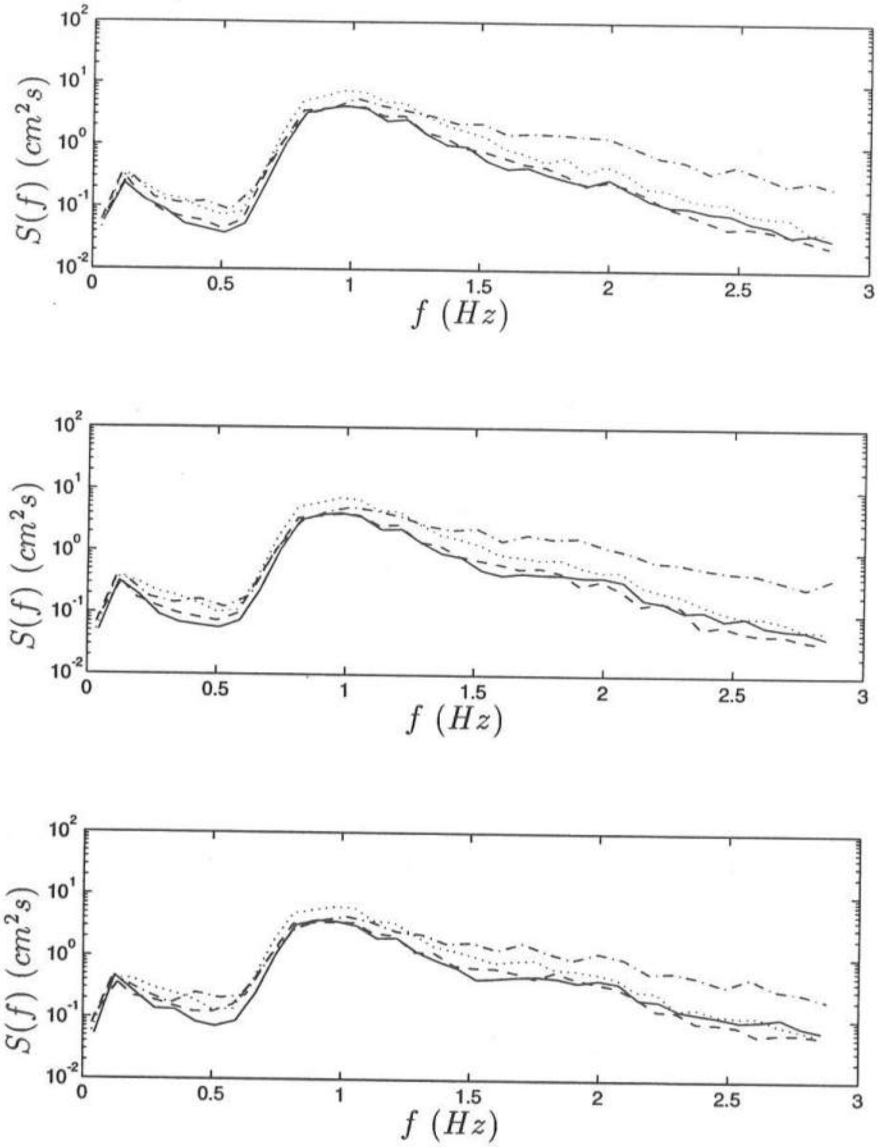

Figure 4.18: Comparison of Shoaling Models to Case 2 of Mase and Kirby (1992). Experimental Data (–), Fully Dispersive Shoaling Model (- -), Consistent Model of Freilich and Guza (1984) (. .), Fully Nonlinear Extended Boussinesq Frequency Domain Model (- .). (Top) $d = 17.5\ cm$; (Middle) $d = 15\ cm$; (Bottom) $d = 12.5\ cm$.

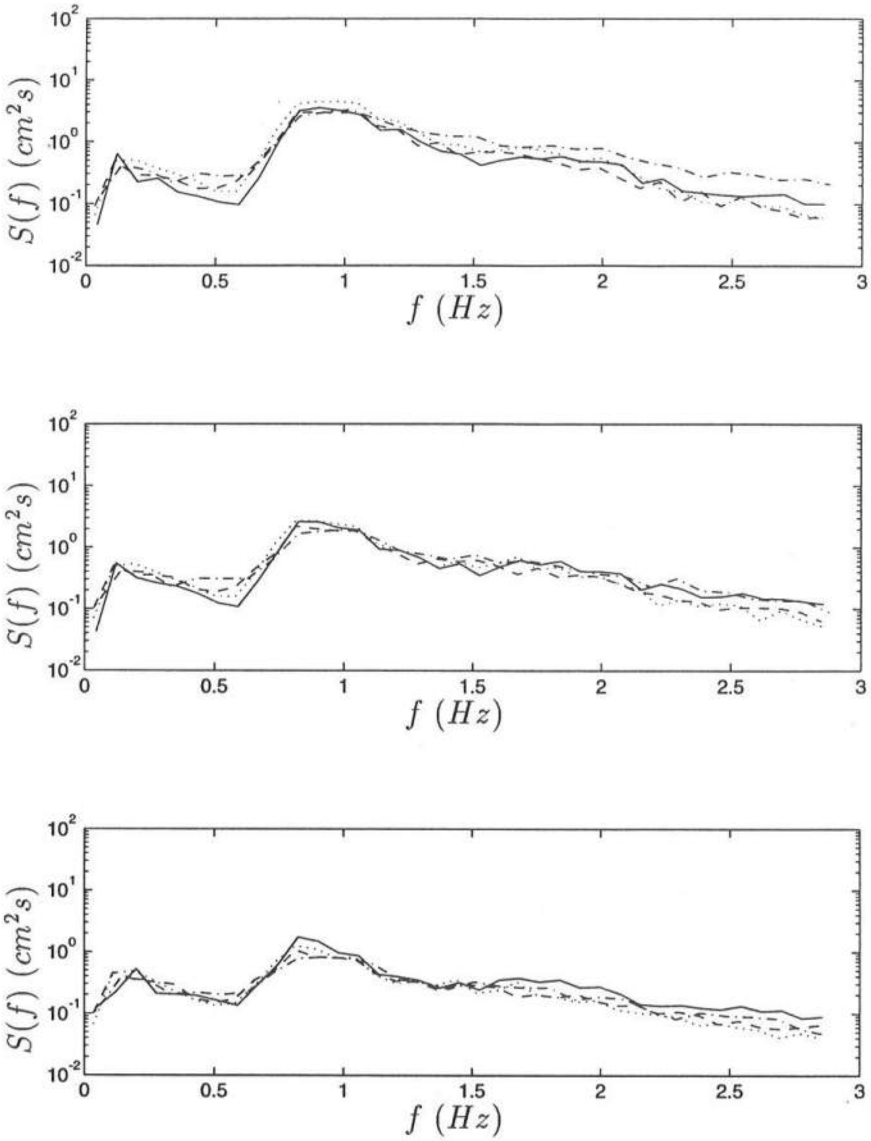

Figure 4.19: Comparison of Shoaling Models to Case 2 of Mase and Kirby (1992). Experimental Data (–), Fully Dispersive Shoaling Model (- -), Consistent Model of Freilich and Guza (1984) (. .), Fully Nonlinear Extended Boussinesq Frequency Domain Model (- .). (Top) $d = 10.0\ cm$; (Middle) $d = 7.5cm$; (Bottom) $d = 5\ cm$

coupling between the components may be suitably formulated, but is driven by the spectral amplitudes; thus erroneous predictions of amplitudes in the high frequency range affect the accuracy of the energy transfer. In contrast, the fully dispersive nonlinear shoaling model performs very well compared to the data. It simulates the high frequency end of the spectrum better than both the consistent model and the fully nonlinear extended Boussinesq model. The consistent model, on the other hand, begins to pull away from the peak at the first slope gage ($d = 35\ cm$), and then overpredicts most of the spectral range for the remainder of the propagation distance, at least until breaking becomes significant. At the final gage ($d = 5\ cm$) damping dominates all the models.

4.2.5 Root-Mean-Square Waveheight, Skewness and Asymmetry

While we have seen qualitative comparisons of spectra between our nonlinear shoaling models and data, we wish to establish a more quantitative comparison using statistical parameters taken from both the data and model output. The statistical properties in question are root-mean-square waveheight (or H_{rms}), skewness and asymmetry. Comparisons between data and model using H_{rms} will allow us to directly quantify the comparisons shown in Figures 4.16 through 4.19, since, in our definition, this is an energy-based parameter. Skewness (a measure of top-to-bottom asymmetry) and asymmetry (used, in this context, to mean front-to-back asymmetry) will help us determine whether our models are attaining the proper wave shape. In addition, we will also examine the implications of truncating the spectra at 300 components for model input. This will be done by direct comparisons of the statistical properties of the truncated spectra of the experimental data set at each gage to those of the full spectra (all components kept). We note here that skewness and asymmetry are relevant only to nonlinear waves; both quantities are identically zero for linear sinusoidal waves.

The quantity H_{rms} is calculated by Equation (4.9). Since it is a direct summation of the energy contained in each spectrum, it is a quantitative analogue of the comparisons shown in Figures 4.16 through 4.19. This quantity contains no information about the actual wave shape; skewness and asymmetry are required for this. Skewness is calculated by :

$$Skewness = \frac{\langle \eta^3 \rangle}{\langle \eta^2 \rangle^{\frac{3}{2}}} \tag{4.20}$$

where η is the signal (in our case, the water surface) and the brackets $\langle\rangle$ denote an average. Asymmetry is found by:

$$Asymmetry = \frac{\langle (\mathcal{H}(\eta))^3 \rangle}{\langle \eta^2 \rangle^{\frac{3}{2}}} \tag{4.21}$$

where $\mathcal{H}(\eta)$ denotes the Hilbert transform of the signal η.

For the ensuing comparisons, each of the seven realizations of the model output was "inverse FFT'd" to recover the time series. Then, H_{rms}, skewness and asymmetry were calculated from each time series and averaged over all seven realizations, with the standard deviation also calculated. This was done for each gage. The experimental data at each gage were processed as discussed in Section 4.2.4, and then "inverse FFT'd" to obtain a time series based on only the first 300 frequency components. Again H_{rms}, skewness and asymmetry were computed, and then averaged over the seven realizations, taking note of the standard deviation. To ascertain the effect of this truncation, the full 1,024 component spectrum for each realization was processed similarly, and the same statistical parameters were calculated and averaged.

Figures 4.20 through 4.23 show the results for H_{rms}. Figure 4.20 shows the average H_{rms} variation through the shoaling and breaking region of the experimental data for both the truncated and full spectra. Also shown is the result

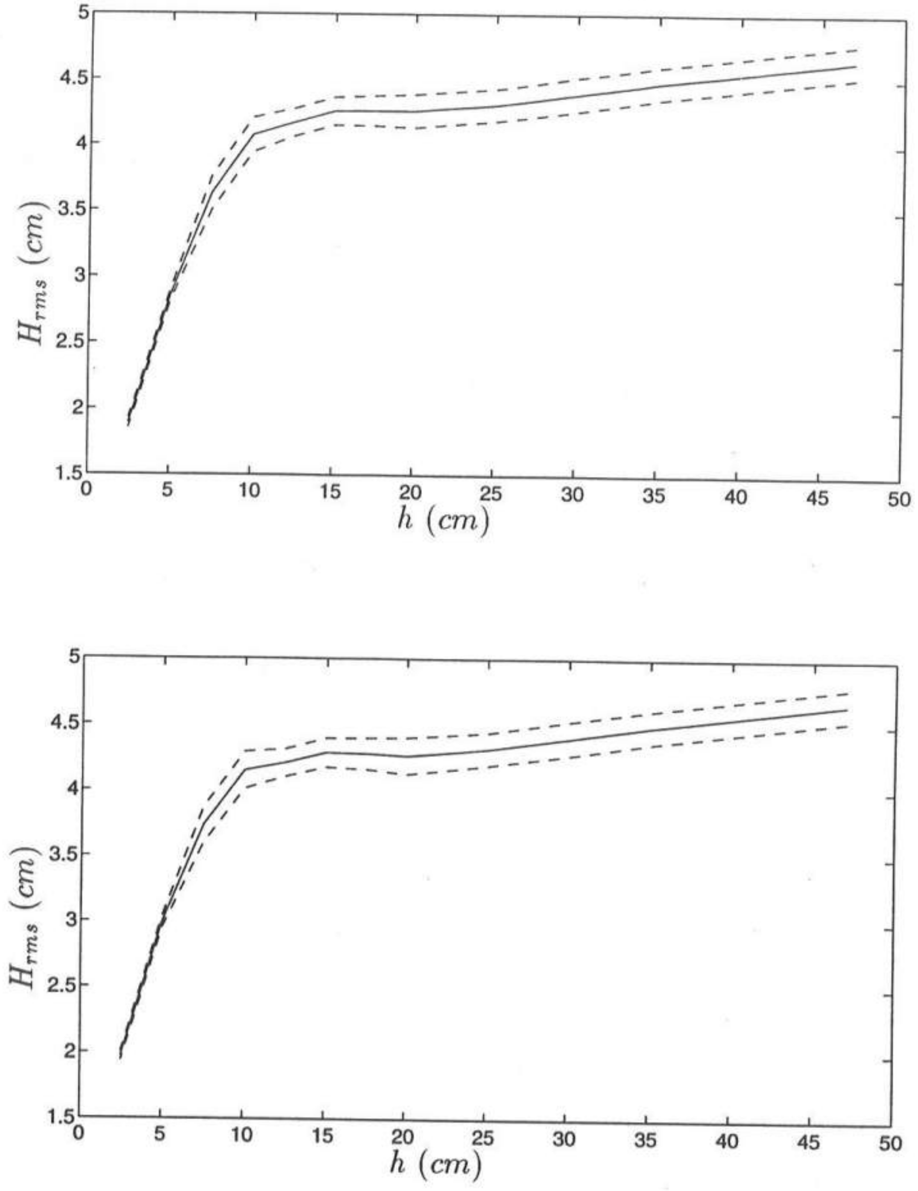

Figure 4.20: Variation of H_{rms} of Experimental Data of Mase and Kirby (1992) with Depth. H_{rms} Averaged Over Seven Realizations (–), Average H_{rms} with One Standard Deviation Added or Subtracted (- -). (Top) Data Truncated At 300 Components; (Bottom) Full Spectrum.

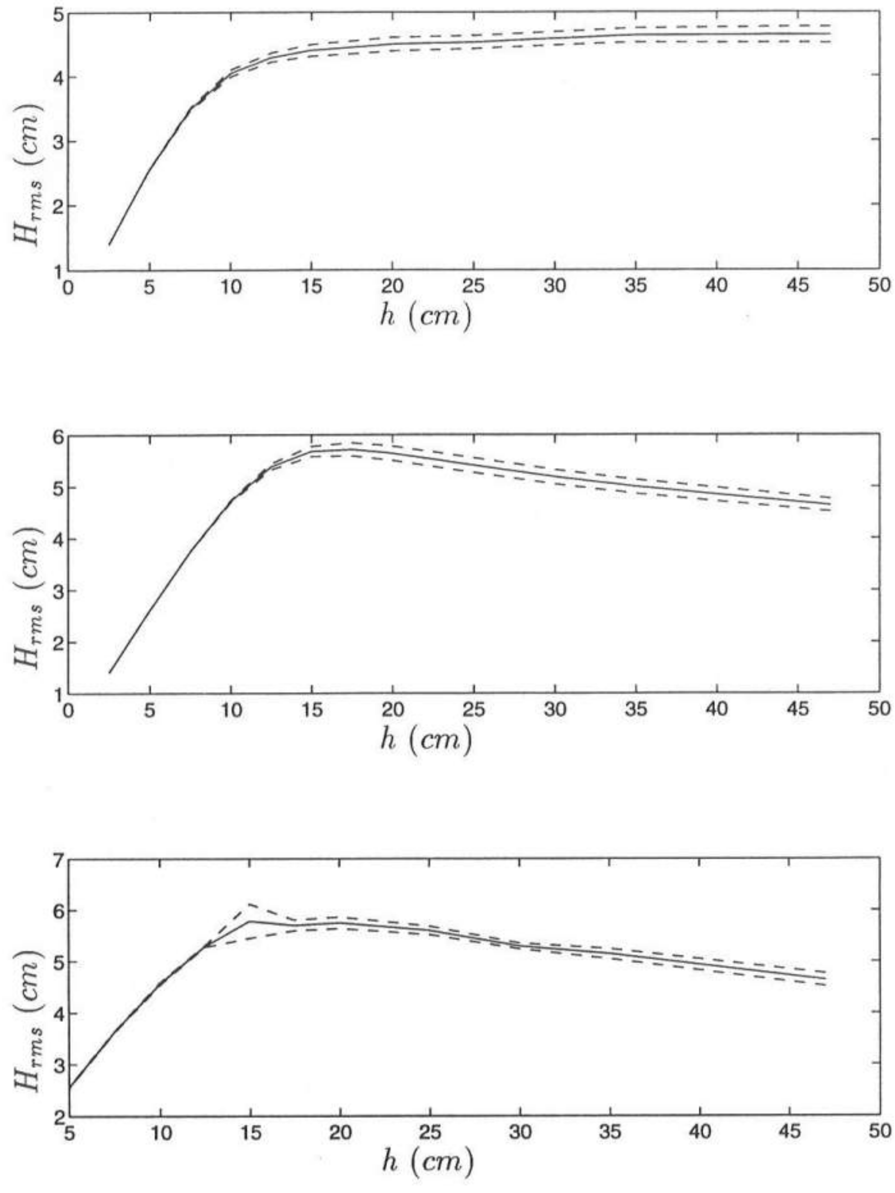

Figure 4.21: Variation of H_{rms} of Model Result with Depth. H_{rms} Averaged Over Seven Realizations (–), Average H_{rms} with One Standard Deviation Added or Subtracted (- -). (Top) Fully Dispersive Nonlinear Shoaling Model; (Middle) Consistent Shoaling Model of Freilich and Guza (1984); (Bottom) Fully Nonlinear Extended Boussinesq Model

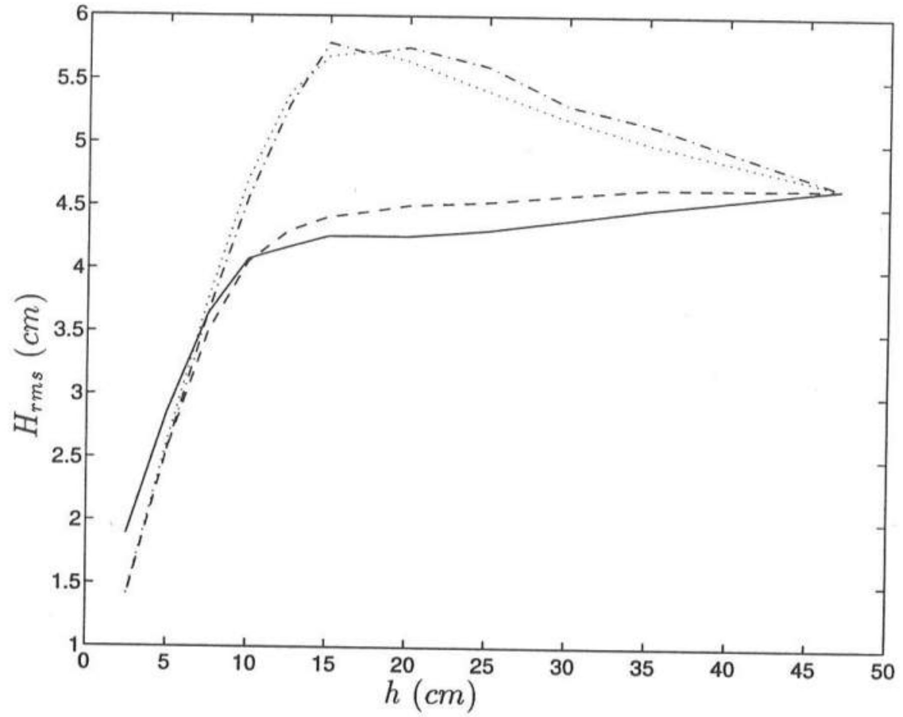

Figure 4.22: Comparison of Average H_{rms}. Experimental Data of Mase and Kirby (1992) Truncated at 300 Components (-); Fully Dispersive Nonlinear Shoaling Model (- -); Consistent Shoaling Model of Freilich and Guza (1984) (. .); Fully Nonlinear Extended Boussinesq Model (- . -)

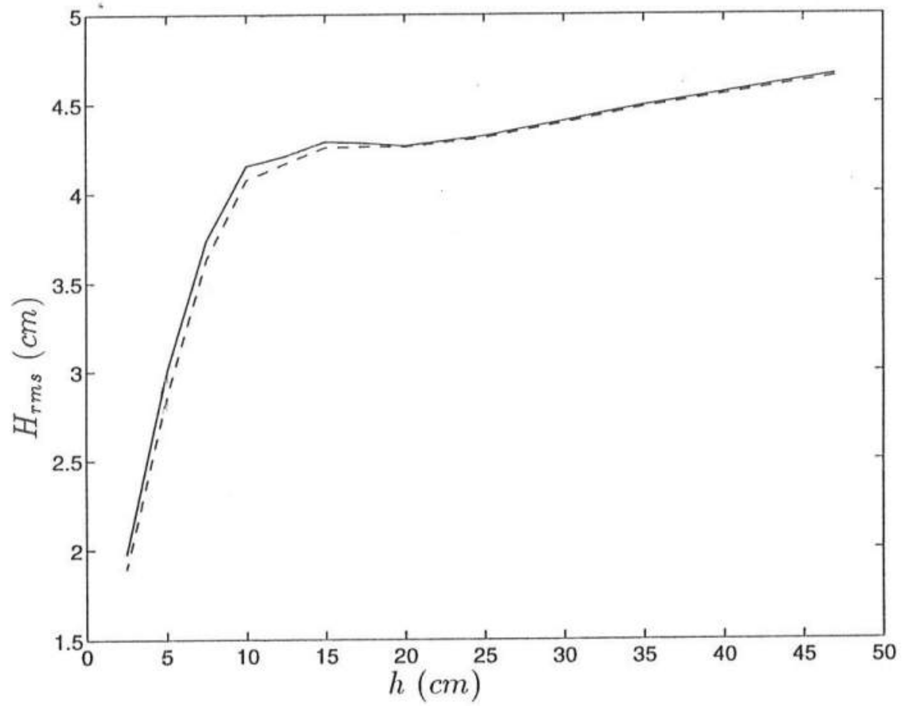

Figure 4.23: Effect of Truncation of Experimental Data of Mase and Kirby (1992) on H_{rms} Variation. Full Spectra (–); Spectra Truncated at 300 Components (- -)

after one standard deviation is added and subtracted from the average. It is apparent that the standard deviations become smaller as the wave train dissipates. This shows that the breaking process acts like a wave height "filter," gradually eliminating the randomness in the wave heights that caused H_{rms} to vary between realizations. This trend is also reflected in the results from all three models. Figure 4.22 shows comparisons of average H_{rms} between the different models and the truncated data. It is apparent that the fully dispersive model performs better than both the consistent model of Freilich and Guza (1984) (Equation 2.59) and the fully nonlinear extended Boussinesq model. Figure 4.23 compares the average H_{rms} values between the truncated experimental spectra and the full spectra throughout the shoaling and breaking region. The close comparison shows that truncation of the spectrum to 300 components does not result in loss of a significant amount of energy.

It is to be noted that the effects of the overprediction of linear shoaling in the fully nonlinear extended Boussinesq model are still present in these simulations. They are not as prevalent in the results due to the dissipation term, which essentially damps energy in proportion to the total energy content. If the higher frequencies were overshoaled, and the energy content overpredicted, the damping would be stronger than it would be if the energy content of the higher frequencies were accurately modeled. Thus, the favorable comparison of the H_{rms} values of the fully nonlinear extended Boussinesq models to those of the consistent model of Freilich and Guza (1984) is misleading, since the dissipation in the former model is probably higher than is present in either the experimental data or the latter model.

The next set of data-model comparisons concerns the skewness parameter. As mentioned before, skewness is a measure of top-to-bottom asymmetry. In the

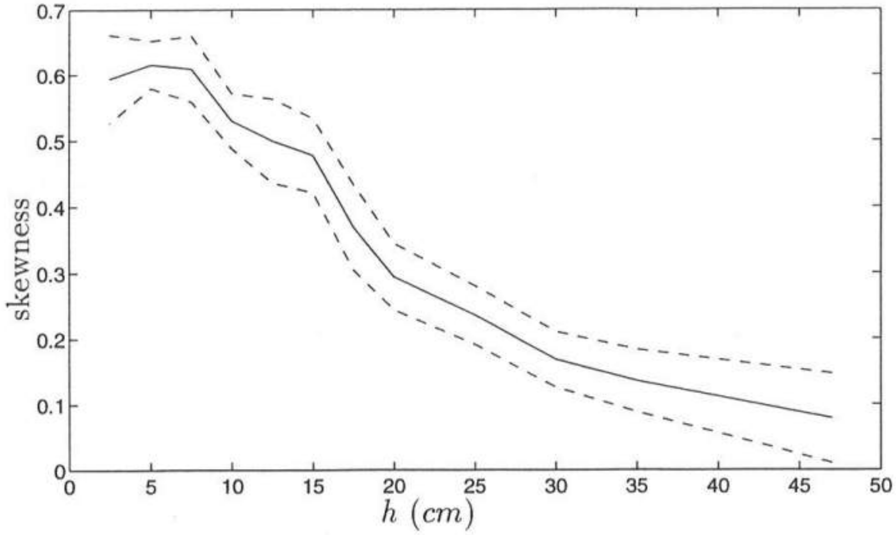

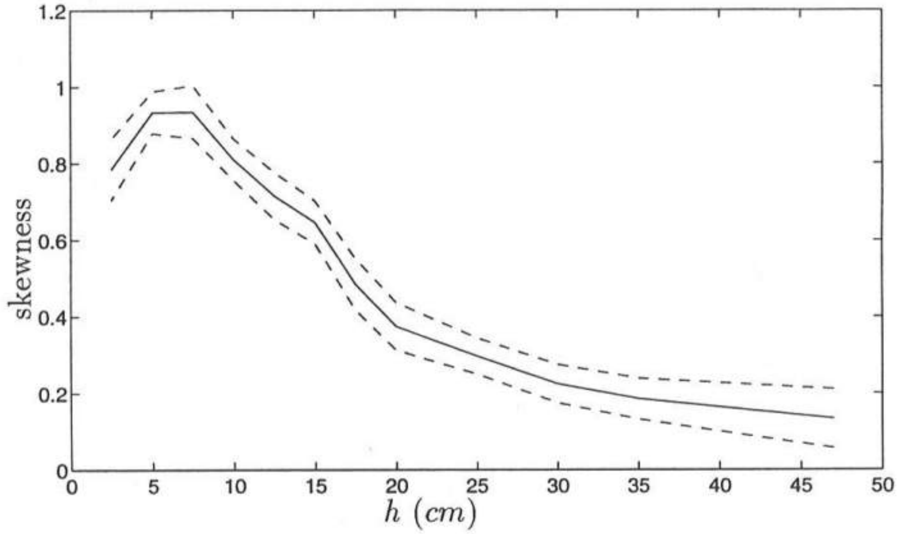

Figure 4.24: Variation of Skewness of Experimental Data of Mase and Kirby (1992) with Depth. Skewness Averaged Over Seven Realizations (–), Average Skewness with One Standard Deviation Added or Subtracted (- -). (Top) Data Truncated At 300 Components; (Bottom) Full Spectrum.

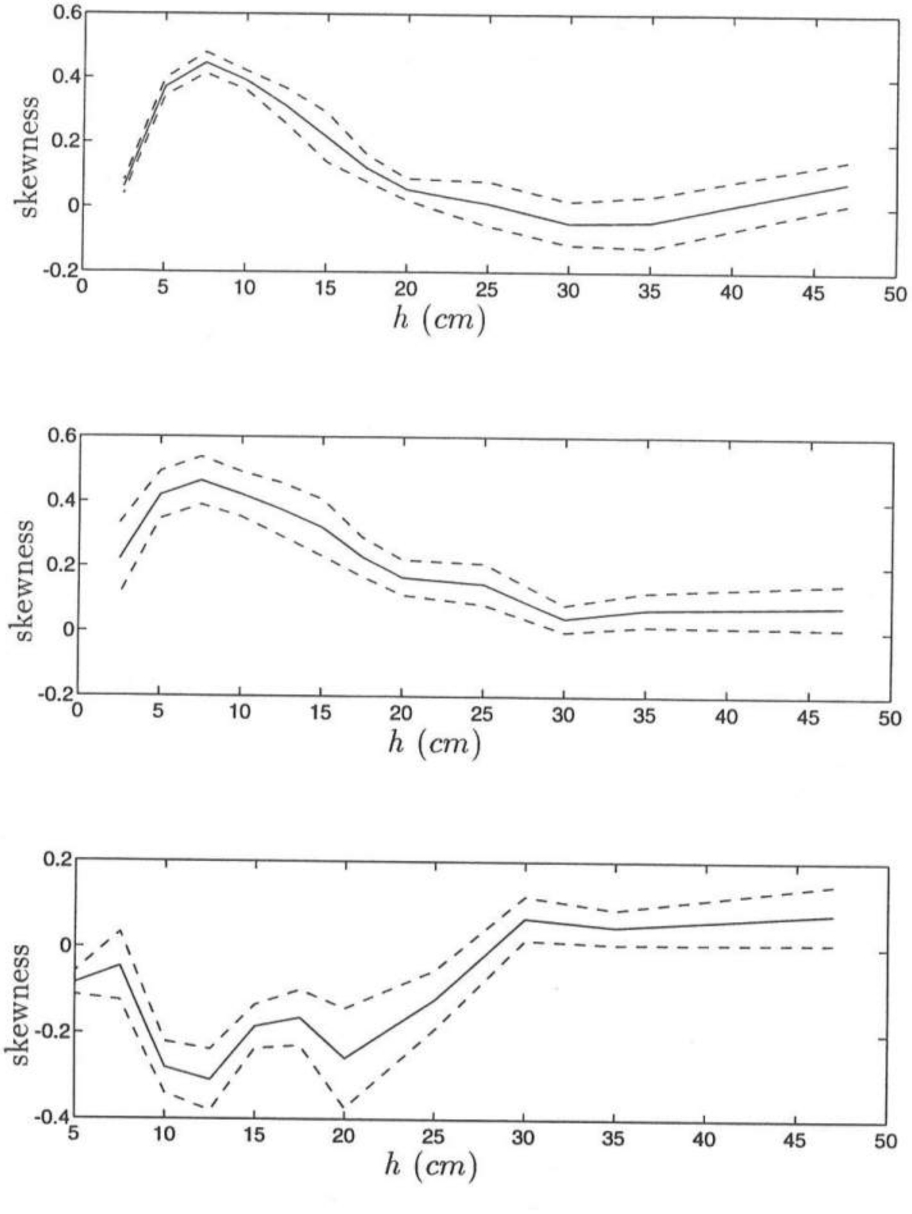

Figure 4.25: Variation of Skewness of Model Result with Depth. Skewness Averaged Over Seven Realizations (–), Average Skewness with One Standard Deviation Added or Subtracted (- -). (Top) Fully Dispersive Nonlinear Shoaling Model; (Middle) Consistent Shoaling Model of Freilich and Guza (1984); (Bottom) Fully Nonlinear Extended Boussinesq Model

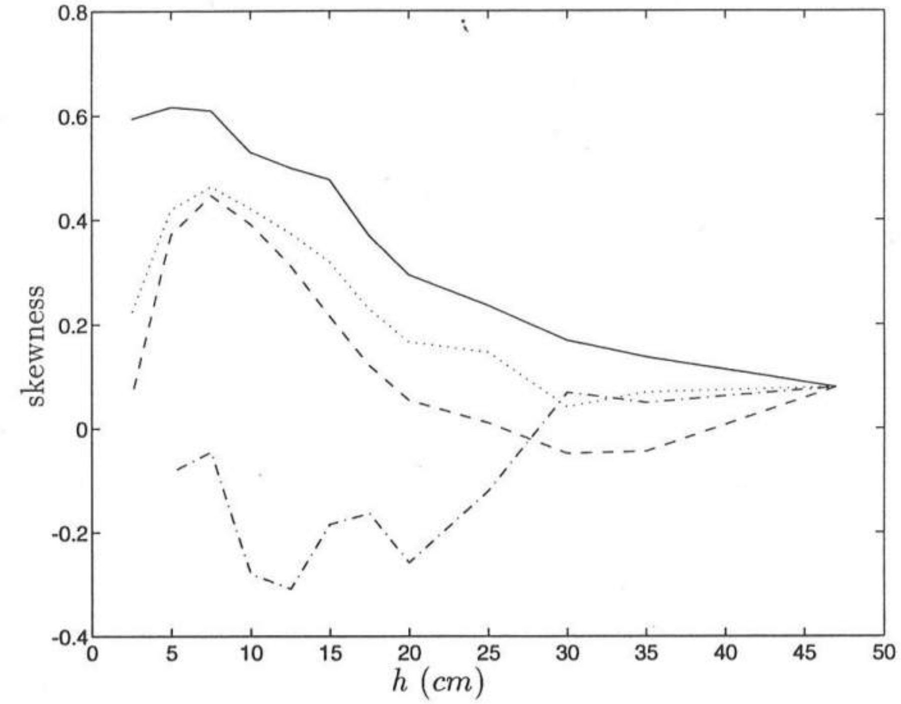

Figure 4.26: Comparison of Average Skewness. Experimental Data of Mase and Kirby (1992) Truncated at 300 Components (–); Fully Dispersive Nonlinear Shoaling Model (- -); Consistent Shoaling Model of Freilich and Guza (1984) (. .); Fully Nonlinear Extended Boussinesq Model (- .)

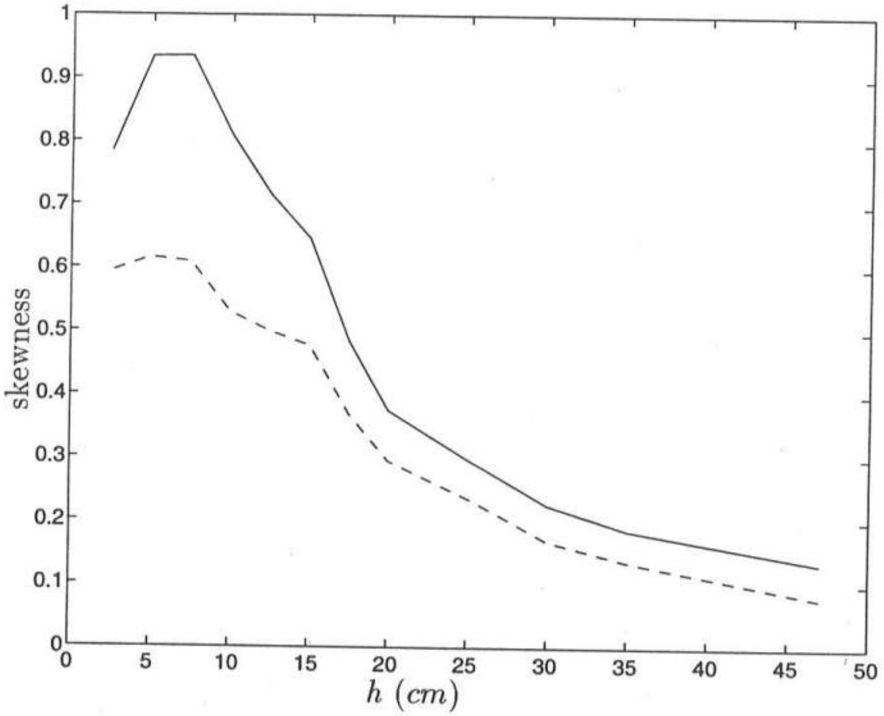

Figure 4.27: Effect of Truncation of Experimental Data of Mase and Kirby (1992) on Skewness Variation. Full Spectra (–); Spectra Truncated at 300 Components (- -)

context of water waves, this is actually a measure of nonlinearity; both Stokes and cnoidal waves have sharper crests and flatter troughs than linear waves, and thus nonzero skewness. Figure 4.24 depicts the variation of skewness with water depth for the truncated and full experimental spectra. Unlike H_{rms}, there seems to be no narrowing of the standard deviation band. This may be because skewness is a less stable statistical parameter than H_{rms}, reliant on the actual shape of the signal rather than just its energy content. Figure 4.25 shows the skewness variations with water depths for the various models under study. Except for some possibly coincidental narrowing of the standard deviation band in the fully dispersive nonlinear shoaling model, this band tends to stay fairly wide. Figure 4.26 compares the average skewness of our shoaling models with the data. While the fully dispersive and consistent shoaling models at least have the correct trend (with the consistent model comparing the better of the two), the fully nonlinear extended Boussinesq model performs quite poorly in comparison. The strong negative trend in this skewness prediction indicates that the waves have flat crests and sharp troughs, unrealizable for a typical gravity wave free of surface tension effects. It can be concluded that the overpredicted high frequency components are affecting the wave shape predictions to a great degree. This strong negative skewness may also be a function of the spectral truncation. The artifical amplification of the energy content of the high frequency components by a shoaling mechanism operating well outside the linear dispersion relation calibration range would seem to affect the nonlinear energy transfer, as stated earlier. It may be that these frequency components would interact strongly with components which have been truncated and are not present in the simulation. This may have a deleterious effect on the prediction of skewness as well. The possible effect of truncation on resonant interaction is explained more completely later in this section. Figure 4.27 compares the skewness between the truncated and full data spectra. It is evident that the skewness of the truncated spectra is much lower than that of the full spectra. This is in concert with the findings of Bowen (1994), who maintained that the calculation of higher order moments like skewness is affected by truncation. This effect is usually manifested by a lower skewness value for the truncated spectra than would be given by the full spectra. In fact, Bowen (1994) showed plots of measured skewness, in which incrementally increasing numbers of harmonics of the peak frequency were kept, and the skewness calculated, until the full spectrum was retained. He found that the skewness values for these data converged on the values for the full spectrum as more harmonics were kept.

The final comparison addresses asymmetry, here meant as front-to-back asymmetry. We would expect the asymmetry of breaking waves to be negative, as this reflects their sawtooth-like shape. Figure 4.28 shows the asymmetry for the truncated and full experimental spectra. Again, as with the skewness, the standard deviation band for the asymmetry is fairly wide, and remains so through the domain. This is evidence of its statistical variability, as was also shown with the skewness predictions. Figure 4.29 depicts the average asymmetry for the three models. All show evidence of the effects of dissipation, as they all exhibit negative asymmetry by the time the last gage is reached, albeit to varying degrees. Figure 4.30 compares the average asymmetry of the three models against that of the truncated spectra. Of the three models, the consistent model of Freilich and Guza (1984) compares the best against the data, although no model performs particularly well. Figure 4.31 compares asymmetry values between the truncated experimental spectra and the full spectra. Again, as with skewness, truncation of the experimental spectra to 300 components tends to reduce the asymmetry (in this case, the *negativeness* of asymmetry). This is also in accord with the findings of Bowen (1994), who calculated varying degrees of asymmetry based on keeping more harmonics of the spectral peak of his laboratory data. He found that, as

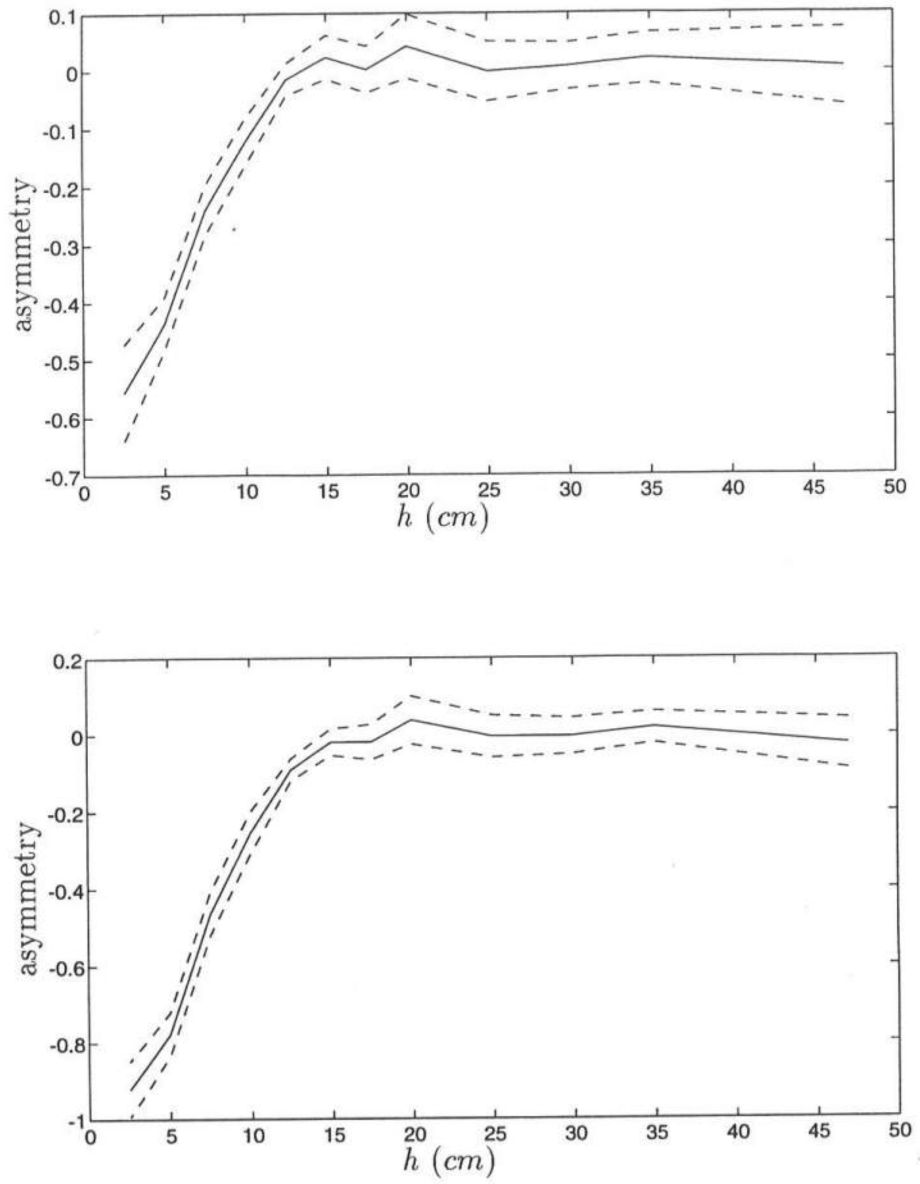

Figure 4.28: Variation of Asymmetry of Experimental Data of Mase and Kirby (1992) with Depth. Asymmetry Averaged Over Seven Realizations (–), Average Asymmetry with One Standard Deviation Added or Subtracted (- -). (Top) Data Truncated At 300 Components; (Bottom) Full Spectrum.

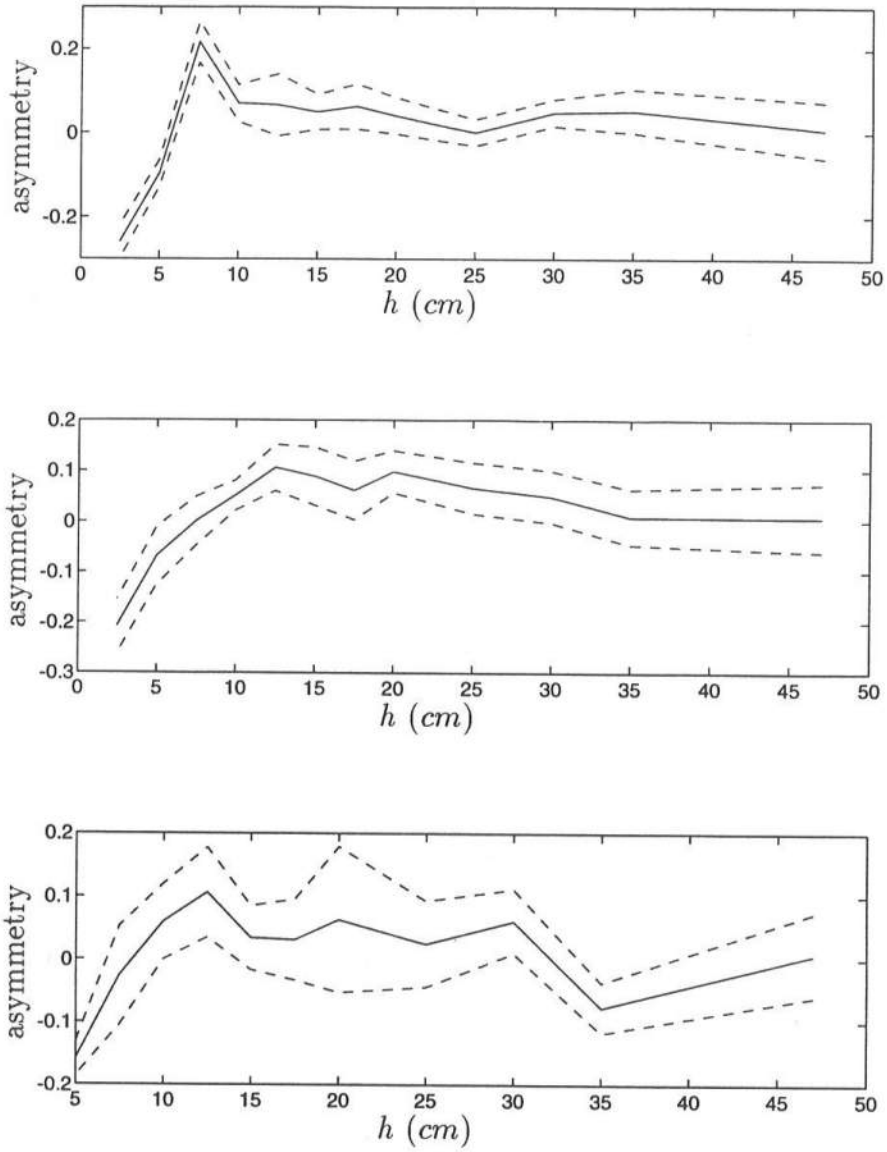

Figure 4.29: Variation of Asymmetry of Model Result with Depth. Asymmetry Averaged Over Seven Realizations (–), Average Asymmetry with One Standard Deviation Added or Subtracted (- -). (Top) Fully Dispersive Nonlinear Shoaling Model; (Middle) Consistent Shoaling Model of Freilich and Guza (1984); (Bottom) Fully Nonlinear Extended Boussinesq Model

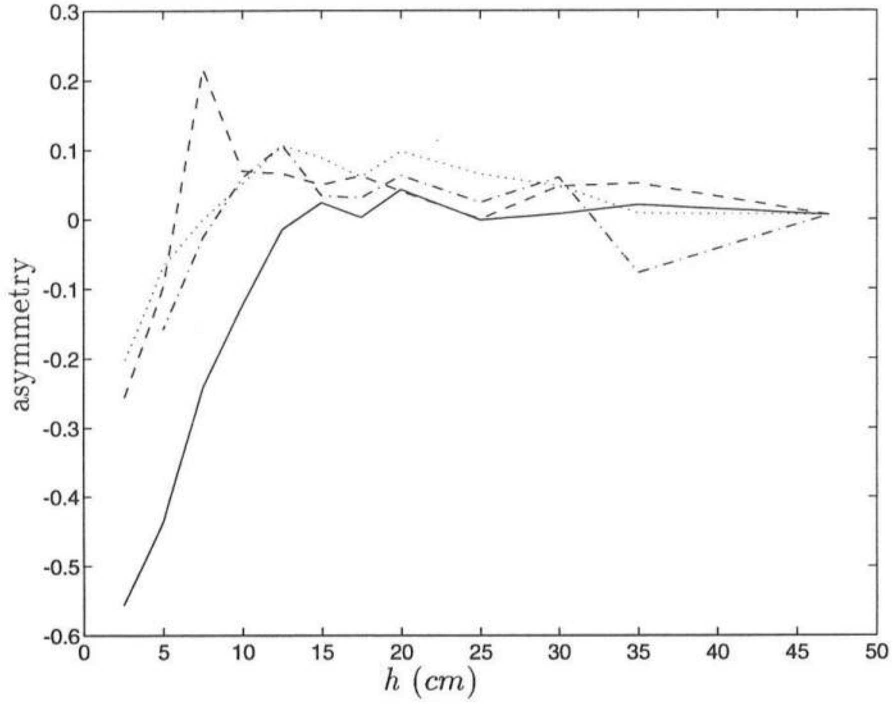

Figure 4.30: Comparison of Average Asymmetry. Experimental Data of Mase and Kirby (1992) Truncated at 300 Components (–); Fully Dispersive Nonlinear Shoaling Model (- -); Consistent Shoaling Model of Freilich and Guza (1984) (. .); Fully Nonlinear Extended Boussinesq Model (- .)

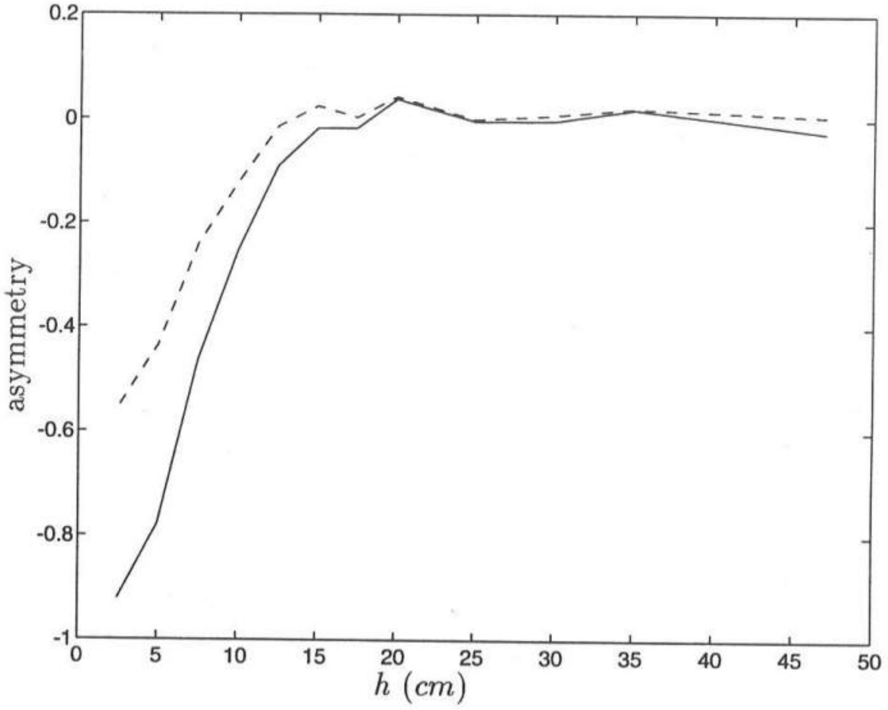

Figure 4.31: Effect of Truncation of Experimental Data of Mase and Kirby (1992) on Asymmetry Variation. Full Spectra (–); Spectra Truncated at 300 Components (- -)

with skewness, the asymmetry values converged upon the asymmetry of the entire spectra (all components kept) as more harmonics of the peak were retained.

It is noted here that strict comparisons of model skewness and asymmetry to data, even the truncated spectra, are misleading. Each component of the data has experienced all possible resonant interactions with every other component; it is the result of these processes that is truncated. In contrast, the models only "see" the truncated spectra as input; thus interactions only take place within the frequency range of these truncated spectra, neglecting all interactions outside this range. While this does not seem to have an effect on lower-order quantities such as H_{rms}, it may have an influence on the higher-order moments such as skewness and asymmetry. It would seem that the only true comparisons of higher-order moments between model and data would be achieved if *all* frequency components of the experimental data were retained, which is possibly prohibitively expensive in terms of required computing time.

Despite the qualifications listed above, we can make some general conclusions concerning the abilities of the models to simulate various statistical quantities associated with the energy level and shape of the wavefield. Figure 4.22 shows that the fully dispersive shoaling model performs better than either the consistent model of Freilich and Guza (1984) or the fully nonlinear extended Boussinesq model in predicting H_{rms}. This is reflective of accuracy in modeling the energy content of the spectral wavefield, and is a quantification of this model's performance in the direct spectra-to-spectra comparisons shown in Figures 4.16 through 4.19. However, in modeling higher-order moments, the consistent model of Freilich and Guza (1984) arguably yields the best comparisons to the data, both in skewness and asymmetry. It may be asserted, however, that none of the three models compares exceptionally well to the skewness and asymmetry values of the truncated experimental spectra. Additionally, we have also determined that truncating the experimental spectra and then calculating higher-order moments tends to lead to underpredictions of skewness and negative asymmetry than if the entire spectra were used. This is in line with the results of Bowen (1994).

4.3 Summary

In this chapter we have shown comparisons of both our parabolic models and our one-dimensional shoaling models (developed in Chapters 2 and 3) to data. Our first comparison was to the experiment of Whalin (1971). We demonstrated that our parabolic two-dimensional models of both the nonlinear mild-slope equation (Equation 2.55) and and the fully nonlinear extended Boussinesq equations (Equations 3.35 and 3.36) compared better to the data than the parabolic KP model of Liu et al. (1985) (Equation 2.56) for the $T = 2$ s wave case. Additonally, we also demonstrated the effects of retaining $O(\delta\mu^2)$ terms in the fully nonlinear extended Boussinesq model by comparing it to the model of Chen and Liu (1993), which does not contain these terms. It was shown that the fully nonlinear extended Boussinesq model compares better than the model of Chen and Liu (1993) for the higher harmonics of the $T = 2$ s case. This is due to the retention of dispersive effects in the nonlinear terms, the neglect of which causes the model to overshoal when nonlinear effects become important. For the $T = 3$ s case, all models, including the parabolic KP model, perform equally well. All models evidence the overprediction of the first harmonic amplitudes that seem to be prevalent among all studies that use this data set for comparison.

Before we compared our one-dimensional shoaling models to the data of Mase and Kirby (1992) we digressed briefly to discuss two aspects of the comparison that affected the models. The first was energy dissipation. We wrote our one-dimensional shoaling models with a damping term added, and derived the energy flux relation, stating that the evolution of the energy flux is a function of dissipation. We then used the dissipation model of Thornton and Guza (1983) as our probabilistic dissipation function, and postulated a frequency distribution function that combines an equal energy drain across all frequencies with a mechanism that attempts to incorporate the f^2 dependence evident in the data of Mase and Kirby (1992). Based on tests with the consistent model of Freilich and Guza (1984), we found that an equal mixture of the two mechanisms worked well for this data. We also analyzed the linear shoaling tendencies that the consistent model of Freilich and Guza (1984) and the fully nonlinear extended Boussinesq model would have relative to the frequency range in this data set. We chose ten representative frequencies that spanned most of the frequency range of the data, defined a percent error between the shoaling coefficient found by either of these two models against that of linear theory, and showed surface plots of these errors (Figures 4.12 and 4.13). It was shown that the linear shoaling characteristics of the fully nonlinear extended Boussinesq model worked better than Green's Law for the frequency range lower than the peak frequency, which was in intermediate water depth. The errors between this model and linear theory were much lower than the corresponding errors with Green's Law in this range. On the higher frequency side of the peak, however, Green's Law seemed to perform better relative to linear theory. This was not because Green's Law has any validity as a predictor of linear shoaling tendencies in this range, but because the shoaling errors climbed quickly and leveled off as the frequency increased. In contrast, the error surface for the linear shoaling characteristics of the fully nonlinear extended Boussinesq model was fairly level until the peak frequency, and then exhibited an almost-exponential increase. Based on this analysis, we expected that the main source of discrepancy between data and either the consistent shoaling model or the fully nonlinear extended Boussinesq model is the partial inapplicability of these models for the range of frequencies and water depths of the experiment.

This assertion was borne out in the direct data-to-model comparisons shown in Figures 4.16 through 4.19. The fully dispersive nonlinear shoaling model, with full linear theory in its linear shoaling mechanism, performed the best of the three models in predicting the energy content and spectral shape. The consistent model, on the other hand, began to pull away from the peak of the data at the first inshore gage ($d = 35\ cm$), and overpredicted the higher frequency range of the data. The fully nonlinear extended Boussinesq model, as expected, exhibited better comparison to the data than the consistent shoaling model for frequencies lower than and equal to the peak frequency, and dramatically overpredicted the energy content in the frequency components higher than the peak compared to either the fully-dispersive nonlinear shoaling model or the consistent shoaling model of Freilich and Guza (1984), in accord with the error analysis described earlier.

We then looked at root-mean-square waveheight (or H_{rms}), skewness and asymmetry. The effect of truncation of the experimental spectra to 300 components was also investigated, as Bowen (1994) maintained that this truncation has an effect on the prediction of skewness and asymmetry. We saw that the comparisons of H_{rms} to data quantified what the direct model-to-data spectra comparisons showed: that the fully dispersive nonlinear shoaling model predicted the overall energy content better than the other two models. We also showed that truncation of the spectra to 300 components incurs no significant energy loss, as the H_{rms} values for both the truncated experimental spectra and the full spectra compare closely at each gage. Skewness comparisons were also shown. It was observed that all three models underpredicted the skewness of the truncated spectra, with the consistent model of Freilich and Guza (1984) yielding the best prediction of skewness among the three models. Additionally, the skewness of the fully nonlinear extended Boussinesq model remained strongly negative for most of the domain, indicating that the waves have sharp troughs and flat crests, which is not endemic of a typical gravity wave. We postulated that this can be explained by the artificially-amplified higher frequency components and the effect of truncation of the spectra. The overshoaled high frequency components adversely affected the prediction of wave shape and the top-to-bottom asymmetry (which is quantified by skewness). Nonlinear energy transfer would seem to have been exacerbated by these overshoaled components; however, since the spectra were truncated at 300 components, the artificially strong energy transfers that would have taken place in a full spectrum could not take place here. This may also have had an effect on the skewness results from the fully nonlinear extended Boussinesq model. We also showed that skewness calculated from a truncated spectrum could be much lower than that from the full spectrum, even though only an insignificant amount of variance is lost with the truncation. This is in agreement with Bowen (1994). Asymmetry was also calculated in an effort to quantify the effect of dissipation on the wave shape. A sawtooth-like wave shape, typical of breaking waves, would carry a negative asymmetry. It was made evident that neither model predicted asymmetry particularly well when compared to the asymmetry values of the truncated experimental spectra. We also showed that truncation of the spectra tends to underpredict the negativeness of the asymmetry as compared with retaining all components. We remarked that direct comparisons of skewness and asymmetry between data and model may not be altogether valid, even compared to the truncated spectra. The truncated data has undergone resonant interactions with all components throughout the entire spectrum. On the other hand, the models only "see" a number of components smaller than that of the entire spectrum, and thus can only interact in that frequency range.

Looking at overall model performance, it appears that the nonlinear mild-slope equation and its one-dimensional counterpart, the fully-dispersive nonlinear shoaling model, perform the best on average of the models tested with the experimental data used. It compares reasonably well in the parabolic two-dimensional form with the data of Whalin (1971), and very well in one dimension against the data of Mase and Kirby (1992). On the other hand, the fully nonlinear extended Boussinesq model does very well against the data of Whalin (1971), but relatively poorly against the data of Mase and Kirby (1992) for frequency ranges beyond the peak. This apparent dichotomy may be explained by examining the processes involved. In the case of Whalin (1971), the primary waves are in intermediate or shallow water depth, the higher harmonics start from zero, and we are modeling waves in two dimensions, which may serve to mitigate any strong overshoaling tendencies. However, in Mase and Kirby (1992), more than half the frequency range is in deep water. Additionally, the energy content in this frequency range is not insignificant. Thus it seems that the fully nonlinear extended Boussinesq model does very well compared to the fully dispersive nonlinear shoaling model for $\frac{h}{L_0} \leq 0.3$ (i.e., the frequency peak), but becomes problematic beyond that range. This may be due to the fact that the dispersion relation is of rational polynomial form, causing the linear shoaling terms to be ratios of rational polynomials if the explicit expression for the wavenumber k (Equation 3.13) is substituted in. This form may lead to poor performance outside the range of calibration for the dispersion parameter α. We thus state that the fully nonlinear extended Boussinesq model does well for situations in which all the frequency components satisfied $\frac{h}{L_0} \leq 0.3$. This is clearly not the case for the data of Mase and Kirby (1992), and so the comparisons may not be entirely appropriate.

Though the nonlinear mild-slope equation performs well for a wide range of water depths, it does not have a convenient time-dependent form, since the model coefficients are all functions of frequency and wavenumber. Additionally, one cannot make use of the "carrier frequency" concept of subdividing an incident spectrum into several components about some frequency, as is often done for time-dependent mild-slope equations (e.g., Kirby et al. 1992b), since all interactions need to occur. The fully nonlinear extended Boussinesq equations, on the other hand, do not have coefficients that are functions of wave number or wave frequency, and as such can be modeled in the time domain fairly conveniently. We are interested in this time-domain-to-frequency-domain correspondence, though we realize that this correspondence may be limited, as discussed in Section 3.5. Using the time-domain model, the wave field can be modeled without regard as to the exact nature of the process (shoaling, refraction, etc.) involved. Using the corresponding frequency-domain model, we can analyze each separate process and determine its relative importance. Thus, at this point, realizing the somewhat restrictive nature of the frequency-domain fully nonlinear extended Boussinesq model, we take this model into the angular spectrum domain. This will be shown in the next chapter.

Chapter 5

ANGULAR SPECTRUM MODELING OF EXTENDED BOUSSINESQ EQUATIONS

5.1 Introduction

So far in this study we have demonstrated the utility of dispersive nonlinear wave propagation models in spectral wave field evolution. We saw how the improved dispersive properties inherent in these models can potentially increase their applicability to situations involving deeper water than the range of validity for the standard Boussinesq equations. However, the suitability of one-dimensional and parabolic two-dimensional models for open coastal problems is obviously limited to the case of zero-to-small angle of wave approach.

Angular spectrum modeling is one method for overcoming the limitation of small wave approach angles without the computational restrictions of solving the full elliptic problem. The parabolic frequency domain approach decomposed the wavefield into a series of frequency components, where the problem still required solution in two space variables. The angular spectrum approach, on the other hand, decomposes the wave field into both frequency and longshore wave number components, thus permitting solutions to be found in terms of only one space variable. This approach essentially reduces the problem to the solution of a stacked framework of ordinary differential equations. This approach has been applied to the linear mild-slope equation (Dalrymple and Kirby 1988; Dalrymple et al. 1989) and to the standard Boussinesq equations (1.5) (Kirby 1990). We will emulate the approach of Kirby (1990) for the angular spectrum transformation of the fully nonlinear extended Boussinesq model. Kirby's development assumed a bathymetry with no variation in y; our development shares this limitation. We choose this model over the nonlinear mild-slope equation since it has a convenient time-domain form where the coefficients are not functions of frequency or wave number. This advantage allows us to view the fully nonlinear extended Boussinesq models as a system: the time-dependent form can predict the wave field without regard as to the nature of the individual components comprising it, and the angular spectrum model can explicitly isolate each relevant mechanism (refraction, shoaling, and nonlinear interaction) for further analysis.

5.2 Simplified Extended Boussinesq Angular Spectrum Model

As noted previously, a primary advantage of the extended formulation of the Boussinesq equation is the improved dispersion characteristics in deeper water than is valid for the standard Boussinesq equations. We saw that the shoaling mechanism behaves poorly in extremely deep water, but when begun in intermediate water depth ($\frac{h}{L_0} \approx 0.3$) the shoaling behavior improves and more closely approaches linear shoaling. The calculations involved in developing an angular spectrum model are straightforward but tedious. It would thus be instructive to investigate what effect improved dispersion would have on an existing shallow water wave model.

We begin from the standard Boussinesq equations of Peregrine (1967) (Equations 1.5), and assume periodicity in both time and longshore (y) direction. We thus decompose the representation of the free surface elevation η into N

frequency and $2M+1$ longshore wave number components:

$$\eta = \sum_{m=-M}^{M} \sum_{n=1}^{N} \frac{A_n^m(x)}{2} e^{i(n \int \mathcal{K}\tilde{\gamma}_n^m dx + m\lambda y - n\omega t)} + c.c. \tag{5.1}$$

where λ, the longshore wave number, is:

$$\lambda = \mathcal{K} \sin\theta \tag{5.2}$$

and:

$$\tilde{\gamma}_n^m = \left[1 - (\frac{m}{n})^2 (\frac{\lambda_0}{\mathcal{K}})^2\right]^{1/2} = \cos\theta \tag{5.3}$$

where:

$$\mathcal{K} = \frac{\omega}{\sqrt{gh}} \tag{5.4}$$

Incorporating this periodicity assumption into equation (1.5) and using triad resonant interactions for both the frequency and longshore wave number components yields:

$$\begin{aligned} A_{n,x}^m + \frac{(\mathcal{K}h\tilde{\gamma}_n^m)_x}{2\mathcal{K}h\tilde{\gamma}_n^m} A_n^m - \frac{1}{6\tilde{\gamma}_n^m} i n^3 \mathcal{K}^3 h^2 A_n^m = \\ - \frac{in\mathcal{K}}{8h\tilde{\gamma}_n^m} \left\{ \sum_{l=1}^{n-1} \sum_{p=P_1}^{P_2} I_{n,l}^{m,p} A_l^p A_{n-l}^{m-p} \mathrm{e}^{i \int \Theta_{n,l}^{m,p} \mathrm{dx}} + 2 \sum_{l=1}^{N-n} \sum_{p=P_3}^{P_4} J_{n,l}^{m,p} A_l^{p*} A_{n+l}^{m+p} \mathrm{e}^{i \int \Upsilon_{n,l}^{m,p} \mathrm{dx}} \right\} \end{aligned} \tag{5.5}$$

where:

$$I_{n,l}^{m,p} = 1 + [\tilde{\gamma}_l^p \tilde{\gamma}_{n-l}^{m-p} + \frac{p}{l}\frac{m-p}{n-l}(\frac{\lambda_0}{\mathcal{K}})^2] \cdot [1 + (\frac{m}{n})^2 (\frac{\lambda_0}{\mathcal{K}})^2 + \frac{(l\tilde{\gamma}_l^p + (n-l)\tilde{\gamma}_{n-l}^{m-p})^2}{n^2}] \tag{5.6}$$

$$J_{n,l}^{m,p} = I_{n,-l}^{m,-p} \tag{5.7}$$

and the phase arguments are:

$$\Theta_{n,l}^{m,p} = l\mathcal{K}\tilde{\gamma}_l^p + (n-l)\mathcal{K}\tilde{\gamma}_{n-l}^{m-p} - n\mathcal{K}\tilde{\gamma}_n^m \tag{5.8}$$

$$\Upsilon_{n,l}^{m,p} = \Theta_{n,-l}^{m,-p} \tag{5.9}$$

This is the angular spectrum model of Kirby (1990). It is an improvement over the parabolic KP model of Liu et al. (1985) because there is no small angle restriction. However, it is still limited by the shallow water assumption in its shoaling relation. We wish to replace linear terms in the model so as to add dispersiveness to its linear shoaling and propagation characteristics. First of all, we replace the shoaling term in the model (the second term on left-hand side in Equation 5.5) with one gleaned from the conservation of energy flux:

$$\frac{(C_{gn}\tilde{\gamma}_n^m)_x}{2C_{gn}\tilde{\gamma}_n^m} \tag{5.10}$$

where C_{gn} is calculated from (3.14), the group velocity expression from the fully nonlinear extended Boussinesq equation. We saw in Section 3.6.2 that this shoaling relation compares well to linear theory for a wide range of water depths. Secondly, in the manner of Mase and Kirby (1992), we replace the dispersive term (the third term on left-hand side of Equation 5.5) with:

$$in\mathcal{K}\tilde{\gamma}_n^m \left(1 - \frac{k_n}{n\mathcal{K}}\right) \tag{5.11}$$

where the k_n is found by Equation (3.13). This results in:

$$\begin{aligned} &A_{n,x}^m + \frac{(C_{gn}\tilde{\gamma}_n^m)_x}{2C_{gn}\tilde{\gamma}_n^m} A_n^m + in\mathcal{K}\tilde{\gamma}_n^m \left(1 - \frac{k_n}{n\mathcal{K}}\right) A_n^m = \\ - &\frac{in\mathcal{K}}{8h\tilde{\gamma}_n^m} \left\{ \sum_{l=1}^{n-1} \sum_{p=P_1}^{P_2} I_{n,l}^{m,p} A_l^p A_{n-l}^{m-p} \mathrm{e}^{i\int \Theta_{n,l}^{m,p} \mathrm{dx}} + 2 \sum_{l=1}^{N-n} \sum_{p=P_3}^{P_4} J_{n,l}^{m,p} A_l^{p*} A_{n+l}^{m+p} \mathrm{e}^{i\int \Upsilon_{n,l}^{m,p} \mathrm{dx}} \right\} \end{aligned} \tag{5.12}$$

where the interaction coefficients $I_{n,l}^{m,p}$ and $J_{n,l}^{m,p}$ and the phase arguments $\Theta_{n,l}^{m,p}$ and $\Upsilon_{n,l}^{m,p}$ remain unchanged. This is the simplified angular spectrum model of the extended Boussinesq equations. We will show comparisons of this model to experimental data in the next chapter.

5.3 Angular Spectrum Model of the Fully Nonlinear Extended Boussinesq Equation

5.3.1 Longshore Periodic Waves

Equation (5.12), though now having improved dispersive properties, is inconsistent because the nonlinearity is that of shallow water Boussinesq theory. Thus, we perform an angular spectrum transformation of the fully nonlinear extended Boussinesq equation. We pick up the derivation of the parabolic version of the model (developed in Chapter 3) where the time-periodic equation for $\hat{\phi}_{\alpha n}$ and $\hat{\eta}$ were detailed. We reproduce these equations here for convenience:

$$
\begin{aligned}
& \frac{n^2\omega^2}{g}\hat{\phi}_{\alpha n} + \left(1 + \frac{n^2\omega^2 z_\alpha}{g}\right)\nabla h \cdot \nabla\hat{\phi}_{\alpha n} + \left(h + \frac{n^2\omega^2 h^2\alpha}{g}\right)\nabla^2\hat{\phi}_{\alpha n} \\
+ \; & \left(1 + 5\alpha + \sqrt{1+2\alpha}\right) h^2\nabla h \cdot \nabla(\nabla^2\hat{\phi}_{\alpha n}) + \left(\alpha + \frac{1}{3}\right) h^3\nabla^2\nabla^2\hat{\phi}_{\alpha n} \\
+ \; & \frac{in\omega}{4g}\left(\sum_{l=1}^{n-1}\nabla\hat{\phi}_{\alpha l}\cdot\nabla\hat{\phi}_{\alpha n-l} + 2\sum_{l=1}^{N-n}\nabla\hat{\phi}^*_{\alpha l}\cdot\nabla\hat{\phi}_{\alpha n+l}\right) \\
+ \; & \frac{in\omega\alpha h^2}{4g}\left[\sum_{l=1}^{n-1}\nabla\hat{\phi}_{\alpha l}\cdot\nabla(\nabla^2\hat{\phi}_{\alpha n-l}) + \nabla\hat{\phi}_{\alpha n-l}\cdot\nabla(\nabla^2\hat{\phi}_{\alpha l})\right. \\
+ \; & \left. 2\sum_{l=1}^{N-n}\nabla\hat{\phi}^*_{\alpha l}\cdot\nabla(\nabla^2\hat{\phi}_{\alpha n+l}) + \nabla\hat{\phi}_{\alpha n+l}\cdot\nabla(\nabla^2\hat{\phi}^*_{\alpha l})\right] \\
+ \; & \frac{in\omega h^2}{4g}\left(\sum_{l=1}^{n-1}\tau_{n,l}\nabla^2\hat{\phi}_{\alpha l}\nabla^2\hat{\phi}_{\alpha n-l} - 2\sum_{l=1}^{N-n}\zeta_{n,l}\nabla^2\hat{\phi}^*_{\alpha l}\nabla^2\hat{\phi}_{\alpha n+l}\right) \\
+ \; & \frac{i\omega}{4g}\nabla\cdot\left[\sum_{l=1}^{n-1} l(\hat{\phi}_{\alpha l} + \alpha h^2\nabla^2\hat{\phi}_{\alpha l})\nabla\hat{\phi}_{\alpha n-l} + (n-l)(\hat{\phi}_{\alpha n-l} + \alpha h^2\nabla^2\hat{\phi}_{\alpha n-l})\nabla\hat{\phi}_{\alpha l}\right. \\
+ \; & \left. 2\sum_{l=1}^{N-n}(n+l)(\hat{\phi}_{\alpha n+l} + \alpha h^2\nabla^2\hat{\phi}_{\alpha n+l})\nabla\hat{\phi}^*_{\alpha l} - l(\hat{\phi}^*_{\alpha l} + \alpha h^2\nabla^2\hat{\phi}^*_{\alpha l})\nabla\hat{\phi}_{\alpha n+l}\right] \\
+ \; & \frac{i\omega\alpha h^2}{4g}\nabla\cdot\left[\sum_{l=1}^{n-1} l\hat{\phi}_{\alpha l}\nabla(\nabla^2\hat{\phi}_{\alpha n-l}) + (n-l)\hat{\phi}_{\alpha n-l}\nabla(\nabla^2\hat{\phi}_{\alpha l})\right. \\
+ \; & \left. 2\sum_{l=1}^{N-n}(n+l)\hat{\phi}_{\alpha n+l}\nabla(\nabla^2\hat{\phi}^*_{\alpha l}) - l\hat{\phi}^*_{\alpha l}\nabla(\nabla^2\hat{\phi}_{\alpha n+l})\right] = 0 \qquad (5.13)
\end{aligned}
$$

and:

$$
\begin{array}{rl}
- & in\omega\hat{\phi}_{\alpha n} + g\hat{\eta}_n - in\omega z_\alpha \nabla h \cdot \nabla\hat{\phi}_{\alpha n} - in\omega\alpha h^2 \nabla^2 \hat{\phi}_{\alpha n} + \frac{1}{4}\left(\sum_{l=1}^{n-1} \nabla\hat{\phi}_{\alpha l} \cdot \nabla\hat{\phi}_{\alpha n-l}\right. \\
+ & \left. 2\sum_{l=1}^{N-n} \nabla\hat{\phi}^*_{\alpha l} \cdot \nabla\hat{\phi}_{\alpha n+l}\right) + \frac{i\omega h}{4}\left[\sum_{l=1}^{n-1} (n-l)\hat{\eta}_l \nabla^2\hat{\phi}_{\alpha n-l} + l\hat{\eta}_{n-l}\nabla^2\hat{\phi}_{\alpha l}\right. \\
+ & \left. 2\sum_{l=1}^{N-n} (n+l)\hat{\eta}^*_l \nabla^2\hat{\phi}_{\alpha n+l} - l\hat{\eta}_{n+l}\nabla^2\hat{\phi}^*_{\alpha l}\right] + \frac{\alpha h^2}{4}\left[\sum_{l=1}^{n-1} \nabla\hat{\phi}_{\alpha l} \cdot \nabla(\nabla^2\hat{\phi}_{\alpha n-l})\right. \\
+ & \left. \nabla\hat{\phi}_{\alpha n-l} \cdot \nabla(\nabla^2\hat{\phi}_{\alpha l}) + 2\sum_{l=1}^{N-n} \nabla\hat{\phi}^*_{\alpha l} \cdot \nabla(\nabla^2\hat{\phi}_{\alpha n+l} + \nabla\hat{\phi}_{\alpha n+l} \cdot \nabla(\nabla^2\hat{\phi}^*_{\alpha l})\right] \\
+ & \frac{h^2}{4}\left(\sum_{l=1}^{n-1} \nabla^2\hat{\phi}_{\alpha l}\nabla^2\hat{\phi}_{\alpha n-l} + 2\sum_{l=1}^{N-n} \nabla^2\hat{\phi}^*_{\alpha l}\nabla^2\hat{\phi}_{\alpha n-l}\right) = 0
\end{array}
\qquad (5.14)
$$

where $\tau_{n,l}$ and $\zeta_{n,l}$ from (5.13) are defined as:

$$
\tau_{n,l} = \frac{(n-l)^2 + l(n-l) + l^2}{l(n-l)} \qquad (5.15)
$$

$$
\zeta_{n,l} = \frac{(n+l)^2 - l(n+l) + l^2}{l(n+l)} \qquad (5.16)
$$

Now we explicitly apply the longshore periodicity assumption:

$$
\hat{\phi}_{\alpha n} = \sum_{m=-M}^{M} \tilde{\phi}^m_{\alpha n} e^{im\lambda y} \qquad (5.17)
$$

where λ is our base longshore wave number. Substituting this into (5.13) and applying the resonant interaction conditions between triads of longshore wave number components yields:

$$
\begin{array}{rl}
 & \frac{n^2\omega^2}{g}\tilde{\phi}^m_{\alpha n} + \left(1 + \frac{n^2\omega^2 z_\alpha}{g}\right) h_x \tilde{\phi}^m_{\alpha nx} + \left(h + \frac{n^2\omega^2 h^2 \alpha}{g}\right)\left(\tilde{\phi}^m_{\alpha nxx} - m^2\lambda^2\tilde{\phi}^m_{\alpha n}\right) \\
+ & (1 + 5\alpha + \sqrt{1+2\alpha})h^2 h_x(\tilde{\phi}^m_{\alpha nxxx} - m^2\lambda^2\tilde{\phi}^m_{\alpha nx}) \\
+ & \left(\alpha + \frac{1}{3}\right) h^3(\tilde{\phi}^m_{\alpha nxxxx} - 2m^2\lambda^2\tilde{\phi}^m_{\alpha nxx} + m^4\lambda^4\tilde{\phi}^m_{\alpha n}) \\
+ & \xi_1 + \xi_2 + \xi_3 + \xi_4 = 0
\end{array}
\qquad (5.18)
$$

where:

$$
\begin{aligned}
\xi_1 = {} & \Biggl(\sum_{l=1}^{n-1}\sum_{p=-M}^{M} 2n\bigl[\tilde\phi^{p}_{\alpha l,x}\tilde\phi^{m-p}_{\alpha n-l,x} - p(m-p)\lambda^2\tilde\phi^{p}_{\alpha l}\tilde\phi^{m-p}_{\alpha n-l}\bigr]\\
+ {} & n\alpha h^2\bigl[\tilde\phi^{p}_{\alpha l,xx}\tilde\phi^{m-p}_{\alpha n-l,xx} - (m-p)^2\lambda^2\tilde\phi^{p}_{\alpha l,xx}\tilde\phi^{m-p}_{\alpha n-l} - p^2\lambda^2\tilde\phi^{p}_{\alpha l}\tilde\phi^{m-p}_{\alpha n-l,xx}\\
+ {} & p^2(m-p)^2\lambda^4\tilde\phi^{p}_{\alpha l}\tilde\phi^{m-p}_{\alpha n-l}\bigr] + l\bigl\{\tilde\phi^{p}_{\alpha l}\tilde\phi^{m-p}_{\alpha n-l,xx} - (m-p)^2\lambda^2\tilde\phi^{p}_{\alpha l}\tilde\phi^{m-p}_{\alpha n-l}\\
+ {} & \alpha h^2\bigl[\tilde\phi^{p}_{\alpha l,xxx}\tilde\phi^{m-p}_{\alpha n-l,x} - p^2\lambda^2\tilde\phi^{p}_{\alpha lx}\tilde\phi^{m-p}_{\alpha n-l,x} - p(m-p)\lambda^2\tilde\phi^{p}_{\alpha l,xx}\tilde\phi^{m-p}_{\alpha n-l}\\
+ {} & p^3(m-p)\lambda^4\tilde\phi^{p}_{\alpha l}\tilde\phi^{m-p}_{\alpha n-l}\bigr]\bigr\} + (n-l)\bigl\{\tilde\phi^{p}_{\alpha l,xx}\tilde\phi_{\alpha n-l} - p^2\lambda^2\tilde\phi^{p}_{\alpha l}\tilde\phi^{m-p}_{\alpha n-l}\\
+ {} & \alpha h^2\bigl[\tilde\phi_{\alpha l,x}\tilde\phi_{\alpha n-l,xxx} - (m-p)^2\lambda^2\tilde\phi^{p}_{\alpha l,x}\tilde\phi^{m-p}_{\alpha n-l,x} - p(m-p)\lambda^2\tilde\phi^{p}_{\alpha l}\tilde\phi^{m-p}_{\alpha n-l,xx}\\
+ {} & p(m-p)^3\lambda^4\tilde\phi^{p}_{\alpha l}\tilde\phi^{m-p}_{\alpha}\bigr]\bigr\} + 2\sum_{l=1}^{N-n}\sum_{p=-M}^{M} 2n\bigl[\tilde\phi^{p*}_{\alpha l,x}\tilde\phi^{m+p}_{\alpha n+l,x}\\
+ {} & p(m+p)\lambda^2\tilde\phi^{p*}_{\alpha l}\tilde\phi^{m+p}_{\alpha n+l}\bigr] + n\alpha h^2\bigl[\tilde\phi^{p*}_{\alpha l,xx}\tilde\phi^{m+p}_{\alpha n+l,xx} - p^2\lambda^2\tilde\phi^{p*}_{\alpha l}\tilde\phi^{m+p}_{\alpha n+l,xx}\\
- {} & (m+p)^2\lambda^2\tilde\phi^{p*}_{\alpha l,xx}\tilde\phi^{m+p}_{\alpha n+l} + p^2(m+p)^2\lambda^4\tilde\phi^{p*}_{\alpha l}\tilde\phi^{m+p}_{n+l}\bigr] + (n+l)\bigl\{\tilde\phi^{p*}_{\alpha l,xx}\tilde\phi^{m+p}_{\alpha n+l}\\
- {} & p^2\lambda^2\tilde\phi^{p*}_{\alpha l}\tilde\phi^{m+p}_{\alpha n+l} + \alpha h^2\bigl[\tilde\phi^{p*}_{\alpha l,x}\tilde\phi^{m+p}_{\alpha n+l,xxx} - (m+p)^2\lambda^2\tilde\phi^{p*}_{\alpha l,x}\tilde\phi^{m+p}_{\alpha n+l,x}\\
+ {} & p(m+p)\lambda^2\tilde\phi^{p*}_{\alpha l}\tilde\phi^{m+p}_{\alpha n+l,xx} - p(m+p)^3\lambda^4\tilde\phi^{p*}_{\alpha l}\tilde\phi^{m+p}_{\alpha n+l}\bigr]\bigr\} - l\bigl\{\tilde\phi^{p*}_{\alpha l}\tilde\phi^{m+p}_{\alpha n+l,xx}\\
- {} & (m+p)^2\lambda^2\tilde\phi^{p*}_{\alpha l}\tilde\phi^{m+p}_{\alpha n+l} + \alpha h^2\bigl[\tilde\phi^{p*}_{\alpha l,xxx}\tilde\phi^{m+p}_{\alpha n+l,x} - p^2\lambda^2\tilde\phi^{p*}_{\alpha l,x}\tilde\phi^{m+p}_{\alpha n+l,x}\\
+ {} & p(m+p)\lambda^2\tilde\phi^{p*}_{\alpha l,xx}\tilde\phi^{m+p}_{\alpha n+l} + p^3(m+p)\lambda^4\phi^{p*}_{\alpha l}\tilde\phi^{m+p}_{\alpha n+l}\bigr]\bigr\}\Biggr)
\end{aligned}
\tag{5.19}
$$

$$
\begin{aligned}
\xi_2 = {} & \frac{in\omega\alpha h^2}{4g}\Biggl[\sum_{l=1}^{n-1}\sum_{p=-M}^{M}\tilde\phi^{p}_{\alpha l,x}\tilde\phi^{m-p}_{\alpha n-l,xxx} - (m-p)^2\lambda^2\tilde\phi^{p}_{\alpha l,x}\tilde\phi_{\alpha n-l,x}\\
- {} & p(m-p)\lambda^2\tilde\phi^{p}_{\alpha l}\tilde\phi^{m-p}_{\alpha n-l,xx} + p(m-p)^3\lambda^4\tilde\phi^{p}_{\alpha l}\tilde\phi^{m-p}_{\alpha n-l} + \tilde\phi^{p}_{\alpha l,xxx}\tilde\phi^{m-p}_{\alpha n-l,x}\\
- {} & p^2\lambda^2\tilde\phi^{p}_{\alpha l,x}\tilde\phi^{m-p}_{\alpha n-l,x} - p(m-p)\lambda^2\tilde\phi^{p}_{\alpha l,xx}\tilde\phi^{m-p}_{\alpha n-l} + p^3(m-p)\tilde\phi^{p}_{\alpha l}\tilde\phi^{m-p}_{\alpha n-l}\\
+ {} & 2\sum_{l=1}^{N-n}\sum_{p=-M}^{M}\tilde\phi^{p*}_{\alpha l,x}\tilde\phi^{m+p}_{\alpha n+l,xxx} - (m+p)^2\lambda^2\tilde\phi^{p*}_{\alpha l,x}\tilde\phi^{m+p}_{\alpha n+l,x} + p(m+p)\lambda^2\tilde\phi^{p*}_{\alpha l}\tilde\phi^{m+p}_{\alpha n+l,xx}\\
- {} & p(m+p)^3\lambda^4\tilde\phi^{p*}_{\alpha l}\tilde\phi^{m+p}_{\alpha n+l} + \tilde\phi^{p*}_{\alpha l,xxx}\tilde\phi^{m+p}_{\alpha n+l,x} - p^2\lambda^2\tilde\phi^{p*}_{\alpha l,x}\tilde\phi^{m+p}_{\alpha n+l,x}\\
+ {} & p(m+p)\lambda^2\tilde\phi^{p*}_{\alpha l,xx}\tilde\phi^{m+p}_{\alpha n+l} - p^3(m+p)\lambda^4\tilde\phi^{p*}_{\alpha l}\tilde\phi^{m+p}_{\alpha n+l}\Biggr]
\end{aligned}
\tag{5.20}
$$

$$
\xi_3 = \frac{in\omega h^2}{4g}\Biggl\{\sum_{l=1}^{n-1}\sum_{p=-M}^{M}\tau_{n,l}\bigl[\tilde\phi^{p}_{\alpha l,xx}\tilde\phi^{m-p}_{\alpha n-l,xx} - p^2\lambda^2\tilde\phi^{p}_{\alpha l}\tilde\phi^{m-p}_{\alpha n-l,xx}
$$

$$
\begin{aligned}
- & \quad (m-p)^2\lambda^2\tilde{\phi}^{p}_{\alpha l,xx}\tilde{\phi}^{m-p}_{\alpha n-l} + p^2(m-p)^2\lambda^4\tilde{\phi}^{p}_{\alpha l}\tilde{\phi}^{m-p}_{\alpha n-l}\Big] \\
- & \quad 2\sum_{l=1}^{N-n}\sum_{p=-M}^{M}\zeta_{n,l}\Big[\tilde{\phi}^{p*}_{\alpha l,xx}\tilde{\phi}^{m+p}_{\alpha n+l,xx} - p^2\lambda^2\tilde{\phi}^{p*}_{\alpha l}\tilde{\phi}^{m+p}_{\alpha n+l,xx} - (m+p)^2\lambda^2\tilde{\phi}^{p*}_{\alpha l,xx}\tilde{\phi}^{m+p}_{\alpha n+l} \\
+ & \quad p^2(m+p)^2\lambda^4\tilde{\phi}^{p*}_{\alpha l}\tilde{\phi}^{m+p}_{\alpha n+l}\Big]\Big\}
\end{aligned}
\tag{5.21}
$$

$$
\begin{aligned}
\xi_4 = & \frac{i\omega\alpha h^2}{4g}\left\{\sum_{l=1}^{n-1}\sum_{p=-M}^{M} l\Big[\tilde{\phi}^{p}_{\alpha l,x}\tilde{\phi}^{m-p}_{\alpha n-l,xxx} - (m-p)^2\lambda^2\tilde{\phi}^{p}_{\alpha l,x}\tilde{\phi}^{m-p}_{\alpha n-l,x}\right. \\
- & \quad p(m-p)\lambda^2\tilde{\phi}^{p}_{\alpha l}\tilde{\phi}^{m-p}_{\alpha n-l,xx} + p(m-p)^3\lambda^4\tilde{\phi}^{p}_{\alpha l}\tilde{\phi}^{m-p}_{\alpha n-l} + \tilde{\phi}^{p}_{\alpha l}\tilde{\phi}^{m-p}_{\alpha n-l,xxxx} \\
- & \quad 2(m-p)^2\lambda^2\tilde{\phi}^{p}_{\alpha l}\tilde{\phi}^{m-p}_{\alpha n-l,xx} + (m-p)^4\lambda^4\tilde{\phi}^{p}_{\alpha l}\tilde{\phi}^{m-p}_{\alpha n-l}\Big] + (n-l)\Big[\tilde{\phi}^{p}_{\alpha l,xxx}\tilde{\phi}^{m-p}_{\alpha n-l,x} \\
- & \quad p^2\lambda^2\tilde{\phi}^{p}_{\alpha l,x}\tilde{\phi}^{m-p}_{\alpha n-l,x} - p(m-p)\lambda^2\tilde{\phi}_{\alpha l,xx}\tilde{\phi}^{m-p}_{\alpha n-l} \\
+ & \quad p^3(m-p)\lambda^4\tilde{\phi}^{p}_{\alpha l}\tilde{\phi}^{m-p}_{\alpha n-l} + \tilde{\phi}_{\alpha l,xxxx}\tilde{\phi}^{m-p}_{\alpha n-l} - 2p^2\lambda^2\tilde{\phi}^{p}_{\alpha l,xx}\tilde{\phi}^{m-p}_{\alpha n-l} + p^4\lambda^4\tilde{\phi}^{p}_{\alpha l}\tilde{\phi}^{m-p}_{\alpha n-l}\Big] \\
+ & \quad 2\sum_{l=1}^{N-n}\sum_{p=-M}^{M}(n+l)\Big[\tilde{\phi}^{p*}_{\alpha l,xxx}\tilde{\phi}^{m+p}_{\alpha n+l,x} - p^2\lambda^2\tilde{\phi}^{p*}_{\alpha l,x}\tilde{\phi}^{m+p}_{\alpha n+l,x} \\
+ & \quad p(m+p)\lambda^2\tilde{\phi}^{p*}_{\alpha l,xx}\tilde{\phi}^{m+l}_{\alpha n+l} - p^3(m+p)\lambda^4\tilde{\phi}^{p*}_{\alpha l}\tilde{\phi}^{m+p}_{\alpha n+l} + \tilde{\phi}^{p*}_{\alpha l,xxxx}\tilde{\phi}^{m+p}_{\alpha n+l} \\
- & \quad 2p^2\lambda^2\tilde{\phi}^{p*}_{\alpha l,xx}\tilde{\phi}^{m+p}_{\alpha n+l} + p^4\lambda^4\tilde{\phi}^{p*}_{\alpha l}\tilde{\phi}^{m+p}_{\alpha n+l}\Big] - l\Big[\tilde{\phi}^{p*}_{\alpha l,x}\tilde{\phi}^{m+p}_{\alpha n+l,xxx} \\
- & \quad (m+p)^2\lambda^2\tilde{\phi}^{p*}_{\alpha l,x}\tilde{\phi}^{m+p}_{\alpha n+l,x}p(m+p)\lambda^2\tilde{\phi}^{p*}_{\alpha l}\tilde{\phi}^{m+p}_{\alpha n+l,xx} - p(m+p)^3\lambda^4\tilde{\phi}^{p*}_{\alpha l}\tilde{\phi}^{m+p}_{\alpha n+l} \\
+ & \quad \tilde{\phi}^{p*}_{\alpha l}\tilde{\phi}^{m+p}_{\alpha n+l,xxxx} - 2(m+p)^2\lambda^2\tilde{\phi}^{p*}_{\alpha l}\tilde{\phi}^{m+p}_{\alpha n+l,xx} + (m+p)^4\lambda^4\tilde{\phi}^{p*}_{\alpha l}\tilde{\phi}^{m+p}_{\alpha n+l}\Big]\Big\}
\end{aligned}
\tag{5.22}
$$

To find the time-periodic, longshore-periodic equation for the free surface elevation, we assume:

$$
\hat{\eta}_n = \sum_{m=-M}^{M}\tilde{\eta}^{m}_{n}e^{im\lambda y}
\tag{5.23}
$$

and substitute this and (5.17) into (5.14) to obtain:

$$
\tilde{\eta}^{m}_{n} = \frac{in\omega}{g}\left(\tilde{\phi}^{m}_{\alpha n} + z_\alpha h_x\tilde{\phi}_{\alpha n,x} + \frac{\alpha h^2}{g}(\tilde{\phi}^{m}_{\alpha n,xx} - m^2\lambda^2\tilde{\phi}^{m}_{\alpha n})\right) + \xi_5 + \frac{i}{n\omega}(\xi_2 + \xi_3)
\tag{5.24}
$$

where:

$$
\xi_5 = -\frac{1}{4g}\left[\sum_{l=1}^{n-1}\sum_{p=-M}^{M}\tilde{\phi}^{p}_{\alpha l,x}\tilde{\phi}^{m-p}_{\alpha n-l,x} - p(m-p)\lambda^2\tilde{\phi}^{p}_{\alpha l}\tilde{\phi}^{m-p}_{\alpha n-l}\right.
$$

$$+ \quad 2\sum_{l=1}^{N-n}\sum_{p=-M}^{M}\tilde{\phi}^{p*}_{\alpha l,x}\tilde{\phi}^{m+p}_{\alpha n+l,x} + p(m+p)\lambda^2\tilde{\phi}^{p*}_{\alpha l}\tilde{\phi}^{m+p}_{\alpha n+l}\Bigg] \tag{5.25}$$

5.3.2 Shoaling Waves

Equation (5.18) represents the evolution of time-periodic, longshore-periodic waves that can travel forward and backward in x. Here we explicitly restrict attention to forward-propagating waves:

$$\tilde{\phi}^m_{\alpha n} = B^m_n(x)e^{i\int k_n\tilde{\gamma}^m_n dx} \tag{5.26}$$

$$\tilde{\eta}^m_n = A^m_n(x)e^{i\int k_n\tilde{\gamma}^m_n dx} \tag{5.27}$$

where $\tilde{\gamma}^m_n$ is now:

$$\tilde{\gamma}^m_n = \left[1 - \left(\frac{m\lambda}{k_n}\right)^2\right]^{1/2} \tag{5.28}$$

which is different from (5.3) since we now have a dispersive wave number k_n rather than the nondispersive $n\mathcal{K}$. As before, B^m_n and A^m_n are assumed to be slowly varying functions of x, so that terms like $B^m_{n,xx}$ and $A^m_{n,xx}$ are neglected. Substituting (5.26) into (5.18) yields:

$$\begin{aligned}
& 2k_n\tilde{\gamma}^m_n\left[h + \frac{n^2\omega^2h^2\alpha}{g} - 2h^3(\alpha+\frac{1}{3})(k_n^2\tilde{\gamma}^{m\,2}_n + m^2\lambda^2)\right]B^m_{nx} \\
+ \quad & k_n\tilde{\gamma}^m_n\left[1 + \frac{n^2\omega^2z_\alpha}{g} - h^2(1+5\alpha+\sqrt{1+2\alpha})(k_n^2\tilde{\gamma}^{m\,2}_n + m^2\lambda^2)\right]h_xB^m_n \\
+ \quad & \left[h + \frac{n^2\omega^2h^2\alpha}{g} - 6k_n^2\tilde{\gamma}^{m\,2}_n(\alpha+\frac{1}{3})h^3 - 2m^2\lambda^2(\alpha+\frac{1}{3})h^3\right](k_n\tilde{\gamma}^m_n)_xB^m_n \\
- \quad & \frac{\omega}{4g}\left(\sum_{l=1}^{n-1}\sum_{p=P_1}^{P_2}\tilde{I}B^p_lB^{m-p}_{n-l}e^{i\tilde{\Theta}} + 2\sum_{l=1}^{N-n}\sum_{p=P_3}^{F_4}\tilde{J}B^{p*}_lB^{m+p}_{n+l}e^{i\tilde{\Upsilon}}\right) = 0
\end{aligned} \tag{5.29}$$

where:

$$\tilde{I} = l(k_{n-l}\tilde{\gamma}^{m-p}_{n-l})^2 + 2nk_l\tilde{\gamma}^p_lk_{n-l}\tilde{\gamma}^{m-p}_{n-l} + (n-l)(k_l\tilde{\gamma}^p_l)^2 + \big[l(m-p)^2$$

$$
\begin{aligned}
&+ \quad 2np(m-p) + (n-l)p^2 \Big] \lambda^2 - nh^2 \tau_{n,l} \Big[(k_l \tilde{\gamma}_l^p)^2 (k_{n-l} \tilde{\gamma}_{n-l}^{m-p})^2 \\
&+ \quad p^2 \lambda^2 (k_{n-l} \tilde{\gamma}_{n-l}^{m-p})^2 + (m-p)^2 \lambda^2 (k_l \tilde{\gamma}_l^p)^2 + p^2 (m-p)^2 \lambda^4 \Big] \\
&- \quad \alpha h^2 \Big\{ (n-l)(k_l \tilde{\gamma}_l^p)^4 + 2n(k_l \tilde{\gamma}_l^p)^3 k_{n-l} \tilde{\gamma}_{n-l}^{m-p} + n(k_l \tilde{\gamma}_l^p)^2 (k_{n-l} \tilde{\gamma}_{n-l}^{m-p})^2 \\
&+ \quad 2n k_l \tilde{\gamma}_l^p (k_{n-l} \tilde{\gamma}_{n-l}^{m-p})^3 + l(k_{n-l} \tilde{\gamma}_{n-l}^{m-p})^4 + \Big[n(m-p)^2 + 2np(m-p) \\
&+ \quad 2(n-l)p^2 \Big] \lambda^2 (k_l \tilde{\gamma}_l^p)^2 + 2n \Big[p^2 + (m-p)^2 \Big] \lambda^2 k_l \tilde{\gamma}_l^p k_{n-l} \tilde{\gamma}_{n-l}^{m-p} \\
&+ \quad \Big[np^2 + 2np(m-p) + 2l(m-p)^2 \Big] \lambda^2 (k_{n-l} \tilde{\gamma}_{n-l}^{m-p})^2 + \Big[l(m-p)^4 \\
&+ \quad 2np(m-p)^3 + np^2(m-p)^2 + 2np^3(m-p) + (n-l)p^4 \Big] \lambda^4 \Big\} \qquad (5.30)
\end{aligned}
$$

$$
\begin{aligned}
&\tilde{J} = (n+l)(k_l \tilde{\gamma}_l^p)^2 - 2n k_l \tilde{\gamma}_l^p k_{n+l} \tilde{\gamma}_{n+l}^{m+p} - l(k_{n+l} \tilde{\gamma}_{n+l}^{m+p})^2 + \Big[(n+l)p^2 \\
&- \quad 2np(m+p) - l(m+p)^2 \Big] \lambda^2 + nh^2 \zeta_{n,l} \Big[(k_l \tilde{\gamma}_l^p)^2 (k_{n+l} \tilde{\gamma}_{n+l}^{m+p})^2 \\
&+ \quad p^2 \lambda^2 (k_{n+l} \tilde{\gamma}_{n+l}^{m+p})^2 + (m+p)^2 \lambda^2 (k_l \tilde{\gamma}_l^p)^2 + p^2 (m+p)^2 \lambda^4 \Big] \\
&- \quad \alpha h^2 \Big\{ (n+l)(k_l \tilde{\gamma}_l^p)^4 - 2n(k_l \tilde{\gamma}_l^p)^3 k_{n+l} \tilde{\gamma}_{n+l}^{m+p} + n(k_l \tilde{\gamma}_l^p)^2 (k_{n+l} \tilde{\gamma}_{n+l}^{m+p})^2 \\
&- \quad 2n k_l \tilde{\gamma}_l^p (k_{n+l} \tilde{\gamma}_{n+l}^{m+p})^3 - l(k_{n+l} \tilde{\gamma}_{n+l}^{m+p})^4 + \Big[n(m+p)^2 - 2np(m+p) \\
&+ \quad 2(n+l)p^2 \Big] \lambda^2 (k_l \tilde{\gamma}_l^p)^2 - 2n \Big[p^2 + (m+p)^2 \Big] \lambda^2 k_l \tilde{\gamma}_l^p k_{n+l} \tilde{\gamma}_{n+l}^{m+p} \\
&+ \quad \Big[np^2 - 2np(m+p) - 2l(m+p)^2 \Big] \lambda^2 (k_{n+l} \tilde{\gamma}_{n+l}^{m+p})^2 + \Big[(n+l)p^4 \\
&- \quad 2np^3(m+p) + np^2(m+p)^2 - 2np(m+p)^3 - l(m+p)^4 \Big] \lambda^4 \Big\} \qquad (5.31)
\end{aligned}
$$

and the phase arguments are:

$$\tilde{\Theta} = \int (k_l \tilde{\gamma}_l^p + k_{n-l} \tilde{\gamma}_{n-l}^{m-p} - k_n \tilde{\gamma}_n^m) dx \qquad (5.32)$$

$$\tilde{\Upsilon} = \int (k_{n+l} \tilde{\gamma}_{n+l}^{m+p} - k_l \tilde{\gamma}_l^p - k_n \tilde{\gamma}_n^m) dx \qquad (5.33)$$

We wish to exclude evanescent modes, which decay in x, so we need to keep (5.28) real. This exclusion is done because nonlinearity may cause a mode which would be evanescent in a linearized wave field to propagate (Kirby 1990).

Thus we can set our range of longshore modes M differently for each frequency mode n as follows:

$$M_n \leq \frac{k_n}{\lambda} \tag{5.34}$$

Therefore, the range of the summations over the longshore modes must be limited in such a way as to account for different ranges for different frequencies. These ranges are determined as follows:

$$\begin{aligned}
P_1 &= \max(-M_l, -M_{n-l} + m) && (5.35)\\
P_2 &= \min(M_l, M_{n-l} + m) && (5.36)\\
P_3 &= \max(-M_l, -M_{n+l} - m) && (5.37)\\
P_4 &= \min(M_l, M_{n+l} - m) && (5.38)
\end{aligned}$$

Equation (5.29) is an angular spectrum model for the amplitudes of ϕ_α. To calculate the amplitudes of the free surface elevation η, we substitute (5.26) and (5.27) into (5.24) to obtain:

$$\begin{aligned}
& A_n^m = \frac{in\omega}{g}\left[1 - \alpha h^2(k_n^2\tilde{\gamma}_n^{m2} + m^2\lambda^2)\right] B_n^m - \frac{n\omega z_\alpha k_n \tilde{\gamma}_n^m}{g} h_x B_n^m \\
- \;& \frac{n\omega\alpha h^2}{g}(k_n\tilde{\gamma}_n^m)_x B_n^m - \frac{2n\omega\alpha h^2 k_n\tilde{\gamma}_n^m}{g} B_{nx}^m \\
+ \;& \frac{1}{4g}\left(\sum_{l=1}^{n-1}\sum_{p=P_1}^{P_2} \tilde{I}' B_l^p B_{n-l}^{m-p} e^{i\tilde{\Theta}} - 2\sum_{l=1}^{N-n}\sum_{p=P_3}^{P_4} \tilde{J}' B_l^{p*} B_{n+l}^{m+p} e^{i\tilde{\Upsilon}}\right) \qquad (5.39)
\end{aligned}$$

where:

$$\begin{aligned}
& \tilde{I}' = k_l\tilde{\gamma}_l^p k_{n-l}\tilde{\gamma}_{n-l}^{m-p} + p(m-p)\lambda^2 - \alpha h^2\left\{k_l\tilde{\gamma}_l^p(k_{n-l}\tilde{\gamma}_{n-l}^{m-p})^3 + (k_l\tilde{\gamma}_l^p)^3 k_{n-l}\tilde{\gamma}_{n-l}^{m-p}\right. \\
+ \;& p(m-p)\lambda^2[(k_l\tilde{\gamma}_l^p)^2 + (k_{n-l}\tilde{\gamma}_{n-l}^{m-p})^2] + [p^2 + (m-p)^2]\lambda^2 k_l\tilde{\gamma}_l^p k_{n-l}\tilde{\gamma}_{n-l}^{m-p} \\
+ \;& \left.[p(m-p)^3 + p^3(m-p)]\lambda^4\right\} - h^2\tau_{n,l}\left[(k_l\tilde{\gamma}_l^p)^2(k_{n-l}\tilde{\gamma}_{n-l}^{m-p})^2 + p^2\lambda^2(k_{n-l}\tilde{\gamma}_{n-l}^{m-p})^2\right. \\
+ \;& \left.(m-p)^2\lambda^2(k_l\tilde{\gamma}_l^p)^2 + p^2(m-p)^2\lambda^4\right] \qquad (5.40)
\end{aligned}$$

$$
\begin{aligned}
\tilde{J}' = {} & k_l\tilde{\gamma}_l^p k_{n+l}\tilde{\gamma}_{n+l}^{m-p} + p(m+p)\lambda^2 - \alpha h^2 \left\{ k_l\tilde{\gamma}_l^p (k_{n+l}\tilde{\gamma}_{n+l}^{m+p})^3 + (k_l\tilde{\gamma}_l^p)^3 k_{n+l}\tilde{\gamma}_{n+l}^{m+p} \right. \\
+ {} & p(m+p)\lambda^2[(k_l\tilde{\gamma}_l^p)^2 + (k_{n+l}\tilde{\gamma}_{n+l}^{m+p})^2] + [p^2 + (m+p)^2]\lambda^2 k_l\tilde{\gamma}_l^p k_{n+l}\tilde{\gamma}_{n+l}^{m+p} \\
+ {} & \left. [p(m+p)^3 + p^3(m+p)]\lambda^4 \right\} - h^2\zeta_{n,l} \left[(k_l\tilde{\gamma}_l^p)^2 (k_{n+l}\tilde{\gamma}_{n+l}^{m+p})^2 + p^2\lambda^2 (k_{n+l}\tilde{\gamma}_{n+l}^{m+p})^2 \right. \\
+ {} & \left. (m+p)^2\lambda^2 (k_l\tilde{\gamma}_l^p)^2 + p^2(m+p)^2\lambda^4 \right]
\end{aligned}
\tag{5.41}
$$

Equations (5.29) and (5.39) comprise the angular spectrum model of the fully nonlinear extended Boussinesq equation.

5.4 Permanent Form Solutions

We will discuss comparisons to experimental data in the next chapter. Simulation of this experiment, the Mach stem reflection experiments of Hammack, et al. (1990), requires that a permanent form solution of the model in question be used as input. In this section we discuss the formulation of these permanent form solutions.

For the simplified extended angular spectrum Boussinesq model (5.12), we first write the model in one-dimensional form over a flat bottom:

$$
A_{n,x} + in\mathcal{K}\left(1 - \frac{k_n}{n\mathcal{K}}\right) A_n = -\frac{3in\mathcal{K}}{8h}\left(\sum_{l=1}^{n-1} A_l A_{n-l} + 2\sum_{l=1}^{N-n} A_l^* A_{n+l}\right) \tag{5.42}
$$

where the 3 that appears before the nonlinear summations is the one-dimensional reduction of the interaction coefficients $I_{n,l}^{m,p}$ and $J_{n,l}^{m,p}$ of equations (5.6) and (5.7), respectively. Recall that the A_n are complex; since the phase functions associated with the propagating wave form use the linear wave number, the phase of the complex amplitude is expected to pick up nonlinear distortions to the wave number due to amplitude effects. This is sufficient for wave field evolution. However, for the purpose of calculating waves of permanent form, we find it more convenient to use the following alternative definition of η:

$$\eta = \sum_{n=1}^{N} \frac{a'_n(x)}{2} e^{in[(k_1+k')x-\omega t]} + c.c. \tag{5.43}$$

where the a'_n is real, k_1 is the solution to the dispersion relation (3.11) for the base frequency ω_1, and k' is the distortion to the wave number in the phase function due to nonlinear effects. This is related to A_n by:

$$A_n = a'_n e^{in[(k_1+k')-\mathcal{K}]x} \tag{5.44}$$

Substituting this into (5.42) and dropping the $a'_{n,x}$ term (no change in energy flux) gives:

$$[n(k_1+k') - k_n]a'_n + \frac{3n\mathcal{K}}{8h}\left(\sum_{l=1}^{n-1} a'_l a'_{n-l} + 2\sum_{l=1}^{N-n} a'^*_l a'_{n+l}\right) = 0 \tag{5.45}$$

We will solve simultaneously a series of equations of the form (5.45), one for each harmonic. Our unknowns are the amplitudes a'_n, and the wave number distortion k'. We require one more equation to fully close the system. We define the wave height as being equal to twice the sum of the amplitudes of the odd harmonics, or:

$$H = 2\sum_{n=1,3,5,\ldots}^{N} a'_n \tag{5.46}$$

This is our last equation. Thus for any given wave period, wave height and water depth, we can calculate a'_n and wave number distortion k'. We use the Newton-Raphson method to solve the equations simultaneously. The resulting amplitudes a'_n and wave number distortion k', when input into the model (Equation 5.12) for the case of uni-directional wave propagation over a flat bottom, will yield a wave of permanent form, with no change in the wave shape. The permanent form solution of the nonlinear mild-slope equation (Equation 2.55) is similar to this development.

For the fully nonlinear extended Boussinesq equations, the permanent form solution is the same in principle, with some differences in the details. The development of this solution was done by Chen and Liu (1993); we use their methodology here. Referring back to Equation (3.27), we note the absence of any term proportional to B_n which is *not* proportional to bottom slope. This is because the coefficient of this term is the linear dispersion relation, which would cause the entire term to vanish. In this case, however, the linear dispersion relation will not be the sole determinant of the wave number, as we have amplitude effects as well. Thus, we must retain this term. If we write out Equation (3.27) for one dimension over a flat bottom with the dispersion term retained we obtain:

$$\begin{aligned} & \frac{n^2\omega^2}{g}B_n - \left(h + \frac{n^2\omega^2h^2\alpha}{g}\right)k_n^2B_n + 2i\left[k_n\left(h + \frac{n^2\omega^2h^2\alpha}{g}\right)\right. \\ - & \left. 2k_n^3h^3\left(\alpha + \frac{1}{3}\right)\right]B_{n,x} + \left(\alpha + \frac{1}{3}\right)h^3k_n^4B_n = \\ + & \frac{i\omega}{4g}\left(\sum_{l=1}^{n-1}\tilde{R}B_lB_{n-l}e^{i\int(k_l+k_{n-l}-k_n)dx} + 2\sum_{l=1}^{N-n}\tilde{S}B_l^*B_{n+l}e^{i\int(k_{n+l}-k_l-k_n)dx}\right) \end{aligned} \tag{5.47}$$

Whereas before we defined our velocity potential ϕ_α as:

$$\phi_\alpha = \sum_{n=1}^{N}\frac{B_n}{2}e^{i(\int k_n dx - n\omega t)} + c.c. \tag{5.48}$$

where B_n was complex, here we use the alternative definition:

$$\phi_\alpha = \sum_{n=1}^{N} -i\frac{b_n'}{2}e^{i(nKx - n\omega t)} + c.c. \tag{5.49}$$

where K is the wave number including amplitude effects and b_n''s are real. This is related to B_n by:

$$B_n = -ib_n'e^{i(nKx - \int k_n dx)} \tag{5.50}$$

Substituting this into Equation (5.47) and neglecting the $b_{n,x}'$ yields:

$$\left[\frac{n^2\omega^2}{g} - \left(h + \frac{n^2\omega^2h^2\alpha}{g}\right)k_n^2 - 2\left(h + \frac{n^2\omega^2h^2\alpha}{g}\right)k_n(nK - k_n)\right.$$

$$\begin{aligned} &+ \quad 4k_n^3h^3\left(\alpha+\frac{1}{3}\right)(nK-k_n)+\left(\alpha+\frac{1}{3}\right)h^3k_n^4\Big]\, b'_n \\ &- \quad \frac{\omega}{4g}\left(\sum_{l=1}^{n-1}\tilde{R}b'_lb'_{n-l}-2\sum_{l=1}^{N-n}\tilde{S}b_l^{*\prime}b'_{n+l}\right)=0 \end{aligned} \tag{5.51}$$

This gives us N equations, but since we still have $N+1$ unknowns (N number of amplitudes b'_n and K), we require one more equation. As with the permanent form solution to the simplified extended Boussinesq angular spectrum model, we use a condition on the wave height. First we write Equation (3.30) for a flat bottom and reduce it to one dimension:

$$\begin{aligned} A_n &= \frac{n\omega}{g}\left[i\left(1-\alpha k_n^2h^2\right)B_n-2k_nh^2\alpha B_{n,x}\right] \\ &+ \quad \frac{1}{4g}\left(\sum_{l=1}^{n-1}\tilde{R}'B_lB_{n-l}e^{i\int(k_l+k_{n-l}-k_n)dx}-2\sum_{l=1}^{N-n}\tilde{S}'B_l^*B_{n+l}e^{i\int(k_{n+l}-k_l-k_n)dx}\right) \end{aligned} \tag{5.52}$$

Then, similar to Equation (5.49), we use an alternative definition for the free surface η:

$$\eta=\sum_{n=1}^{N}\frac{a'_n}{2}e^{i(nKx-n\omega t)}+c.c. \tag{5.53}$$

This is related to A_n by:

$$A_n=a'_ne^{i(nKx-\int k_ndx)} \tag{5.54}$$

Substituting this and Equation (5.50) into Equation (5.52) gives:

$$a'_n=\frac{n\omega b'_n}{g}\left[1+\alpha h^2\left(k_n^2-2k_nnK\right)\right]-\frac{1}{4g}\left(\sum_{l=1}^{n-1}\tilde{R}'b'_lb'_{n-l}+2\sum_{l=1}^{N-n}\tilde{S}'b_l^{*\prime}b_{n+l}\right) \tag{5.55}$$

Using Equation (5.46), we can formulate our final equation:

$$\begin{aligned} H &= \\ 2 &\sum_{n=1,3,5\ldots}^{N}\frac{n\omega b'_n}{g}\left[1+\alpha h^2\left(k_n^2-2k_nnK\right)\right]-\frac{1}{4g}\left(\sum_{l=1}^{n-1}\tilde{R}'b'_lb'_{n-l}+2\sum_{l=1}^{N-n}\tilde{S}'b_l^{*\prime}b_{n+l}\right) \end{aligned} \tag{5.56}$$

Thus we use Equations (5.51) and (5.56) as our system of $N+1$ equations, to be solved using a Newton-Raphson technique for the unknowns b_n' and K given wave height, water depth and wave period. This gives us the amplitudes of the velocity potential ϕ_α and the nonlinearly-distorted wave number K required to allow all harmonics to move at the same speed. The corresponding free surface amplitudes a_n' can be found from Equation (5.55).

One potential difficulty that may arise is the lack of convergence of the solution for a particular set of input conditions. In many cases, the equations become stiff and difficult to solve. In these cases a global iteration is done. In order to achieve a permanent form solution for a particular wave height for which the Newton-Raphson method may be problematic, we at first choose a lower wave height, allow this to converge, and then use the amplitudes and wave number found for this case as input for solving the equations again for a slightly larger wave height. This is done until the solution for the desired wave height is found. We will discover, however, that using an iterated wave condition into the corresponding model can lead to instabilities, since the model, which shares the same interaction coefficients as the permanent form solution and thus the same stiffness, cannot be iterated in the same manner.

5.5 Summary

In this chapter, we discussed the recasting of our fully nonlinear extended Boussinesq model into the angular spectrum format. In this format, we incorporated the additional assumption of longshore periodicity, thereby decomposing our two-dimensional time-periodic equations into an entire gridwork of coupled first-order differential equations, one for each frequency and longshore wave number mode.

Before applying this technique to the fully nonlinear extended Boussinesq equations, we wished to see what effect improved dispersion characteristics have on the leading order quantities of the angular spectrum model of Kirby (1990), which is a Fourier domain decomposition of the standard Boussinesq equations of Peregrine (1967). We simply replaced the shoaling and dispersion terms with ones that reflect the characteristics of the dispersion relation associated with the fully nonlinear extended Boussinesq equations. Nonlinear terms were left unchanged. The result, Equation (5.12), is our simplified angular spectrum model of the extended Boussinesq equations.

We also applied the angular spectrum technique directly to the equations. This was done on the argument that the simplfied model, while incorporating improved dispersion characteristics on the linear side, is inconsistent since the nonlinear terms are nondispersive. We obtained two time-periodic, longshore-periodic equations for each frequency and longshore wave number mode, one for the amplitudes of the velocity potential ϕ_α (Equation 5.29) and one for the free surface elevation η (Equation 5.39). This system of equations is solved for the amplitudes of ϕ_α first, and these amplitudes used to calculate amplitudes of η. This is our full angular spectrum model of the fully nonlinear extended Boussinesq equations.

For the data-model comparisons to be shown in the next chapter, we require a permanent form solution of these equations. When input into the model from which it was derived, the solution will propagate through a domain of constant depth without change in form. We derived two sets of equations for the permanent form solution, one for the simplified angular spectrum model and one for the full angular spectrum model. We also discussed a methodology for incrementally approaching a solution for a specific set of wave height, water depth and wave period conditions if these conditions caused the system of equations to become too stiff to converge.

Chapter 6

COMPARISONS TO DATA - ANGULAR SPECTRUM MODELS

6.1 Introduction

As was done in Chapter 4, we will compare our models to experimental data. We will also compare them to models which have been addressed in the literature. The purpose of this simulation is to demonstrate the advantages of an angular spectrum formulation over a small-angle parabolic format when modeling waves approaching at large angles to the x direction.

6.2 Comparison of Parabolic and Angular Spectrum Models to Hammack et al. (1990)

6.2.1 Introduction

Hammack et al. (1990) investigated the phenomenon of Mach stem reflection caused by cnoidal waves impinging on a vertical wall. They used a multi-directional wave paddle to generate a permanent form cnoidal wave train at various angles. The experimental layout is shown in Figure (6.1). The constant water depth in the experiment was 20 *cm*. Table 6.1 shows the gage locations with

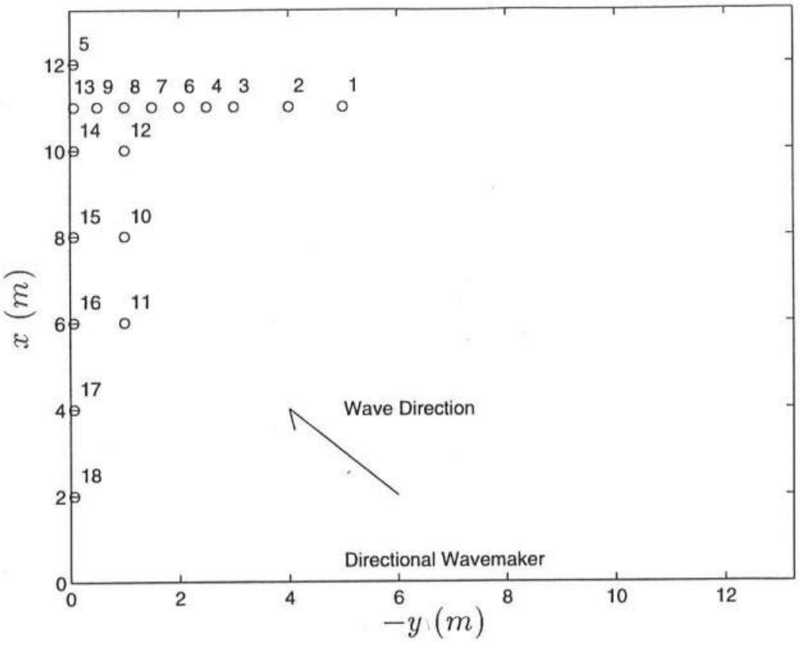

Figure 6.1: Tank And Gage Layout for Experiment of Hammack et al. (1990)

respect to a coordinate system shown in Figure 6.1. Most of the details of the experiment can be found in Hammack et al. (1990) and Kirby (1990), who compared his angular spectrum model of the standard Boussinesq equations (Equations 1.4 and 1.5) to this data. We will concentrate on the more relevant points of the experimental setup. Hammack et al. (1990) used the wave generation algorithm of Goring and Raichlen (1980) to generate cnoidal waves in one dimension. This was done to ascertain the characteristics of the wave and to determine whether adjustments should be made in the experimental setup in the case of oblique incidence. It was found that the nominally 4 *cm* high wave actually had a maximum crest elevation closer to 3.3 *cm*. The wave period was 1.478 *s*. Oblique incidence was simulated by phase lagging the adjacent paddles. This phase shift angle, Λ, is related to the directed wave angle Ψ by (Kirby 1990):

$$\Psi = \arcsin\left(\frac{\Lambda L}{360W}\right) \tag{6.1}$$

where L is the wavelength and W is the width of the individual wave paddles

Table 6.1: Gage Locations of Mach Stem Reflection Experiments of Hammack et al. (1990).

gage	x (m)	y (m)	gage	x (m)	y (m)	gage	x (m)	y (m)
1	11	-5	7	11	-1.5	13	11	-0.07
2	11	-4	8	11	-1	14	10	-0.07
3	11	-3	9	11	-0.5	15	8	-0.07
4	11	-2.5	10	8	-1	16	6	-0.07
5	12	-0.07	11	6	-1	17	4	-0.07
6	11	-2	12	10	-1	18	2	-0.07

comprising the directional wavemaker. For this experiment $W = 45$ cm. Phase angles used in the experiment were $\Lambda = 14.5$, 22, 30, 38.5, 47.5, and 57.6 degrees. It was not determined whether the maximum crest elevation of 3.3 cm varied with wave direction; however, to attempt to account for the difference between the velocity of the wavemaker (which is moving along the x-coordinate) and the velocity of the generated wave (moving in the Ψ direction), we divide our input spectral amplitudes by $\cos\Psi$ when performing the model-data comparisons. Data were taken at the gage locations; each time series consisted of 1250 points sampled at 25 Hz. The gage array was arranged to measure the particular characteristics of the Mach stem reflection pattern near the wall located along $x = 0$. The gage array perpendicular to the reflecting wall measured the width of the Mach stem pattern and any local wavefield structure generated as a consequence of this pattern. The gage array parallel to the wall measured the propagation characteristics of the Mach stem.

6.2.2 Comparison of Models to Mach Stem Experimental Data

We wished to compare both the parabolic models developed in Chapters 2 and 3, and the angular spectrum models discussed in Chapter 5, to this data. We also wished to compare the frequency domain parabolic KP model of Liu et al. (1985) (Equation 2.56) and the angular spectrum Boussinesq model of Kirby (1990) to this data, so that we may investigate the effects of improved dispersion on the data-model comparisons. In order to perform the comparisons, permanent form solutions were generated for each model using the techniques described in Section 5.4. The given input conditions for the permanent form solutions were: wave period $T = 1.478\ s$, water depth $h = 20\ cm$, and a maximum crest elevation $\eta_{max} = 3.3\ cm$. This last condition required some iteration, as different permanent form solutions would require different input waveheights to achieve the proper maximum crest elevation. Figure 6.2 shows the different permanent form solutions in the form of time series spanning two wave periods. It is noted here that the same permanent form solution was used for both the parabolic KP model and the angular spectrum Boussinesq model of Kirby (1990). It has been shown by Kirby (1991) that permanent form solutions of the same type as the KP and the angular spectrum model of Kirby (1990) in one dimension corresponds exactly to the solutions of the modified KdV equation:

$$\eta_t + c\eta_x - \frac{3}{2h}\eta\eta_t - \frac{h^2}{6c^2}\eta_{ttt} = 0 \tag{6.2}$$

Thus, we used this equation to generate the permanent form solution for both models.

After the solutions shown in Figure 6.2 were generated, we used the wavelengths associated with these solutions to calculate the directed wave angle Ψ by Equation 6.1. The calculated wave angles for the angular spectrum Boussinesq model of Kirby (1990) and the simplified extended Boussinesq angular spectrum

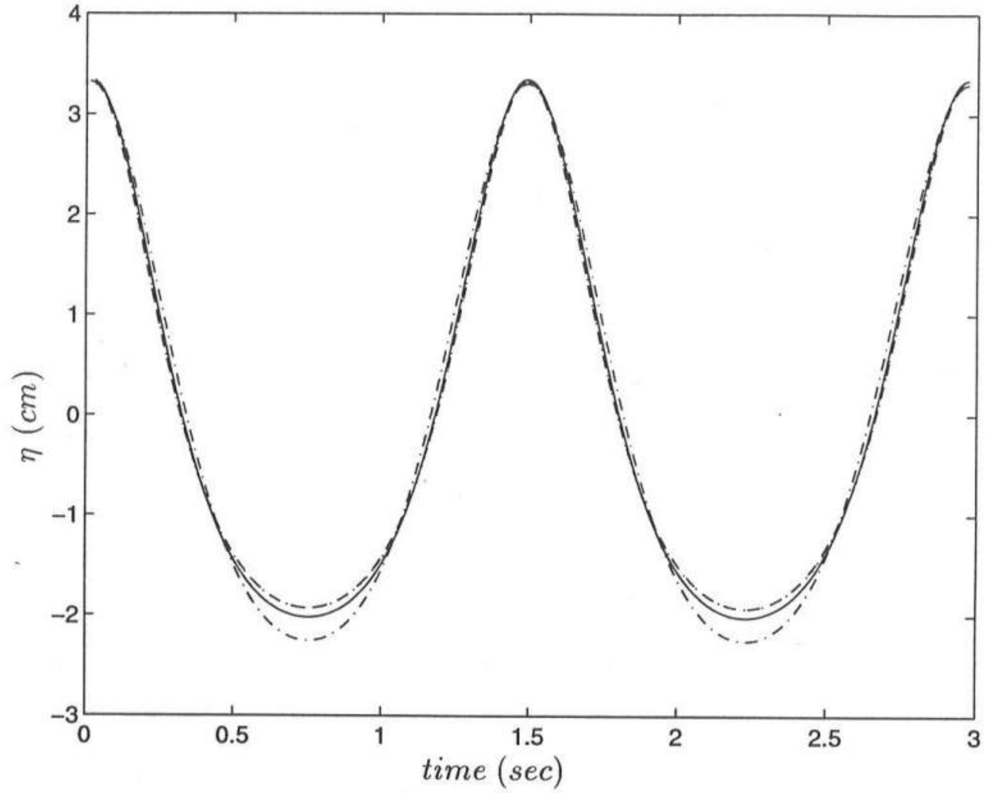

Figure 6.2: Comparison of Different Permanent Form Solutions for Input to Evolution Models: Permanent Form Solution to KP Model of Liu et al. (1985) (–); Permanent Form Solution to Fully Nonlinear Extended Boussinesq Equation of Chapter 3 (- -); Permanent Form Solution to Nonlinear Mild-Slope Equation of Chapter 2 (. .); Permanent Form Solution to Simplified Angular Spectrum Model of Extended Boussinesq Equation of Chapter 5 (-.).

model (Equation 5.12) are shown in Table 6.2. The wavelength L from the permanent form solution of Equation 6.2 was 1.9977 m, while that of the permanent form solution to Equation 5.12 was 1.9792 m. The wave angles used for the parabolic KP model of Liu, et al. (1985) are the same as those of the angular spectrum model of Kirby (1990). Unfortunately, both the parabolic model of the nonlinear mild-slope equation (Equation 2.55) and the parabolic model of the fully nonlinear extended Boussinesq equation (Equations 3.35 and 3.36) became numerically unstable for the given input conditions. One possible reason for this instability was the fact that the input conditions to generate the permanent form solutions to these models for this test had to be incrementally approached by gradual increases in waveheight. This process was described in Section 5.4. Because the interaction coefficients present in the permanent form solutions are the same as those of the corresponding model, the same degree of stiffness would be present. This stiffness, circumvented in the permanent form solutions by iteration with gradually increased waveheights as the target conditions are approached, cannot be dealt with in a similar manner in the model. It is hypothesized that this stiffness caused the numerical instability in both parabolic models. It is believed that the full angular spectrum model (Equations 5.29 and 5.39) would be similarly problematic, so it is eliminated as well. Thus, we used the parabolic KP model of Liu et al. (1985), the angular spectrum model of Kirby (1990) and the simplified extended model (Equation 5.12) in these comparisons.

For the parabolic KP model, reflective walls were placed at $x = 0$ m and $x = 13.25$ m. The spectral amplitudes from the permanent form solution and the wave angles Ψ corresponding to the paddle phase lag Λ in Table 6.2.2 were used to generate the amplitudes for oblique incidence along the boundary $x = 0$ m. Resolution for this simulation was $\Delta x = \Delta y = 0.0625$ m, and $N = 9$ frequency components were used. For the angular spectrum models, we used a mirror image

Table 6.2: Paddle Phase Angles Λ and Directed Wave Angles Ψ. Model 1 is Kirby (1990); Model 2 is Simplified Extended Boussinesq Angular Spectrum Model

Model	$\Lambda = 14.5°$	$\Lambda = 22°$	$\Lambda = 30°$	$\Lambda = 38.5°$	$\Lambda = 47.5°$	$\Lambda = 57.6°$
1	10.13	15.48	21.34	27.84	35.18	44.32
2	10.04	15.33	21.13	27.56	34.81	43.80

about $x = 0$, doubling the domain to $-13.25 \leq 0 \leq 13.25$ m. We computed the incident waveform as with the parabolic model, then Fourier transformed it over the domain and used the corresponding frequency-longshore wave number spectrum as input into the models. For these cases, we used $N = 9$ frequency components and $2M + 1 = 129$ longshore wave number components, thus making $M = 64$. The number of longshore wave number components used here insures that all freely propagating modes of the highest harmonics are kept. We again used a $\Delta x = 0.0625$ m. Model runs with more frequency components and finer resolution showed no significant improvement. We note here that for the angular spectrum models, we divided the resulting wave form generated by the spectral amplitudes and the wave angle Ψ by $\cos\Psi$, in order to compensate for any possible variation of the maximum crest elevation η_{max} from the acknowledged value of 3.3 cm as the angle increased. This was done as an attempt to improve upon the comparisons of Kirby (1990), who did not perform this adjustment and found the errors between data and model to increase with increasing wave angle, even though the angular spectrum format has no restrictions on wave angle. Similar compensation in the input to the parabolic KP model caused some instabilities in the solution, even after doubling the grid resolution, so we simulated the experimental conditions using this model without making this adjustment. It is unclear why these instabilities occurred, but we do not expect that this would invalidate the general conclusions drawn from this comparison.

6.2.3 Results

Figure 6.3 is a contour plot of the instantaneous free surface generated by the simplified extended Boussinesq angular spectrum model for the case $\Lambda = 14.5°$. The appearance of the Mach stem reflection area is evident near the left boundary. Figure 6.4 is another contour plot of the instantaneous free surface from the same model, in this case for $\Lambda = 57.6°$. The wave is approaching at such an oblique angle that it essentially radiates from the wavemaker as a short-crested wave. Pronounced diffraction effects can be seen near the right side of the figure.

We follow the procedure used by Kirby (1990) to perform the detailed data-model comparisons. First, we allowed a sufficient time to lapse in the experimental time series in order to establish nearly periodic motion. Then, a start time is established at the occurrence of a wave crest at Gage 13. We use this start time for all other gages as well. After recovering the time series from the spectral amplitudes in the model output, we mark a start time for the model time series with the occurrence of a crest at Gage 13. After these start times were established, time series of both data and model results were plotted for the gage array perpendicular to the wall (gages 13, 9, 8, 7, 6, 4, 3, 2 and 1) and parallel to the wall at $y = -0.07\ m$ (gages 18, 17, 16, 15, 14, 13 and 5). We will only show time series comparisons for the small phase angle ($\Lambda = 14.5°$) and the largest phase angle ($\Lambda = 57.6°$), as these results show the extremes in data-model agreement.

Figure 6.5 shows the comparison of data to the parabolic KP model of Liu, et al. (1985) for the transect perpendicular to the wall ($\Lambda = 14.5°$). The comparisons for each gage are offset by 10 *cm* so that the entire transect can be shown in one figure. This shows that, while agreement is good in general, the KP

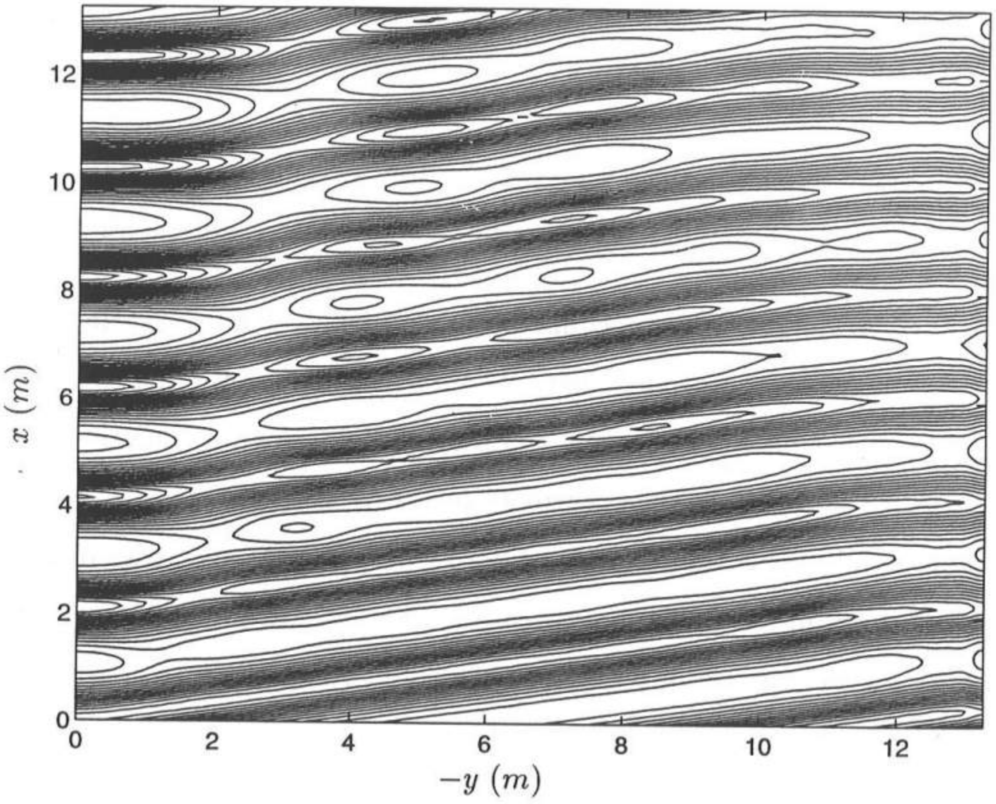

Figure 6.3: Contours of Instantaneous Free Surface Elevation, Simplified Extended Boussinesq Angular Spectrum Model, $\Lambda = 14.5°$.

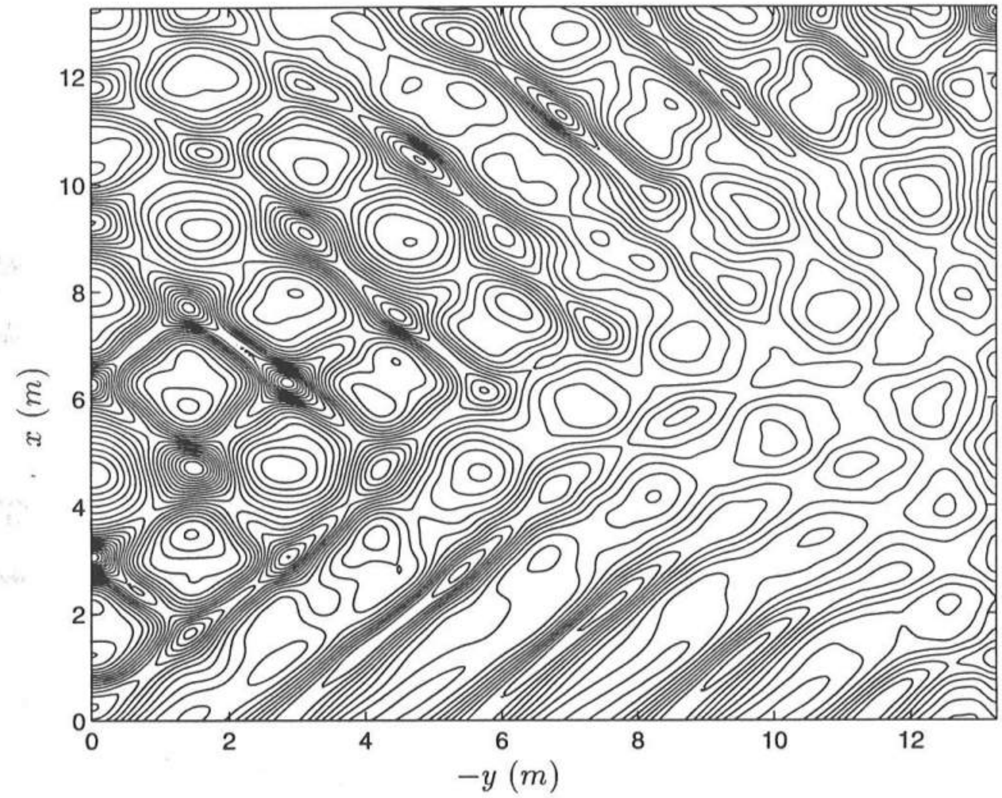

Figure 6.4: Contours of Instantaneous Free Surface Elevation, Simplified Extended Boussinesq Angular Spectrum Model, $\Lambda = 57.6°$.

model slightly overpredicts the width of the Mach stem. Figure 6.6 shows the KP model results for the gage array parallel to the wall. This shows the propagation characteristics of the Mach stem region; agreement to data is very good, though some phase error occurs at Gage 18. Figures 6.7 and 6.8 show the comparisons for the same case between the standard angular spectrum Boussinesq model of Kirby (1990) and the data for the gage arrays perpendicular and parallel to the reflecting wall, respectively. While the comparison between data and model for the gage array perpendicular to the wall is similar in agreement to that of the KP model, agreement is improved for the array parallel to the wall. Figures 6.9 and 6.10 show the same sort of comparisons for the same phase angle, with the model being the simplified extended Boussinesq angular spectrum model. Agreement to data for both gage arrays is similar to that of the parabolic KP model.

Figures 6.11 and 6.12 show model-data comparisons for the parabolic KP model of Liu et al. (1985) for the case $\Lambda = 57.6°$. This case would appear to violate the small-angle assumption inherent in the parabolic approximation. It is evident that the parabolic KP model compares relatively poorly to the data, with significant phase and amplitude errors. Figures 6.13 and 6.14 show the comparisons between the data and the angular spectrum model of Kirby (1990) for this phase angle. Not only are amplitude and phase predictions improved over the KP model, but even in the instances where the data and model match somewhat poorly much of the characteristic local features of the data is reflected in the model results. This can be seen, for example, in the Gage 2 comparison in Figure 6.13. Even with the phase error in the prediction of the crests, secondary crests in the troughs that are seen in the data are also captured by the model. In contrast, the Gage 2 comparison for the parabolic KP model (Figure 6.11) shows only a flat water surface with no crest structure whatsoever. Figures 6.15 and 6.16 show the comparisons to the simplified extended Boussinesq angular spectrum

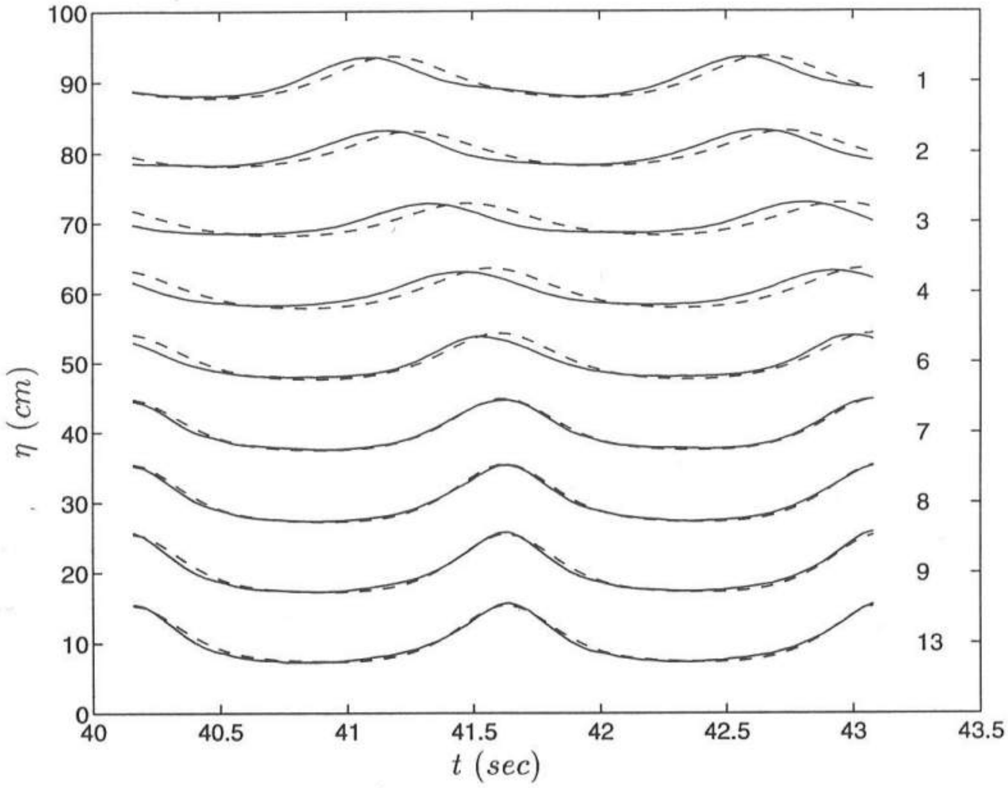

Figure 6.5: Comparisons of Parabolic KP Model of Liu et al. (1985) to Mach Stem Reflection Data, $\Lambda = 14.5°$. Gage Array Perpendicular to Wall. Numbers on Right Side are Gage Numbers. Data (–); KP Model (- -).

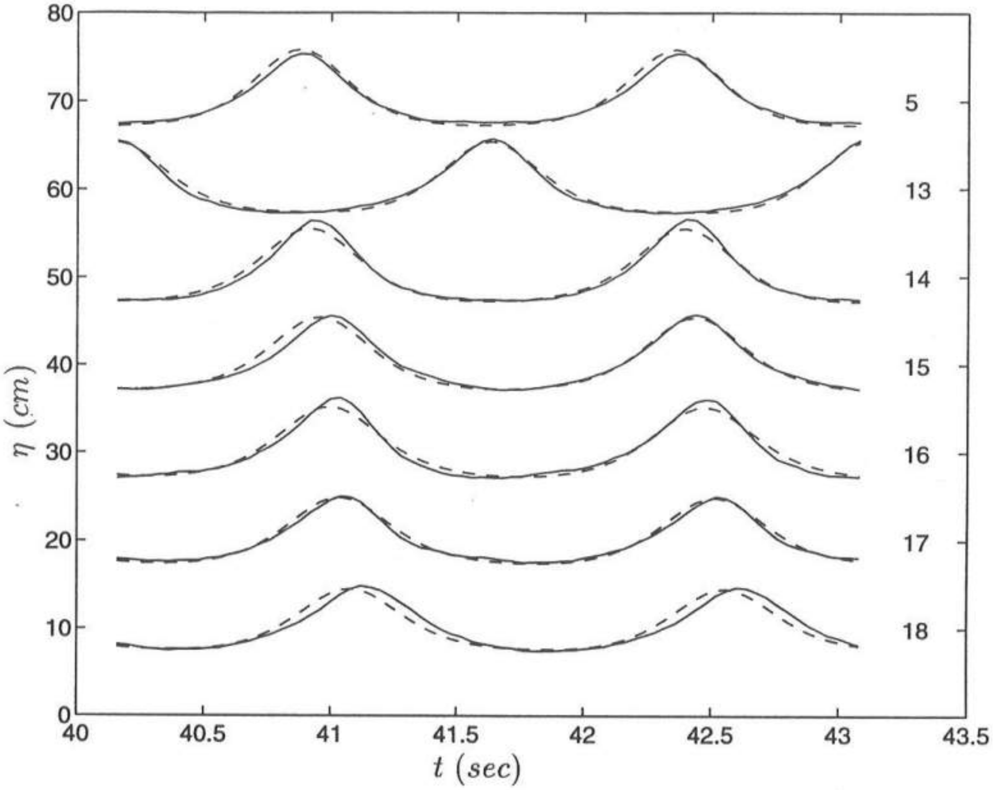

Figure 6.6: Comparisons of Parabolic KP Model of Liu et al. (1985) to Mach Stem Reflection Data, $\Lambda = 14.5°$. Gage Array Parallel to Wall. Numbers on Right Side are Gage Numbers. Data (–); KP Model (- -).

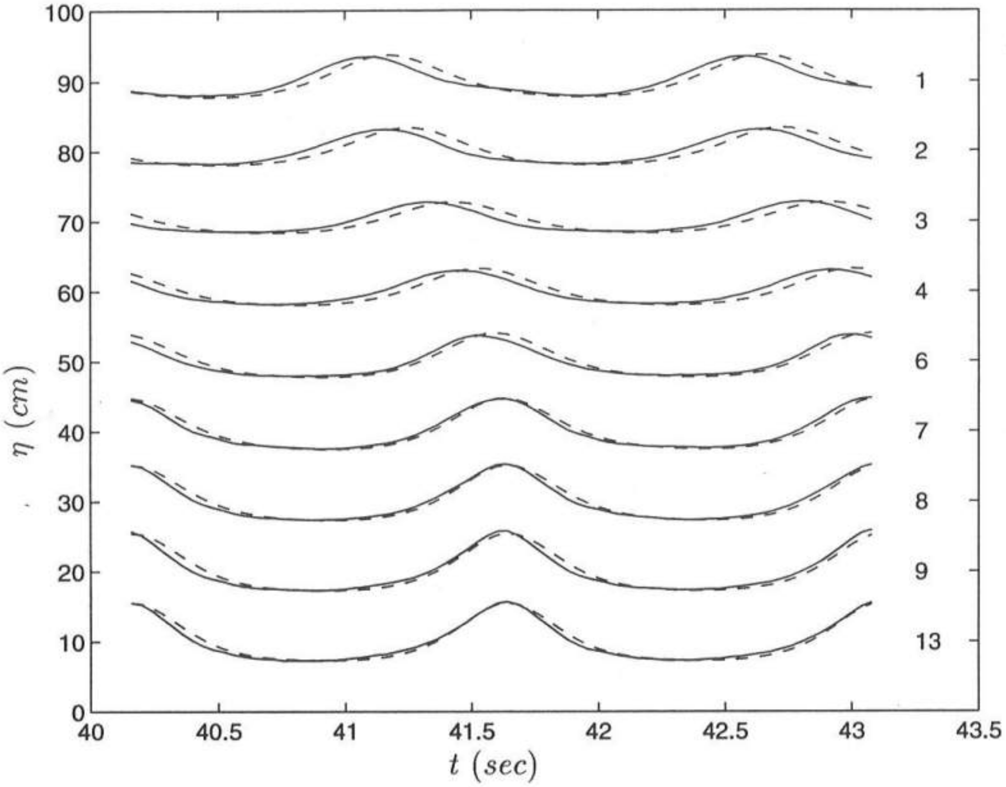

Figure 6.7: Comparisons of Angular Spectrum Boussinesq Model of Kirby (1990) to Mach Stem Reflection Data, $\Lambda = 14.5°$. Gage Array Perpendicular to Wall. Numbers on Right Side are Gage Numbers. Data (–); Angular Spectrum Model of Kirby (1990) (- -).

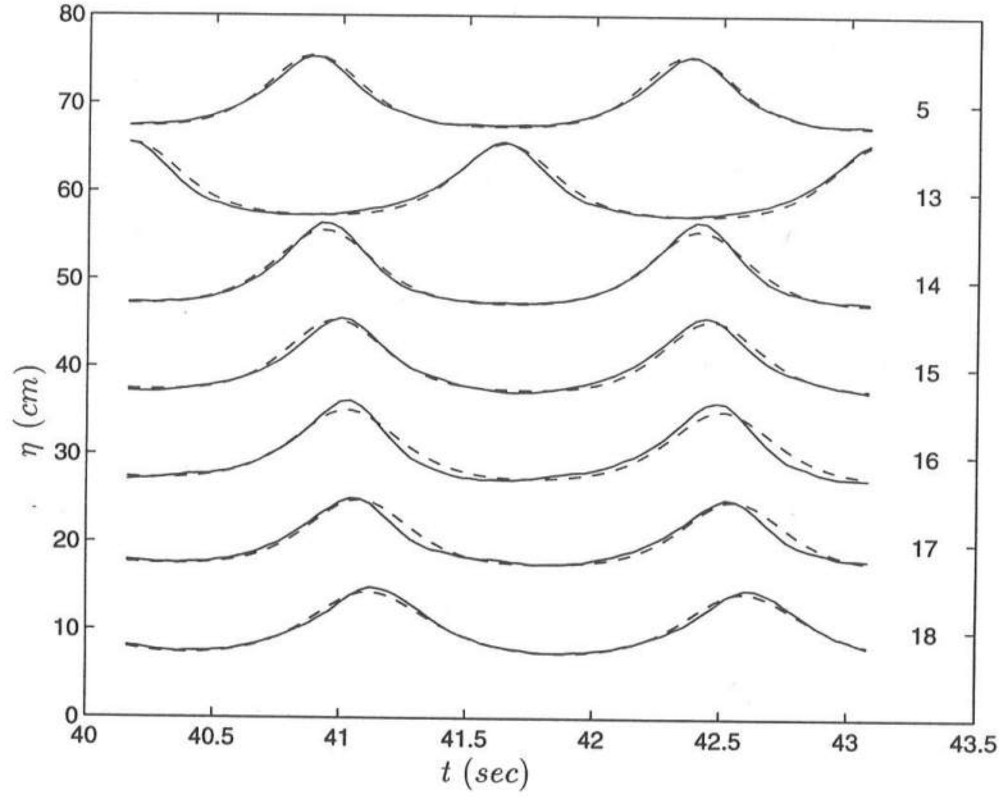

Figure 6.8: Comparisons of Angular Spectrum Boussinesq Model of Kirby (1990) to Mach Stem Reflection Data, $\Lambda = 14.5°$. Gage Array Parallel to Wall. Numbers on Right Side are Gage Numbers. Data (–); Angular Spectrum Model of Kirby (1990) (- -).

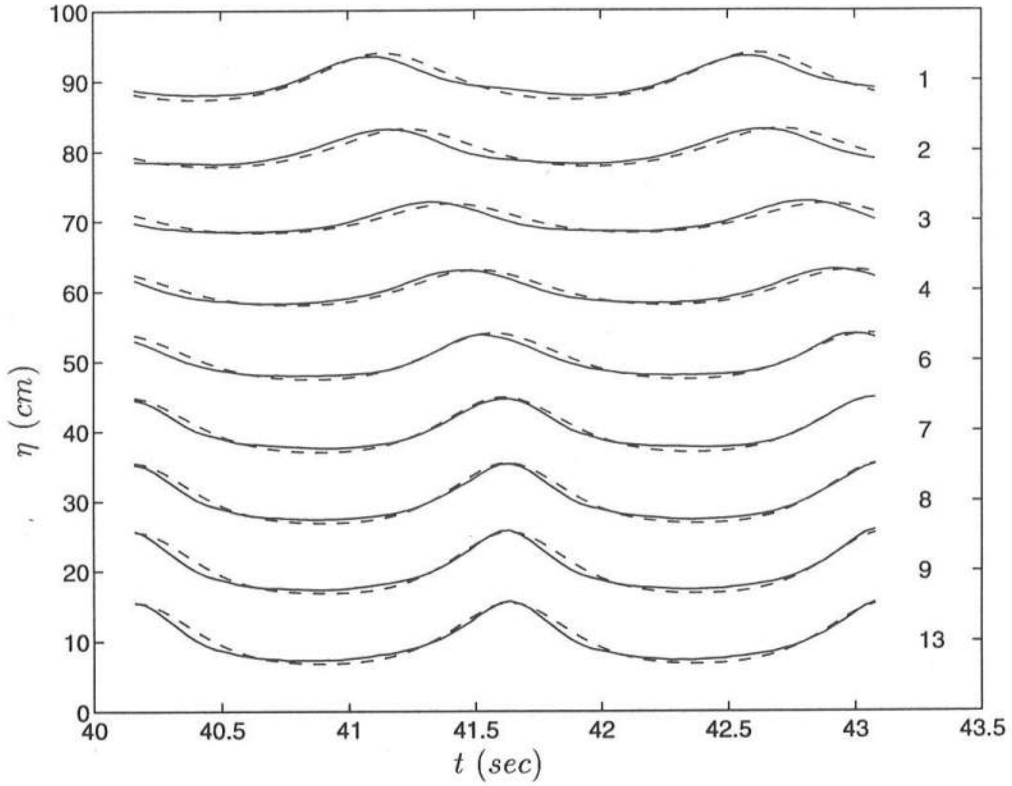

Figure 6.9: Comparison of Simplified Extended Boussinesq Angular Spectrum Model to Mach Stem Reflection Data, $\Lambda = 14.5°$. Gage Array Perpendicular to Wall. Numbers on Right Side are Gage Numbers. Data (–); Simplified Extended Boussinesq Angular Spectrum Model (- -).

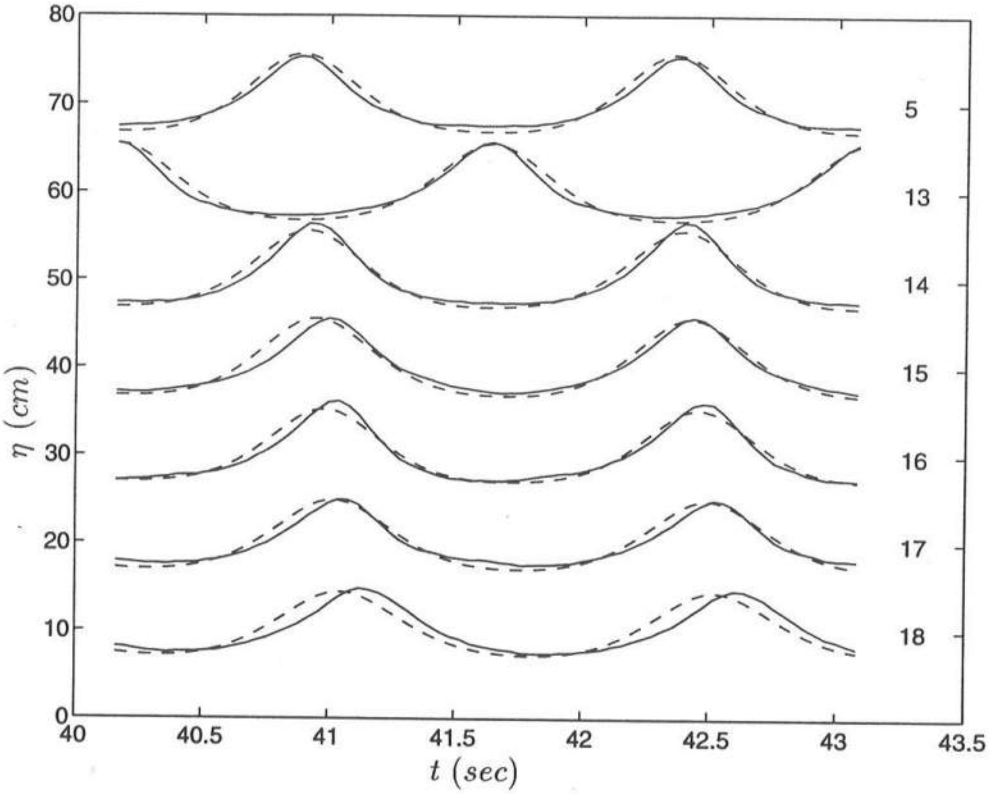

Figure 6.10: Comparison of Simplified Extended Boussinesq Angular Spectrum Model to Mach Stem Reflection Data, $\Lambda = 14.5°$. Gage Array Parallel to Wall. Number on Right Side are Gage Numbers. Data (–); Simplified Extended Boussinesq Angular Spectrum Model (- -).

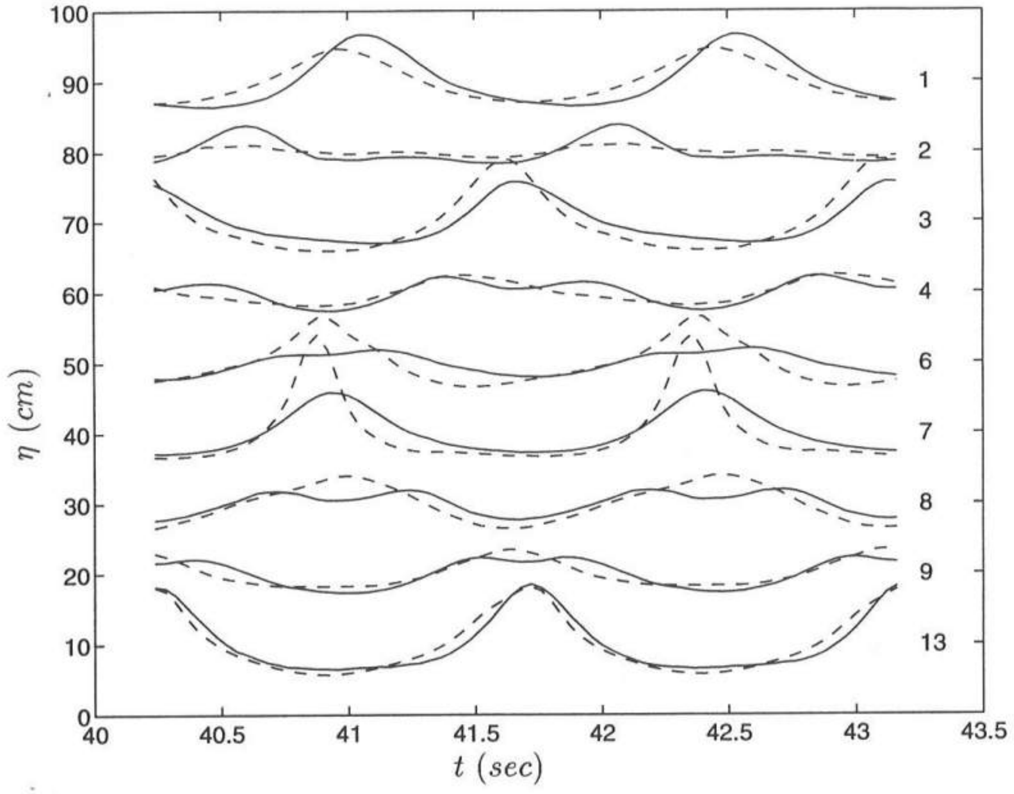

Figure 6.11: Comparisons of Parabolic KP Model of Liu et al. (1985) to Mach Stem Reflection Data, $\Lambda = 57.6°$. Gage Array Perpendicular to Wall. Numbers on Right Side are Gage Numbers. Data (–); KP Model (- -).

model. The model predicts the phase and amplitudes of the wavefield very well for the gage array perpendicular to the wall (Figure 6.15). Errors in the prediction of amplitude and phase are somewhat more pronounced in the array parallel to the wall (Figure 6.16) than they are in the comparison for the angular spectrum model of Kirby (1990) (Figure 6.14). Overall, however, it can be concluded that, for this large-angle case, the two angular spectrum models perform better than the parabolic KP model in simulating the Mach stem phenomena.

Though we have only shown the case for the smallest and largest Λ, we in

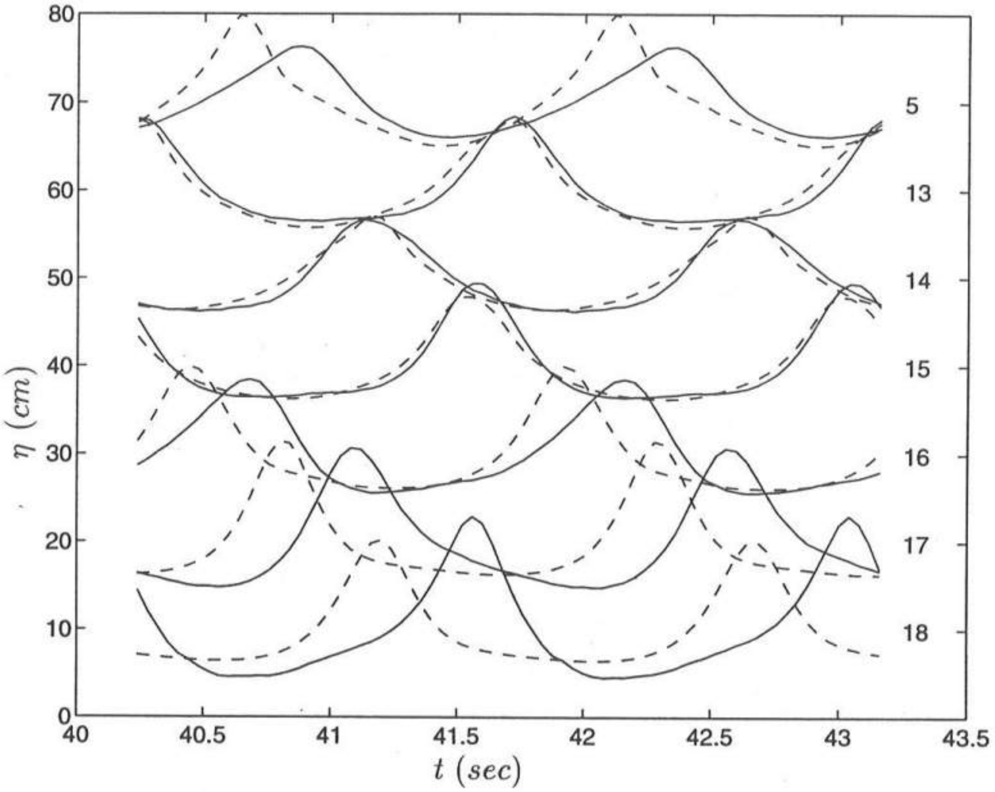

Figure 6.12: Comparisons of Parabolic KP Model of Liu et al. (1985) to Mach Stem Reflection Data, $\Lambda = 57.6°$. Gage Array Parallel to Wall. Numbers on Right Side are Gage Numbers. Data (–); KP Model (- -).

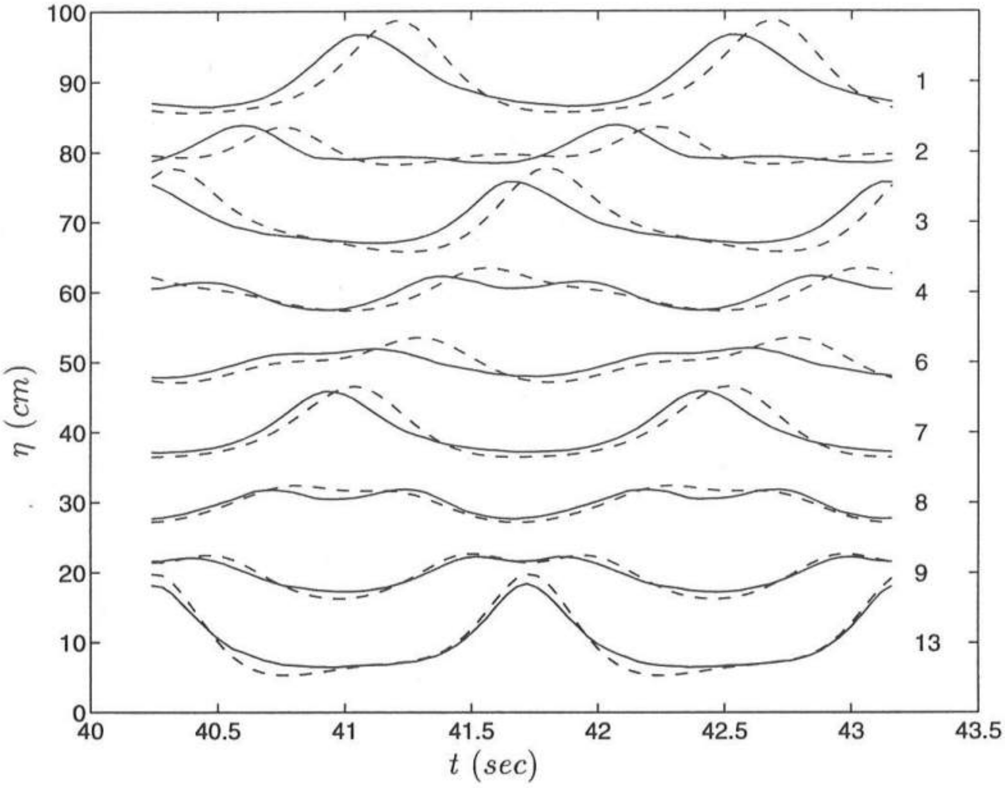

Figure 6.13: Comparisons of Angular Spectrum Boussinesq Model of Kirby (1990) to Mach Stem Reflection Data, $\Lambda = 57.6°$. Gage Array Perpendicular to Wall. Numbers on Right Side are Gage Numbers. Data (–); Angular Spectrum Model of Kirby (1990) (- -).

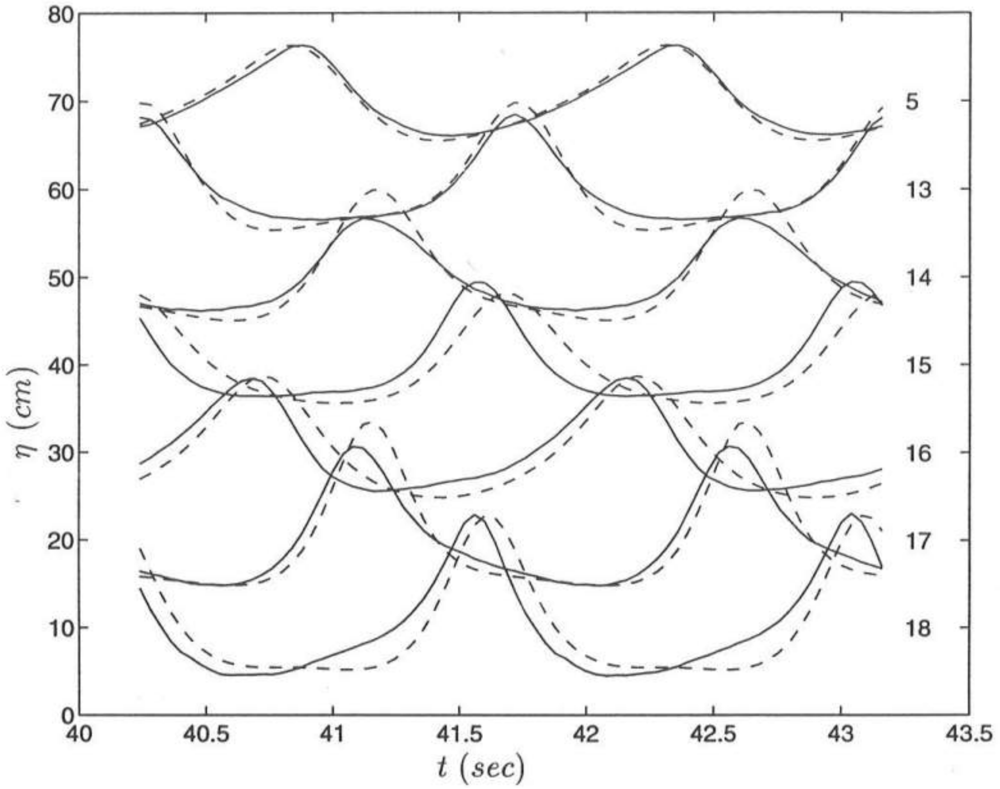

Figure 6.14: Comparisons of Angular Spectrum Boussinesq Model of Kirby (1990) to Mach Stem Reflection Data, $\Lambda = 57.6°$. Gage Array Parallel to Wall. Numbers on Right Side are Gage Numbers. Data (–); Angular Spectrum Model of Kirby (1990) (- -).

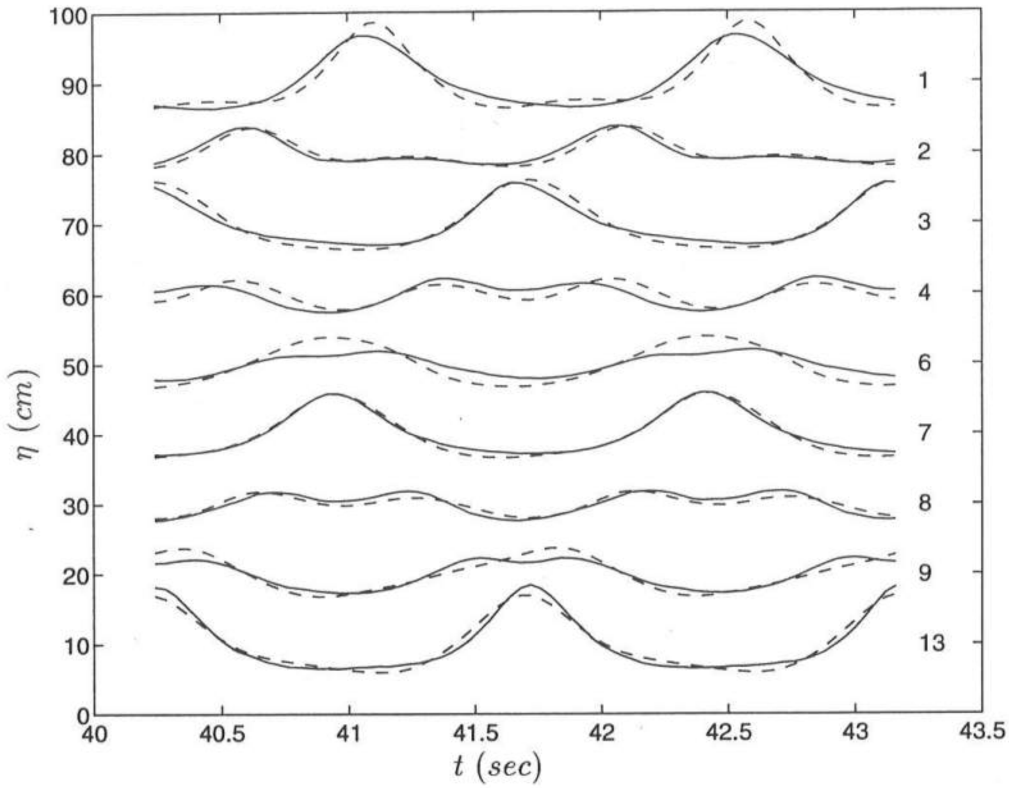

Figure 6.15: Comparisons of Simplified Extended Boussinesq Angular Spectrum Model to Mach Stem Reflection Data, $\Lambda = 57.6°$. Gage Array Perpendicular to Wall. Numbers on Right Side are Gage Numbers. Data (–); Simplified Extended Boussinesq Angular Spectrum Model (- -).

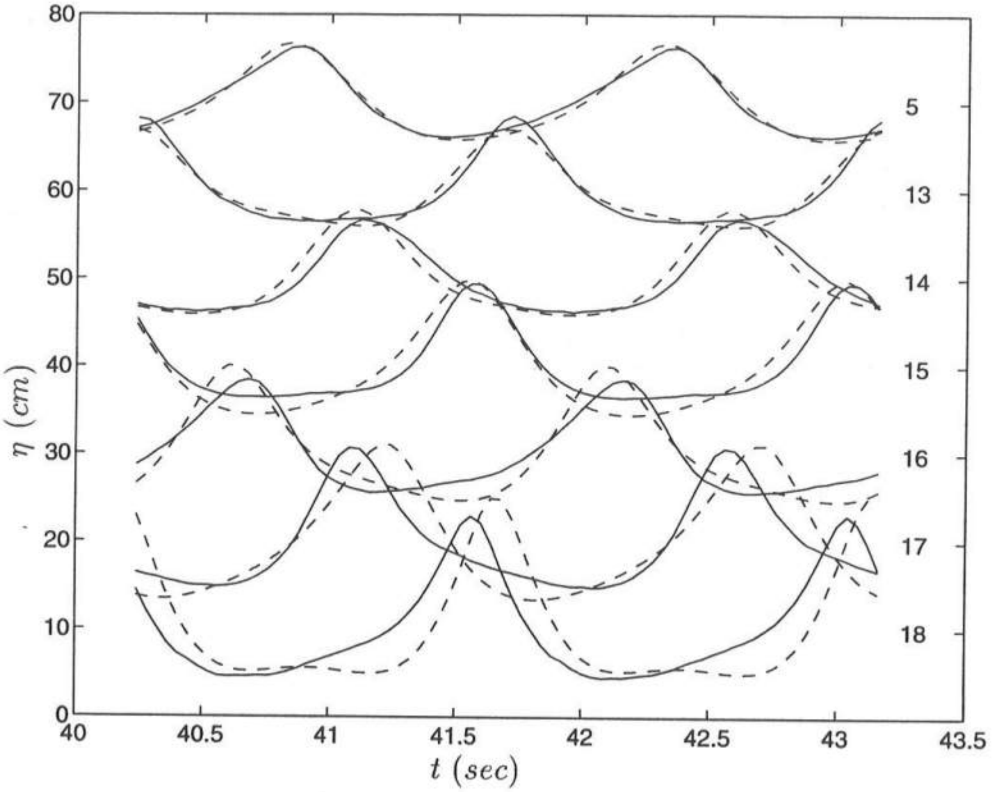

Figure 6.16: Comparisons of Simplified Extended Boussinesq Angular Spectrum Model to Mach Stem Reflection Data, $\Lambda = 57.6°$. Gage Array Perpendicular to Wall. Numbers on Right Side are Gage Numbers. Data (–); Simplified Extended Boussinesq Angular Spectrum Model (- -).

fact did use all three models to simulate all six phase angles. Rather than discuss every case generated by every model, we wish instead to quantify the amount of data-model agreement. We make use of correlation measures between data and model results at each of the nine gages located on the array perpendicular to the wall. We use the following definition of gage correlation:

$$\rho'_j = \frac{C_{12,j}}{\sigma_{1,j}\sigma_{2,j}} \tag{6.3}$$

where the subscript 1 refers to the data, 2 refers to the model in question, and the subscript j indexes the gages used and shown in the comparisons ($j = 1, ..., 9$) for the gage array perpendicular to the wall. It should be noted that the subscript j is not the gage number as denoted in the previous comparisons. Gage 13 corresponds to $j = 1$, and gage 1 corresponds to $j = 9$. The covariance $C_{12,j}$ and the individual standard deviations $\sigma_{1,j}$ and $\sigma_{2,j}$ are defined as follows:

$$C_{12,j} = \frac{1}{I}\sum_{i=1}^{I}\eta_{1,j}(i)\eta_{2,j}(i) \tag{6.4}$$

$$\sigma_{l,j} = \sqrt{\frac{1}{I}\sum_{i=1}^{I}\eta_{l,j}(i)\eta_{l,j}(i)} \quad l = 1, 2 \tag{6.5}$$

where $i = 1, ..., I$ is the index for the discrete time series over two wave periods, the same condition shown in Figures 6.5 through 6.16. We then compute an average correlation $\overline{\rho'}$:

$$\overline{\rho'} = \frac{1}{9}\sum_{j=1}^{9}\rho'_j \tag{6.6}$$

The values of correlation coefficients for the data-model comparisons are shown in Tables 6.3 through 6.5. Table 6.3 details the correlations between data and model for the parabolic KP model of Liu et al. (1985). Because we were unable to adjust for the possible variation of η_{max} with phase angle, as we did with the other two models we ran, strict comparison of correlation coefficients between the

Table 6.3: Correlation Coefficients ρ' (Each Gage and Average) for Parabolic KP Model Runs

Λ	13	9	8	7	6	4	3	2	1	average
14.5	.994	.992	.997	.996	.959	.854	.760	.873	.924	.928
22.0	.984	.950	.923	.893	.807	.524	.742	.931	.523	.809
30.0	.978	.986	.971	.961	.033	.992	.933	.859	.945	.856
38.5	.999	.972	.892	-.644	.952	.839	.871	.703	.901	.701
47.5	.889	.914	-.516	.894	.929	.873	-.658	.938	.870	.570
57.6	.966	.852	.814	.852	.729	.790	.903	.944	.866	.858

parabolic and angular spectrum models may not be applicable. Figure 6.17 shows the average correlation $\overline{\rho'}$ tabulated in Tables 6.3 through 6.5 plotted against Λ. It appears that, except for the rather anomalous increase in correlation for $\Lambda = 57.6°$, the parabolic model correlations fall off dramatically, even for the small-angle cases, where the effect of not dividing by $\cos\Psi$ is not strong. The last increase in correlation may be due to the fact that the standard correlation coefficient ρ' is lower for cases of equal amplitude but slight phase differences than for cases of almost zero phase difference and high amplitude differences. This can be clearly seen by comparing Figure 6.12 to either Figure 6.14 or Figure 6.16. In the latter two figures the errors are primarily phasing errors, which are heavily penalized by the correlation coefficient estimate. On the other hand the parabolic KP model prediction shows the proper phasing but strong deviation in the amplitudes, an error treated lightly by the correlation coefficient estimate. Thus the average correlation coefficient for the parabolic KP model at $\Lambda = 57.6°$ may not present the true picture. Thus, using both the values in Tables 6.3 through 6.5 as well as the direct comparisons to data for the case $\Lambda = 57.6°$ shown in Figures 6.11 through 6.16, we can conclude that the angular spectrum format performs better than the parabolic formulation when modeling oblique incidence.

Table 6.4: Correlation Coefficients ρ' (Each Gage and Average) for Angular Spectrum Boussinesq Model of Kirby (1990).

Λ	13	9	8	7	6	4	3	2	1	average
14.5	.989	.980	.986	.986	.965	.923	.882	.904	.937	.950
22.0	.962	.941	.946	.937	.932	.856	.978	.820	.920	.921
30.0	.969	.953	.980	.987	.881	.987	.988	.988	.993	.969
38.5	.971	.787	.750	.860	.953	.904	.839	.847	.960	.875
47.5	.968	.990	.880	.996	.997	.962	.827	.978	.952	.949
57.6	.991	.980	.927	.922	.672	.768	.802	.531	.833	.825

Table 6.5: Correlation Coefficients ρ' (Each Gage and Average) for Simplified Extended Boussinesq Angular Spectrum Model

Λ	13	9	8	7	6	4	3	2	1	average
14.5	.988	.983	.992	.991	.979	.956	.927	.933	.980	.970
22.0	.958	.924	.904	.906	.914	.865	.935	.990	.853	.916
30.0	.944	.960	.994	.958	.570	.946	.935	.946	.932	.910
38.5	.978	.973	.816	.744	.988	.977	.969	.971	.965	.931
47.5	.971	.945	.832	.907	.792	.624	.677	.833	.913	.832
57.6	.982	.939	.921	.993	.932	.744	.984	.958	.959	.935

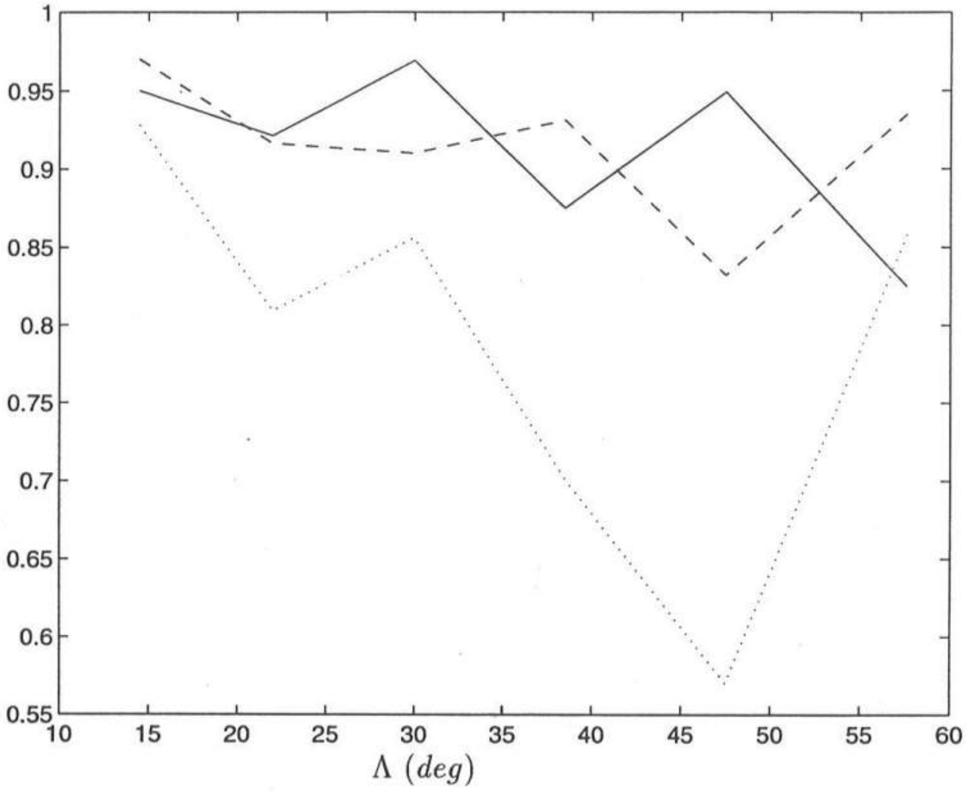

Figure 6.17: Comparison of $\overline{\rho'}$ for Three Models: Angular Spectrum Boussinesq Model of Kirby (1990) (–); Simplified Extended Boussinesq Angular Spectrum Model (- -); Parabolic KP Model of Liu et al. (1985) (. .).

Our final task of this chapter is to determine which of the angular spectrum models matches the Mach stem data best. Figure 6.17 does not quite answer this question, since it appears that there is no trend concerning the correlation coefficient $\overline{\rho'}$ with either model as the angle widens, though both have better correlations than the parabolic model save for the anomalous last angle. To independently check this result, we use a measure of root-mean-square error (Kirby 1990):

$$e_{j,rms} = \sqrt{\frac{\frac{1}{I}\sum_{i=1}^{I}(\eta_{2,j}(i) - \eta_{1,j}(i))^2}{\frac{1}{I}\sum_{i=1}^{I}(\eta_{1,j}(i))^2}} \tag{6.7}$$

for each gage. It is apparent that the normalization is with respect to the data variance. We note also that this is an unbounded error measure, and *not* percentage error, though we can remark that a value of $e_{rms} = 0$ is no error and $e_{rms} = 1$ can imply no theory ($\eta_{2,j} = 0$). An interesting feature of this error measure is that if $\eta_{2,j}$ and $\eta_{1,j}$ were both random uncorrelated signals with the same variance, the error measure would reduce to $\sqrt{2}$. This is not its maximum value, since it is likely that the error could climb above this value were the variances of the signals different. It is best to simply interpret the size of this value; a lower e_{rms} would indicate better data-model agreement. We also define a composite error $\overline{e_{rms}}$ by adding the root-mean-square error for all times and all gages and dividing the sum by the total standard deviation for all times and all gages. Table 6.6 shows the errors for the angular spectrum Boussinesq model of Kirby (1990), and Table 6.7 shows the same for the simplified extended Boussineq angular spectrum model. Figure 6.18 is a plot of the variation of $\overline{e_{rms}}$ with the paddle phase angle Λ. As with the correlation coefficients, there seems to be no clear indication that the simplified extended Boussinesq angular spectrum model is an improvement over the angular spectrum Boussinesq model of Kirby (1990), though this may be a consequence of the fact that the experiment was carried out in fairly shallow water ($\frac{h}{L_0} = 0.06$), so the benefit of improved dispersion is

Table 6.6: Root-Mean-Square Error e_{rms} (Each Gage and Average) for Angular Spectrum Boussinesq Model of Kirby (1990)

Λ	13	9	8	7	6	4	3	2	1	average
14.5	.152	.207	.169	.173	.286	.408	.490	.461	.391	.280
22.0	.277	.353	.351	.372	.405	.617	.432	.223	.606	.361
30.0	.307	.339	.220	.183	1.26	.273	.165	.157	.126	.271
38.5	.523	.702	.691	.782	.345	.545	.583	.778	.279	.564
47.5	.374	.321	.742	.217	.132	.275	.859	.304	.306	.304
57.6	.256	.328	.520	.472	1.07	.814	.817	.938	.712	.621

not evident. The general *trend*, however, seems to be a slight increase in error with an increase in angle of approach, independent of the individual oscillations present between different values of Λ. Though we have shown that these models are a clear improvement over standard parabolic modeling, it seems anomalous that this trend in the error is present, since there is no restriction on the angle of incidence. Moreover, comparison of Table 6.6 to Table 4 of Kirby (1990), where no accounting for possible variation of the input wave amplitude with increasing angle was done, reveals that the errors have actually worsened. It appears that accounting for the variation in $\eta_{\mathbf{max}}$ by dividing the input amplitudes by $\cos\Psi$ has not addressed this unknown effect properly. Perhaps what is most needed is a model-model comparison, whereby we would run a time-dependent Boussinesq model at the required angles and consider this to be the "data." We would then compare the results. In this manner we would not have to concern ourselves with any particular variation of wave heights with increasing angle.

Table 6.7: Root-Mean-Square Error e_{rms} (Each Gage and Average) for Simplified Extended Boussinesq Angular Spectrum Model

Λ	13	9	8	7	6	4	3	2	1	average
14.5	.206	.220	.185	.191	.257	.305	.377	.394	.324	.256
22.0	.381	.465	.478	.450	.452	.636	.397	.241	.560	.433
30.0	.468	.398	.222	.288	1.39	.538	.419	.324	.385	.412
38.5	.423	.304	.582	2.35	.598	.261	.282	.563	.274	.434
47.5	.297	.340	1.05	.565	.672	.852	1.41	.734	.538	.630
57.6	.194	.449	.418	.146	.989	.672	.262	.289	.327	.349

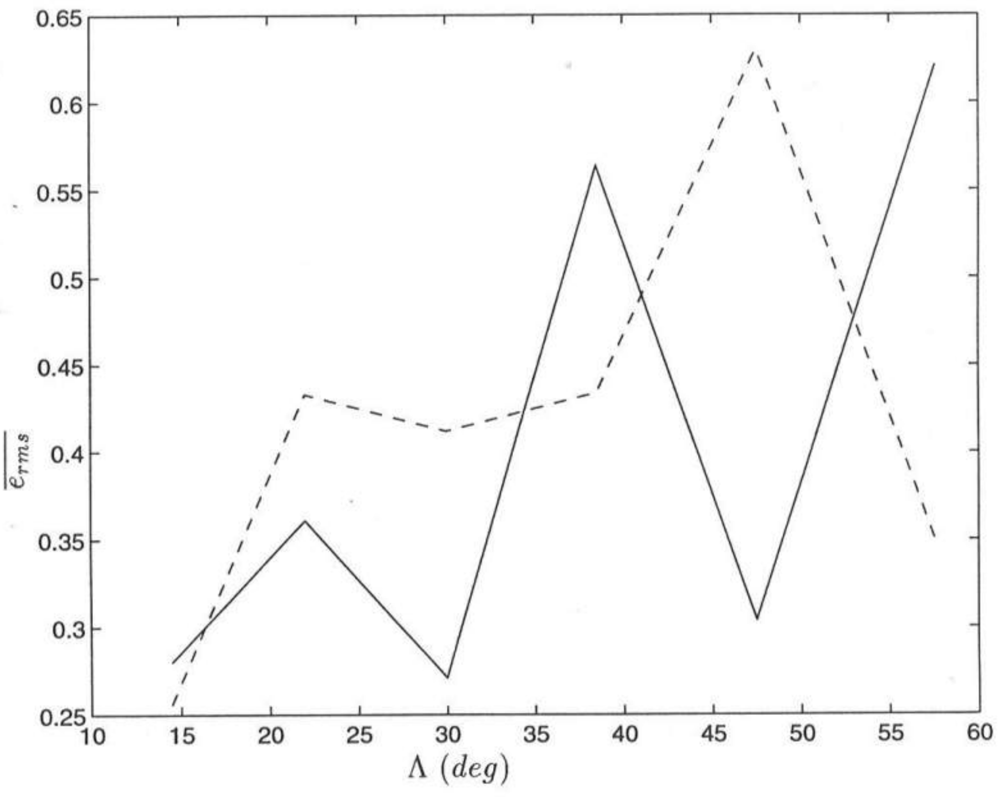

Figure 6.18: Comparison of $\overline{e_{rms}}$ for Angular Spectrum Models: Angular Spectrum Boussinesq Model of Kirby (1990) (–); Simplified Extended Boussinesq Angular Spectrum Model (- -).

6.3 Summary

We used the simplified extended Boussinesq angular spectrum model of Section 5.2 to compare to the Mach stem experiments of Hammack, et al. (1990). We also used the angular spectrum Boussinesq model of Kirby (1990) and the parabolic KP model of Liu et al. (1985) in this comparison. Unlike Kirby (1990), who did not account for any possible variation in η_{max} with increases in wave angle, we attempted to remedy this by dividing the incident wave amplitudes by $\cos\Psi$, where Ψ is the angle from wavemaker normal. This was not done for the parabolic KP model, since it exhibited some unexplainable numerical instability even after doubling the grid resolution. We showed several direct comparisons between data and model along gage array transects. These comparisons were for the smallest incident angle (paddle phase angle $\Lambda = 14.5°$) and the largest ($\Lambda = 57.6°$). It is clear that these angular spectrum models are an improvement over the parabolic KP model, which not only shows strong amplitude errors compared to the data for the large-angle case but also fails to capture much of the local wave shape structures evident in the data. We used a correlation coefficient to attempt to quantify the data-model comparisons. The result was summarized in Figure 6.17, which showed a clear decline in correlation between model and data for the parabolic KP model even at small angles, where the effect of not dividing the amplitudes by $\cos\Psi$ is not as evident as it may be for large angles. The last correlation coefficient for the KP model shows an anomalous increase, which is a peculiarity of the calculation of correlation; it appears that slight phasing errors are penalized heavily, while strong amplitude errors are not, thus the high correlation for the KP model at $\Lambda = 57.6°$. In contrast to this, the two angular spectrum models show relatively high correlation, though their general trend is to decline as the wave angle increases. In an attempt to distinguish between the angular spectrum model of Kirby (1990) and the simplified extended Boussinesq angular spectrum model, we defined a root-mean-square error between the model results and the data. This error calculation is unbounded, and should not be thought of as a percent error. Figure 6.18 summarized this analysis. There seemed to be no clear indication that the simplified extended Boussinesq angular spectrum model improved data-model comparisons with respect to the angular spectrum Boussinesq model of Kirby (1990). This may be due to the fact that the value of the depth parameter $\frac{h}{L_0}$ for this experiment was 0.06, which is fairly shallow water. Both showed a general trend of increasing error with increases in wave angle, an occurrence that the division of the amplitudes by $\cos\Psi$ actually worsened for the angular spectrum model of Kirby (1990) when comparison was made to his results, which were generated without this adjustment. Despite these qualifications, we can assert that the two angular spectrum models perform better in modeling oblique wave angles than the corresponding parabolic model. To provide a definitive account of the relative improvement of data-model comparisons we would need a similar experimental data set in deeper water than was used for this comparison.

We stated earlier that we eliminated the more dispersive parabolic models of Chapters 2 and 3, as well as the full angular spectrum model of the fully nonlinear extended Boussinesq equations of Chapter 5, from this simulation because of perceived problems with the stiffness of the equations used to generate their permanent form solutions for this experiment. Because these permanent form solutions have identical interaction coefficients to their respective models, any stiffness of the equations in the permanent form solution would likely also be present in the model itself. As stated before, this stiffness was overcome in the permanent form solutions by wave height iteration; no corresponding iteration technique is applicable for the models. However, due to the uncertain nature of quantifying data-model comparisons in the simulations of this experiment, it does not seem likely that using either the more dispersive parabolic models or the full angular spectrum model of Chapter 5 would result in dramatic improvement in the comparisons. What is actually needed for these more dispersive models is an experimental data set in deep enough water to demonstrate the advantages of improved dispersion, with wave characteristics that would cause no convergence problems in the permanent form solutions. Alternatively, we could also look at experimental simulations that require no permanent form solutions. We have already seen one such case in Chapter 4 (the experiment of Whalin 1971), but we could not use these angular spectrum models in that case because the bathymetry varied in the y (longshore) direction. There are several laboratory studies of nonlinear wave shoaling and refraction over a plane beach (Elgar et al. 1993; Elgar et al. 1992; Nwogu 1994), and at least one field study (Freilich et al. 1990). It is expected that simulation of these conditions would be be time consuming, because all that is known in any of these cases is the energy density (usually denoted $S(f,\theta)$) and no phase information, so that many realizations with random phases need to be simulated and averaged. Additionally, we have the expected problems with the linear shoaling characteristics of frequency domain models of the fully nonlinear extended Boussinesq equations, complications not alleviated by the full angular spectrum model of these same equations. Thus we end our discussion of angular spectrum model comparisons to data, with the expectation that future work will overcome many of these other difficulties.

Chapter 7

CONCLUSIONS AND SUGGESTIONS FOR FUTURE WORK

In this work we have detailed two different methodologies for modeling the propagation of weakly nonlinear water waves through water depths that may be outside the usual range of validity for standard shallow water predictive techniques. We developed these methodologies in the frequency domain, thereby formulating evolution equations for time-harmonic (and, in the case of the angular spectrum formulation, longshore-periodic) wave motion. These formulations have linear dispersive and shoaling properties which can be applied to regions outside shallow water.

The first approach, the formulation of a nonlinear mild-slope equation, yielded models with shoaling and dispersion mechanisms that are determined by full linear theory, thus extending the linear capabilities to areas outside shallow water. This was an advance on the work of Bryant (1973,1974), Keller (1988) and Agnon et al. (1993) in that the formulation involved two-dimensional irregular wave propagation over varying depth. We found, however, that we needed to restrict ourselves to water depths where the phase mismatch in the nonlinear terms remains small. Otherwise, the phase mismatch can oscillate at the same order as the wave itself, invalidating the slowly varying amplitude assumption. We developed both one-dimensional and parabolic two-dimensional models for comparison to data. For the one-dimensional model, we included a dissipation mechanism based on the work of Thornton and Guza (1983). We found that, overall, the nonlinear mild-slope model and its one-dimensional counterpart, the fully dispersive nonlinear shoaling model, compared very well to the data of Whalin (1971) and Mase and Kirby (1992). This indicates that the model is an excellent predictor of energy-based quantitites in spectral simulations. However, it performs less well when higher-order moments like skewness and asymmetry are compared to data. This is true even if the effects of spectral truncation are accounted for.

The second approach is the fully nonlinear extended Boussinesq equations of Kirby and Wei (1994), which is an extension of the work of Nwogu (1993) and Chen and Liu (1993). We developed it in both one-dimensional and parabolic two-dimensional forms, in terms of ϕ_α and η because this form was more convenient than deriving it in terms of $\mathbf{u}_\alpha$ and η due to the lack of an extra vector gradient operation. This was the approach taken by Chen and Liu (1993); our linear terms are exactly the same as theirs, but we retain dispersive effects in the nonlinear terms. The derivation of the frequency-domain model was consistent, but the linear shoaling term that resulted is extremely restrictive in its applicability to deep water. The two-dimensional parabolic form compared quite well to the laboratory data of Whalin (1971), but the one-dimensional model (which was equipped with the same dissipation mechanism as the fully dispersive nonlinear shoaling model) was far less successful when compared to the shoaling data of Mase and Kirby (1992). When analyzed for the frequency range of this data, we found that the linear shoaling mechanism of this model compared better to linear theory than Green's Law (the linear shoaling mechanism inherent in the consistent shoaling model of Freilich and Guza (1984)) for frequencies below the spectral peak ($\frac{h}{L_0} = 0.3$, which is intermediate water depth) . However, for frequencies above this peak, this linear shoaling model diverged rapidly from linear theory, incurring errors far above those exhibited by Green's Law for this range of frequencies. While the source of this behavior is unclear, we hypothesized that it may be due to the rational polynomial formulation of the dispersion relation. The shoaling terms in this model are essentially ratios of rational polynomials. When carried outside the range of calibration for the dispersion parameter α, these terms could behave somewhat unpredictably. This tendency was borne out in the direct data-model comparisons. The higher harmonics of this extended Boussinesq model were dramatically overpredicted compared to the data. This overshoaling was reflected in the statistics as well, as quantities such as skewness and asymmetry were poorly predicted. However, for frequencies below the peak, the model performed very well, better than the consistent model of Freilich and Guza (1984). It was thus recommended that a suitable deep water limit for the model for reliable predictions should be $\frac{h}{L_0} \leq 0.3$.

We also discussed linear shoaling models that were realizable from the $(\eta, \mathbf{u}_\alpha)$ version of the fully nonlinear extended Boussinesq equations. There was difficulty in developing these models, since the first-order substitutions necessary to obtain a wave equation were ambiguous, with each ambiguity leading to a very different shoaling model. We circumvented that problem with the use of a free parameter β, which was then "best-fit" to the shoaling term from linear theory. The resulting linear shoaling model compared very well with the shoaling characteristics of linear theory. Unfortunately, the ambiguous nature of the substitution affected the nonlinear terms as well, leading to different terms with potentially very different behavior. Unlike the linear terms, we did not have a benchmark model that we could "best-fit" a parameter to. The consistent nature of the derivation of the frequency-domain model in terms of ϕ_α and η was our primary motivation for using this form. We also emphasized that transforming a time-dependent equation into the frequency domain tends to be less than straightforward for dispersive models, and thus there may not be a direct correspondence between characteristics exhibited by the frequency-domain models and those of the time-domain models from which they were derived. Therefore, we cautioned against inferring time-domain model behavior from frequency-domain model results.

Despite this, we would still obtain a limited correspondence between the time-domain fully nonlinear extended Boussinesq model and its frequency-domain counterpart. Time-domain modeling makes no distinction between the nature of processes like shoaling, refraction, diffraction or nonlinear interactions. These characteristics *are* present in a time-domain model, but they are not explicit. In contrast, a corresponding frequency-domain model does make these processes obvious, so they can be studied individually. The nonlinear mild-slope equation does not have a convenient time-domain form; thus, we retain the frequency-domain fully nonlinear extended Boussinesq equation, being cognizant of the above-stated depth limitation. To obtain a model with no limitation on the angle of approach, we transformed the frequency domain fully nonlinear extended Boussinesq equations into the angular spectrum domain, where longshore periodicity was assumed. We developed two models within this format. The first was a simplified extended Boussinesq angular spectrum model, whereby we took the angular spectrum Boussinesq model of Kirby (1990) (which was an angular spectrum transformation of the Boussinesq equations of Peregrine 1967), and replaced the shoaling and dispersion terms to represent the dispersion properties of the extended Boussinesq equations while retaining lowest-order nonlinearity. We also developed a full angular spectrum treatment of the fully nonlinear extended Boussinesq equations. We also developed permanent form solutions of these models, since we wished to simulate the Mach stem reflection experiments of Hammack et al. (1990).

It was desired at first to simulate these experimental conditions with the parabolic Kadomstsev-Petviashvili (KP) model of Liu et al. (1985), the two parabolic models developed in this study, the angular spectrum Boussinesq model of Kirby (1990), the simplified extended Boussinesq angular spectrum model, and the full angular spectrum model. Unfortunately, the permanent form solutions of the nonlinear mild-slope equation and the frequency-domain fully nonlinear extended Boussinesq equations required global iteration on the waveheight to obtain the experimental input conditions. Upon operation of the parabolic models, instabilities were encountered that were not mitigated by increased grid resolution. This is possibly because the nonlinear coefficients, which are the same in the model as in the permanent form solution, caused the model equations to become too stiff and difficult to solve with these iterated wave conditions as input. We suspected the same would hold true for the full angular spectrum model of the fully nonlinear extended Boussinesq equations, since the input condition is shared with its parabolic counterpart. Thus, simulation of the experimental conditions of Hammack, et al. (1990) were performed using only the parabolic KP model of Liu et al. (1985), the angular spectrum Boussinesq model of Kirby (1990), and the simplified extended Boussinesq angular spectrum model. The results indicate that the two angular spectrum models perform better than the parabolic KP model as the angle increases. This conclusion was ascertained by defining a correlation coefficient between data and model, which, as it happened, heavily penalizes mismatches in phase with little discrepancy in amplitude, more so than strong discrepancies in amplitude with little phase error. This explains why the parabolic KP model achieved such a high correlation coefficient for the largest wave angle, when inspection of the direct time series comparisons reveal no small amount of amplitude discrepancy between model and data. Comparisons between the angular spectrum Boussinesq model of Kirby (1990) and the simplified extended Boussinesq angular spectrum model proved unrevealing, as it was not clear which model performed better for this experimental case. This may be due to the fact that the experiment took place in fairly shallow water ($\frac{h}{L_0} = 0.06$). A slight increasing trend in error with increases in wave angle was also noticed, which indicates that the attempt to modify the input conditions to account for variations with wave angle was not entirely successful.

In conclusion, we have attempted to overcome the limitations inherent in standard Boussinesq shallow water wave theory with these more dispersive models. One approach, that of the nonlinear mild-slope equation, seems to be fairly successful in the context of frequency domain modeling. The second approach, that of the frequency domain treatment of the fully nonlinear extended Boussinesq equations, is somewhat less successful due to the nature of its linear shoaling tendencies, but still works well when within its recommended depth limitation.

Future work could include rederiving the frequency domain model of the fully nonlinear extended Boussinesq equations by possibly obtaining a wave equation first (in the manner of the $(\eta, \mathbf{u}_\alpha)$ form of the time dependent equations), and then attempting to obtain an improved shoaling term, either by the use of a free parameter or by iterating the substitutions until a suitable shoaling term is found. On a more applications-oriented level, an area that requires addressing is in the use of these models in ascertaining physical processes. For example, the angular spectrum format is ideally suited for investigating interaction of waves propagating at different directions. Freilich et al. (1990) indicate that detuned non-colinear interactions between directional spectra approaching at distinct mean angles would yield a non-negligible effect on the evolution of the wavefield. They use their field data, which consisted of two directional wave spectra as the primary offshore feature, and indicate the presence of a third peak in the nearshore environment. This third peak, they maintain, was generated by the vector-sum interactions between the two primary peaks. However, Abreau et al. (1992), in formulating allowable interactions in their collision integral to develop a nonlinear refraction model, maintain that the third peak noted by Freilich et al. (1990) was actually a result of colinear resonant interactions due to the directional overlap between the two directional spectra. They used a digitized version of the data of Freilich et al. (1990) obtained from their paper to serve as input into their model; they demonstrate what they term reasonable agreement. Because of its allowance of interactions between different longshore wave number modes, the angular spectrum format is ideal for addressing this issue because directional interactions can be included or deleted at will; this is not possible with parabolic or time-domain models. Kaihatu and Kirby (1992) generated a simplified wave field consisting of only two monochromatic waves approaching at distinctly different angles with no directional overlap. They used the angular spectrum Boussinesq model of Kirby (1990) to propagate this bi-chromatic, bi-directional wave field and noted the interactions that occurred. They found a significant peak at the vector sum direction and the sum frequency, indicating a non-colinear vector sum interaction. With a more dispersive angular spectrum model, we may be able to simulate the field conditions of Freilich et al. (1990) with some confidence that the higher harmonics outside the shallow water range are modeled correctly. This could serve as motivation for further developing and refining the angular spectrum model of the fully nonlinear extended Boussinesq equations once the linear shoaling characteristics are improved.

REFERENCES

Abreau, M, Larraza, A., and Thornton, E.B., "Nonlinear transformation of directional wave spectra in shallow water," *Journal of Geophysical Research*, 97, pp. 15579-15589, 1992.

Agnon, Y., Sheremet, A., Gonsalves, J., and Stiassnie, M., "Nonlinear evolution of a unidirectional shoaling wave field," *Coastal Engineering*, 20, pp. 29-58, 1993.

Berkhoff, J.C.W., "Computation of combined refraction-diffraction," *Proceedings of the 13th International Conference on Coastal Engineering*, pp. 471-490, Vancouver, BC, 1972.

Bowen, G.D., "Shoaling and breaking random waves on a 1:35 laboratory beach," Master's thesis, University of Delaware, 1994.

Bryant, P.J., "Periodic waves in shallow water," *Journal of Fluid Mechanics*, vol. 59, pp. 625-644, 1973.

Bryant, P.J., "Stability of periodic waves in shallow water," *Journal of Fluid Mechanics*, vol. 66, pp. 81-96, 1974.

Chen, Y., and Liu, P.L.-F., "Modified Boussinesq equations and associated models for wave propagation," *Research Report CACR-93-06*, Center for Applied Coastal Research, University of Delaware, Newark, DE, 1993.

Dalrymple, R.A., and Kirby, J.T., "Models for very wide-angle water waves and wave diffraction," *Journal of Fluid Mechanics*, vol. 192, pp. 33-50, 1988.

Dalrymple, R.A., Suh, K.D., Kirby, J.T., and Chae, J.W., "Models for very wide-angle water waves and wave diffraction. Part 2. Irregular bathymetry," *Journal of Fluid Mechanics*, vol. 201, pp. 299-322, 1989.

Dean, R.G., and Sharma, J.N., "Simulation of wave systems due to nonlinear directional spectra," *Proceedings of International Symposium on Hydrodynamics in Ocean Engineering*, pp. 1211-1222, Trondheim, Norway, 1981.

Elgar, S., Guza, R.T., Freilich, M.H., and Briggs, M.J., "Laboratory simulations of directionally spread shoaling waves," *Jornal of Waterway, Port Coastal and Ocean Engineering*, ASCE, vol. 118, pp. 87-103, 1992.

Elgar, S., Guza, R.T., and Freilich, M.H., "Observations of nonlinear interactions in directionally spread shoaling surface gravity waves," *Journal of Geophysical Research*, 98, pp. 20299-20305, 1993.

Freilich, M.H., and Guza, R.T., "Nonlinear effects on shoaling surface gravity waves," *Philosophical Transactions of the Royal Society of London*, A311, pp. 1-41, 1984.

Freilich, M.H., Guza, R.T., and Elgar, S., "Observations of nonlinear effects in directional spectra of shoaling surface gravity waves," *Journal of Geophysical Research*, 95, pp. 9645-9656, 1990.

Goring, D.G., and Raichlen, F., "The generation of long waves in the laboratory," *Proceedings of the 17th International Conference on Coastal Engineering*, pp. 763-793, Sydney, Australia, 1980.

Hammack, J.L., Scheffner, N.W., and Segur, H., personal communication, 1990.

Kaihatu, J.M, and Kirby, J.T., "Spectral evolution of directional finite ampitude dispersive waves in shallow water," *Proceedings of the 23rd International Conference on Coastal Engineering*, pp. 364-377, Venice, Italy, 1992.

Keller, J.B., "Resonantly interacting water waves," *Journal of Fluid Mechanics*, vol. 191, pp. 529-534, 1988.

Kirby, J.T., "Modelling shoaling directional wave spectra in shallow water," *Proceedings of the 22nd International Conference on Coastal Engineering*, pp. 109-121, Delft, the Netherlands, 1990.

Kirby, J.T., "Intercomparison of truncated series solutions for shallow water waves," *Journal of Waterway, Port, Coastal and Ocean Engineering*, ASCE, vol. 117, no. 2, pp. 143-155, 1991.

Kirby, J.T., Kaihatu, J.M., and Mase, H., "Shoaling and breaking of random wave trains: spectral approaches," *Proceedings of the Ninth Engineering Mechanics Division Specialty Conference*, ASCE, pp. 71-74, College Station, TX, 1992a.

Kirby, J.T., Lee, C., and Rasmussen, C., "Time-dependent solutions of the mild-slope wave equation," *Proceedings of the Twenty-Third International Conference on Coastal Engineering*, pp. 391-404, Venice, Italy, 1992b.

Kirby, J.T., and Wei, G., "Derivation and properties of a fully nonlinear model for weakly dispersive waves," *International Symposium on Waves - Physical and Numerical Modelling*, Vancouver, BC (to appear), 1994.

Liu, P.L.-F., Yoon, S.B., and Kirby, J.T., "Nonlinear refraction-diffraction of waves in shallow water," *Journal of Fluid Mechanics*, vol. 153, pp. 185-201, 1985.

Lozano C.J., and Liu, P.L.-F., "Refraction-diffraction model for linear surface water waves," *Journal of Fluid Mechanics*, vol 101, pp. 705-720, 1980.

Madsen, P.A., Murray, R., and Sørensen, O.R., "A new form of the Boussinesq equations with improved linear dispersion characteristics," *Coastal Engineering*, 15, pp. 371-388, 1991.

Madsen, P.A., and Sørensen, O.R., "A new form of the Boussinesq equations with improved linear dispersion characteristics. Part 2. A slowly-varying bathymetry," *Coastal Engineering*, 18, pp. 183-204, 1992.

Madsen, P.A., and Sørensen, O.R., "Bound waves and triad interactions in shallow water," *Ocean Engineering*, 20, pp. 359-388, 1993.

Mase, H, and Kirby, J.T., "Hybrid frequency-domain KdV equation for random wave transformation," *Proceedings of the 23rd International Conference on Coastal Engineering*, pp. 474-487, Venice, Italy, 1992.

McCowan, A.D., and Blackman, D.R., "The extension of Boussinesq-type equations to modelling short waves in deep water," *Proceedings of the Ninth Australasian Conference on Coastal and Ocean Engineering*, pp. 412-416, Adelaide, Australia, 1989.

Nwogu, O., "Alternative form of Boussinesq equations for nearshore wave propagation," *Journal of Waterway, Port, Coastal and Ocean Engineering*, ASCE, vol. 119, no. 6, pp. 618-638, 1993.

Nwogu, O., "Nonlinear transformation of multi-directional waves in water of variable depth," submitted to *Journal of Fluid Mechanics*, 1994.

Peregrine, D.H., "Long waves on a beach," *Journal of Fluid Mechanics*, vol. 27, part 4, pp. 815-827, 1967.

Phillips, O.M., *The Dynamics of the Upper Ocean*, 2nd edition, Cambridge University Press, New York, 1977.

Press, W.H., Flannery, B.P., Teukolsky, S.A., and Veeterling, W.T., *Numerical Recipies: The Art of Scientific Computing*, Cambridge University Press, New York, 1986.

Radder, A.C., "On the parabolic equation method for water-wave propagation," *Journal of Fluid Mechanics*, vol. 95, part 1, pp. 159-176, 1979.

Rygg, O.B., "Nonlinear refraction-diffraction of surface waves in intermediate and shallow water," *Coastal Engineering*, 12, pp. 191-211, 1988.

Segur, H., and Finkel, A. "An analytical model of periodic waves in shallow water," *Studies of Applied Mathematics*, vol. 73, pp. 183-220, 1985.

Smith, R., and Sprinks, T., "Scattering of surface waves by a conical island," *Journal of Fluid Mechanics*, vol. 72, part 2, pp. 373-384, 1975.

Svendsen, I.A., "A direct derivation of the KdV equation for waves on a beach, and discussion of its implications," *Progress Report*, 39, 9-14, ISVA, Technical University of Denmark, Lyngby, Denmark, 1976.

Thornton, E.B., and Guza, R.T., "Transformation of wave height distribution," *Journal of Geophysical Research*, 88, C10, pp. 5925-5938, 1983.

Wei, G., and Kirby, J.T., "A time-dependent numerical code for extended Boussinesq equations," *Research Report CACR-94-02*, Center for Applied Coastal Research, University of Delaware, Newark, DE, 1994.

Whalin, R.W., "The limit of application of linear wave refraction theory in a convergence zone," *Research Report H-71-3*, U.S. Army Engineer Waterways Experiment Station, Vicksburg, MS, 1971.

Witting, J.M., "A unified model for the evolution of nonlinear water waves," *Journal of Computational Physics*, vol. 56, pp. 203-236, 1984.

Yue, D.K.P., and Mei, C.C., "Forward diffraction of Stokes waves by a thin wedge," *Journal of Fluid Mechanics*, vol. 99, pp. 33-52, 1980.